TECHNISCHE UNIVERSITÄT MÜNCHEN

TUM School of Life Sciences

In-depth characterization of mouse models for monogenic diabetes and gene therapy of Hnf4a-KI mice

Anna-Lena Amend

Vollständiger Abdruck der von der TUM School of Life Sciences der Technischen Universität München zur Erlangung des Grades einer

Doktorin der Naturwissenschaften

genehmigten Dissertation.

Vorsitzender: apl. Prof. Dr. Ramon Torres Ruiz

Prüfer der Dissertation: 1. Prof. Dr. Dr. h. c. mult. Martin Hrabě de Angelis

2. Prof. Angelika Schnieke, Ph.D.

Die Dissertation wurde am 04.04.2022 bei der Technischen Universität München eingereicht und durch die TUM School of Life Sciences am 05.07.2022 angenommen.

Table of Contents

List of Figures

List of Tables

List of Appendix A Figures

List of Appendix B Figures

List of Abbreviations

Table 1 List of abbreviations

Abbreviation	Full Name
°C	Degree Celsius
α	alpha
β	beta
δ	delta
ε	epsilon
µ	micro
AAV	Adeno-associated virus
ANOVA	Analysis of variance
ATF6	Activating transcription factor 6, encoded by *Atf6*
AUC	Area under the curve
BG	Blood glucose
BiP	Heat shock protein 5, encoded by *Hspa5*
BMI	Body mass index
bp	Base pair
BSA	Bovine serum albumin
BW	Body weight
CALR	Calreticulin
cDNA	Complementary DNA
CO_2	Carbon dioxide
Cp	Crossing point
%CV	Coefficient of variation
d	deionized
Da	Dalton
DNA	Deoxyribonucleic acid
DBPS	Dulbecco’s Phosphate Buffered Saline
dNTPs	Deoxyribonucleic triphosphates
DTT	Dithiothreitol
EDTA	Ethylenediaminetetraacetic acid
ELISA	Enzyme-linked immunosorbent assay
ER	Endoplasmic reticulum

ERAD	ER-associated degradation
ERO	Endoplasmic reticulum oxidoreductase
EtOH	Ethanol
FBS	Fetal bovine serum
FC	Fold change
g	Gram
G	Gauge
GCG	Glucagon, encoded by *Gcg*
GCK	Glucokinase, encoded by *Gck*
GLUT2	Glucose transporter 2, encoded by *Slc2a2* (solute carrier family 2, member 2)
GMC	German Mouse Clinic
GSIS	Glucose-stimulated insulin secretion
GTT	Glucose tolerance test
h	hour
H_2O	Water
HBSS	Hanks' Balanced Salt Solution
HCl	Hydrochloric acid
HDR	Homology directed repair
HEPES	4-(2-hydroxyethyl)-1-piperazineethanesulfonic acid
het	heterozygous
HFD	High fat diet
HKG	Housekeeping gene
HMW	High molecular weight
HNF1A	Hepatocyte nuclear factor 1 A, encoded by *Hnf1a*
HNF4A	Hepatocyte nuclear factor 4 A, encoded by *Hnf4a*
hom	homozygous
IF	Immunofluorescence
INS	Insulin
ip	Intraperitoneal
IRE1A	Endoplasmic reticulum to nucleus signaling 1, encoded by *Ire1a*
ITT	Insulin tolerance test
k	kilo
KI	Knock-in

KO	Knock-out
KRB	Krebs Ringer buffer
L	Liter
LC3	Microtubule-associated protein 1 light chain 3 alpha, encoded by *Map1lc3*
m	milli
M	Molar
MAFA	v-maf musculoaponeurotic fibrosarcoma oncogene family A, encoded by *Mafa*
MAFB	v-maf musculoaponeurotic fibrosarcoma oncogene family B, encoded by *Mafb*
MIDY	Mutant *INS*-gene induced diabetes of youth
MODY	Maturity onset diabetes of the young
n	nano
n	In statistics: sample size (number of samples)
NaCl	Sodium chloride
NaOH	Sodium hydroxide
NKX6-1	NK6 Homeobox 1, encoded by *Nkx6.1*
NMR	Nuclear magnetic resonance
P-	Phospho-
P62	Sequestosome 1, encoded by *Sqstm1*
PBS	Phosphate-buffered saline
PCR	Polymerase chain reaction
PDI	Protein disulfide isomerase
PDX1	Pancreatic duodenal homeobox 1, encoded by *Pdx1*
PERK	Eukaryotic translation initiation factor 2 alpha kinase 3, encoded by *Eif2ak3*
PFA	Paraformaldehyde
pH	Base 10 logarithm of the molar concentration of hydrogen ions in units of moles per liter
PP	Pancreatic polypeptide
PROINS	proinsulin
qRT-PCR	Quantitative real-time polymerase chain reaction
R^2	Coefficient of Determination
rAAV	Recombinant AAV

RFU	Relative fluorescence units
RIDD	Regulated *Ire1*-dependent decay
RNA	Ribonucleic acid
ROS	Reactive oxygen species
rpm	Revolutions per minute
RPMI	Roswell Park Memorial Institute medium
RRP	Readily Releasable Pool
RT	Room temperature
s	Second
SD	Standard deviation
SDS	Sodium dodecyl sulfate
SEM	Standard error of the mean
Slc2a2	Solute Carrier Family 2 Member 2 (gene encoding GLUT2)
STZ	Streptozotocin
T1DM	Type 1 diabetes mellitus
T2DM	Type 2 diabetes mellitus
TBS	Tris-buffered saline
TEM	Transmission electron microscopy
TF	Transcription factor
TG	Triglyceride
U	Unit
UCN3	Urocortin 3, encoded by *Ucn3*
UPR	Unfolded protein response
UTR	Untranslated region
V	Volt
VCP	Valosin-containing protein
vg	Viral genomes
WT	Wild type
×**g**	Times G-force

II Summary

About 1.5-2% of all diabetes patients worldwide suffer from a rare form of diabetes, so-called monogenic diabetes, in which a mutation in a single gene leads to diabetes. Common to most of these patients is a lifelong dependency on medication, since common therapies do not address the underlying genetic defects. An emerging form of treatment for genetic diseases is gene therapy, which, once approved, has the potential for becoming a one-time treatment that could bring lifelong benefits to patients.

This project focused on the detailed characterization of nine mouse models for monogenic diabetes and the feasibility of AAV-mediated gene therapy for their treatment. The results of this study provide valuable insights into the pathophysiology of monogenic diabetes caused by *Ins2*, *Pdia6* and *Hnf4a* mutations and confirmed the possibility of gene transfer directly to the pancreas.

Each of the models was subjected to an individualized series of *in vitro* and *in vivo* experiments to follow the progression of diabetes and to elucidate the signaling pathways involved in disease mechanisms.

Mouse models with *Ins2* mutations presented with severe, early-onset diabetes accompanied by hypoinsulinemia. The overload of misfolded proteins in the ER caused mild ER- and oxidative stress. Signs for β-cell death could not be observed, instead, evidence of β-cell dedifferentiation was found. In addition, autophagy processes seemed to be activated which may play a more important role in the disease mechanism than previously thought.

Pdia6-mutant mice showed reduced Mendelian ratio, lower body weight and severe hypoinsulinemia and hypoproinsulinemia. The underlying reasons for the metabolic defect indicated β-cell dedifferentiation and ER-stress.

None of the Hnf4a mouse models showed a diabetic phenotype and only in one of them a downregulation of *Hnf4a* in β-cells could be observed. *Hnf4a*-mutations are loss-of-function mutations and could therefore be treated by gene therapy. The technique of intraductal rAAV-injection was implemented and the feasibility of therapeutic gene transfer into the pancreas was demonstrated without observing toxic effects.

Pdia6- and *Ins2*-mutant mouse models both suffer from gain-of-toxic function mutations. Whether gene therapy that provides a healthy version of the gene is appropriate to treat their diseases is up for debate.

III Zusammenfassung

Etwa 1,5-2% aller Diabetespatienten weltweit leiden an einer seltenen Form von Diabetes, dem so genannten monogenetischen Diabetes, bei dem eine Mutation in einem einzigen Gen zu Diabetes führt. Die meisten dieser Patienten haben gemeinsam, dass sie lebenslang auf Medikamente angewiesen sind, da die gängigen Therapien die zugrundeliegenden Gendefekte nicht beheben. Eine neue Form der Behandlung genetisch bedingter Krankheiten ist die Gentherapie, die, sobald sie zugelassen ist, das Potenzial hat, eine einmalige Behandlung zu werden, die den Patienten lebenslange Vorteile bringen könnte.

Dieses Projekt konzentrierte sich auf die detaillierte Charakterisierung von neun Mausmodellen für monogenetischen Diabetes und die Durchführbarkeit der AAV-vermittelten Gentherapie für deren Behandlung. Die Ergebnisse dieser Studie liefern wertvolle Einblicke in die Pathophysiologie des monogenetischen Diabetes, der durch *Ins2*-, *Pdia6*- und *Hnf4a*-Mutationen verursacht wird, und bestätigten die Möglichkeit eines Gentransfers direkt in die Bauchspeicheldrüse.

Jedes der Modelle wurde einer individuellen Reihe von *in vitro*- und *in vivo*-Experimenten unterzogen, um das Fortschreiten des Diabetes zu verfolgen und die an den Krankheitsmechanismen beteiligten Signalwege aufzuklären.

Mausmodelle mit *Ins2*-Mutationen wiesen einen schweren, früh einsetzenden Diabetes auf, der mit einer Hypoinsulinämie einherging. Die Überladung mit fehlgefalteten Proteinen im ER verursachte leichten ER- und oxidativen Stress. Anzeichen für ein Absterben der β-Zellen konnten nicht beobachtet werden, stattdessen fanden sich Hinweise auf eine Dedifferenzierung der β-Zellen. Darüber hinaus schienen Autophagie-Prozesse aktiviert zu sein, die möglicherweise eine wichtigere Rolle im Krankheitsmechanismus spielen als bisher angenommen.

Das Mausmodel mit einer *Pdia6*-Mutation zeigte eine reduzierte Mendelsche Verteilung, ein geringeres Körpergewicht sowie eine schwere Hypoinsulinämie und Hypoproinsulinämie. Die Ursachen für den Stoffwechseldefekt deuten auf eine Dedifferenzierung der β-Zellen und ER-Stress hin.

Keines der *Hnf4a*-Mausmodelle zeigte einen diabetischen Phänotyp und nur in einem von ihnen konnte eine Reduktion von *Hnf4a* in β-Zellen beobachtet werden. *Hnf4a*-Mutationen sind Mutationen, die zum Verlust der Funktion führen und könnten daher durch Gentherapie behandelt werden. Die Technik der intraduktalen rAAV-Injektion wurde angewandt und die Durchführbarkeit des therapeutischen Gentransfers in die Bauchspeicheldrüse nachgewiesen, ohne dass dabei toxische Effekte beobachtet wurden.

Sowohl das *Pdia6*- als auch die *Ins2*-Mausmodelle leiden unter Mutationen, die zu einer toxischen Funktion führen. Ob eine Gentherapie, die eine gesunde Version des Gens bereitstellt, zur Behandlung dieser Krankheiten geeignet ist, steht zur Debatte.

1. Introduction

1.1 The pancreas and the islets of Langerhans

Almost everyone is related to someone or knows someone who is affected by diabetes. It is a growing epidemic on the rise and day by day, more and more people are affected by chronically elevated blood sugar. The organ in the body that is responsible to regulate the blood sugar is the pancreas. The pancreas is both an endocrine as well as an exocrine organ and arises during embryonic development from a ventral and dorsal bud starting at embryonic day 9.5 (E9.5) in mice. Its exocrine and endocrine compartments differentiate in a complex, not yet fully understood pattern from pancreatic multipotent progenitor cells (MPCs). Both compartments differ functionally as well as morphologically. Pancreas organogenesis has been reviewed and described extensively in the past 30 years [1-3]. Cell fates are determined by an extensive and complex interplay of intrinsic and exogenous signals and transcription factors, all working together to specify lineage, differentiation and growth [4].

The exocrine compartment is made up from acinar cells, which secrete mostly enzymes that help with digestion. The endocrine compartment is aggregated in cell clusters, which are commonly called the islets of Langerhans (short: islets) as they were first described by Paul Langerhans in 1869 [5]. Experiments by Mering and Minkowski in 1889 first suggested that removal of the pancreas caused diabetes in dogs [6]. In 1921, now about 100 years ago, Banting and Best discovered the hormone responsible for this effect and named it insulin, thereby revolutionizing diabetes care [7].

There are five types of endocrine, hormone secreting cells within the islets: glucagon-secreting α-cells, insulin-secreting β-cells, somatostatin-secreting δ-cells, ghrelin-secreting ε-cells and pancreatic polypeptide-secreting PP-cells [1].

Islet architecture varies greatly within species. In adult rodents, β-cells make up around 60-80% of all islet cells. Approximately 15-20% of the cells are α-cells and less than 10% are δ-cells [8, 9]. The β-cells are centrally localized forming the core, while the other cells, mainly α- and δ-cells, are arranged around the periphery. Only few PP- and ε-cells are present, which are also localized in the mantle region [9, 10]. In humans, the different

cells types are more intermingled and not as strictly organized [11]. Here, β-cells generally make up around 60% of all islet cells. About 30% are α-cells, the remaining 10% are δ-, PP- and ε-cells, all randomly distributed over the islet [12]. An overview of islet architectures is provided in Figure 1.

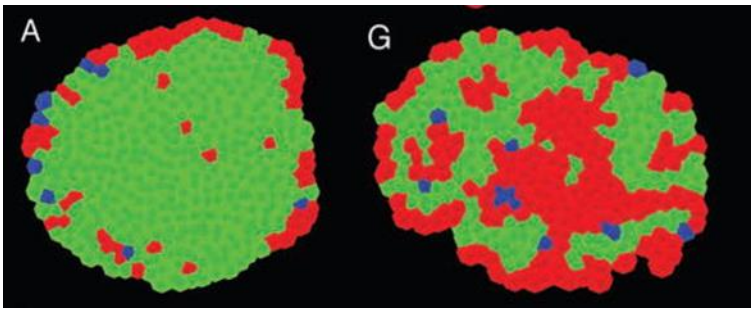

Figure 1 Islet architecture in rodents and humans

Comparison of mouse (A) and human islets (G) under healthy, normal conditions. Red: α-cells, Green: β-cells, Blue: δ-cells. This Figure is adapted from Steiner et al., 2010.

These cells together form spherical structures coming up to around 50-500 µm in diameter, each containing 50-3000 cells [13]. Concerning size, there is very little difference between species, by that suggesting an evolutionarily optimized size [14] for generating action potential to aid in its main function, insulin secretion.

1.2 Glucose-stimulated insulin secretion (GSIS) from β-cells

One very important hormone in the context of diabetes is produced by the pancreas: insulin, which acutely reduces blood sugar levels. Pancreatic β-cells are the body's glucose sensors and acutely regulate insulin secretion to maintain glucose homeostasis. The β-cells are responsible for the synthesis, sorting and secretion of insulin [12, 13]. If this process is impaired, it leads to chronic elevation of blood glucose and hyperglycemia, which eventually leads to diabetes [13, 15]. Tight regulation of the system is very important as severe hypoglycemia caused by hypersecretion of insulin is fatal [13].

An overview of the signaling mechanisms in β-cells that ultimately lead to insulin release is given in Figure 2. This is mostly glucose-stimulated insulin secretion (GSIS). GSIS is an important determining factor for healthy β-cell function [13].

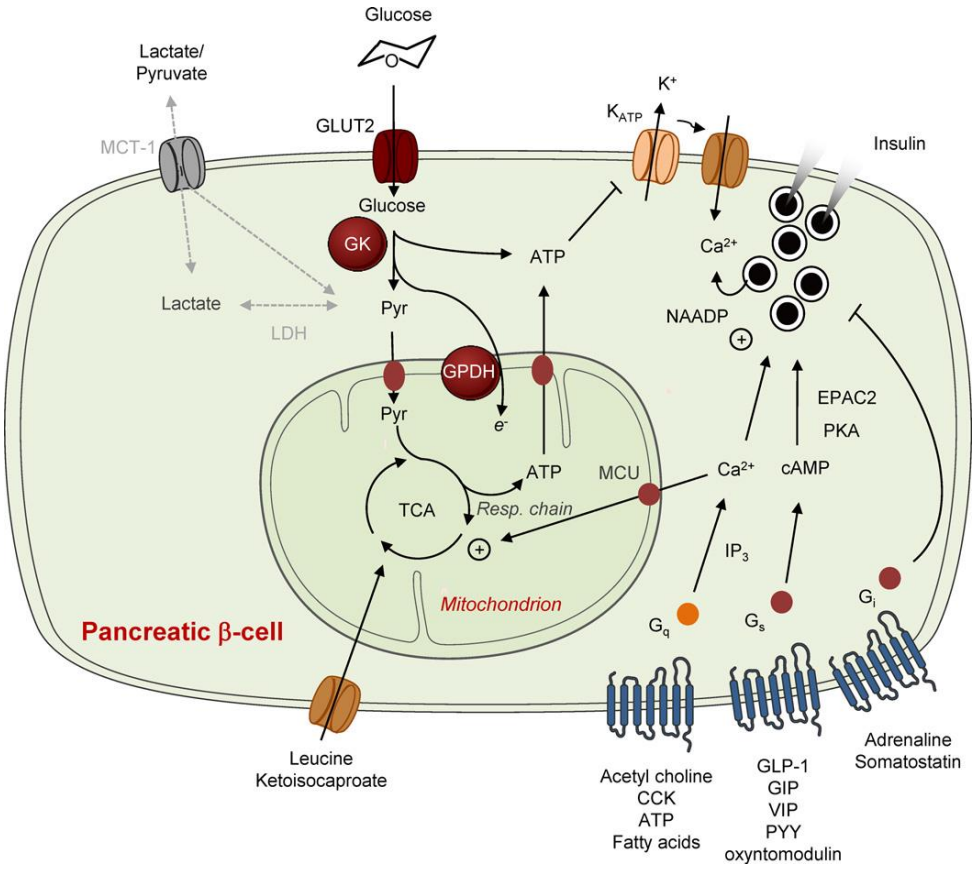

Figure 2 Overview of glucose sensing and insulin secretion in β-cells

A detailed description about the processes is given in the text of this chapter (1.2). This Figure is adapted from Rutter et al., 2015.

When glucose is present, glucose transporters carry it across the plasma membrane into the β-cell. The main transporters are GLUT2, encoded by *Slc2a2*, in rodents and GLUT1, encoded by *SLC2A1*, in humans. The intracellular sensor for glucose is the enzyme glucokinase (GCK) that initiates glycolysis as the metabolic response [16]. The final product of glycolysis, pyruvate, reaches the mitochondria via specialized carriers [17] and enters the tricarboxylic acid (TCA) cycle. After oxidative phosphorylation in the mitochondria, the ATP that was generated throughout the processes is exported, which effectively increases the ATP/ADP ratio in the cytoplasm, which in turn closes ATP-sensitive potassium channels (K_{ATP}) [18, 19]. The resulting depolarization of the cell membrane opens voltage-gated calcium channels, which leads to an increased Ca^{2+} concentration in the cytoplasm. Other mechanisms can help increase the intracellular Ca^{2+} concentration. Finally, the increased Ca^{2+} leads to the fusion of insulin-containing vesicles, which are stored in readily releasable pools (RRP), with the plasma membrane.

Insulin is released to the blood stream and transported to insulin-sensing tissues, the most important being skeletal muscle, and white adipose tissue. After binding to its receptor, insulin triggers diverse, tissue-specific responses that finally result in the lowering of blood glucose [20].

Other factors also influence insulin release (see also Figure 2 and [13]). Examples include glucagon-like peptide-1 (GLP-1) and glucose-dependent insulinotropic polypeptide (GIP). These peptides produced by the gut are also known as incretin hormones. They are responsible for the incretin effect, according to which the intravenous injection of glucose leads to a significantly lower release of insulin than oral glucose administration [21].

1.3 What makes a β-cell a β-cell: Is it all about identity?

What exactly defines the molecular identity of β-cells besides function? This question has received a lot of attention in recent years and has generated considerable interest [12, 22, 23]. In order to find and implement novel therapies for diabetes, it is of fundamental importance to understand cellular function and to know as much as possible about what makes a β-cell a functional β-cell. A complex network of genes and factors have been described that are associated with functionally mature β-cells and regulate insulin transcription. Throughout their life cycle from the onset of embryonic development through differentiation to postnatal maturation, β-cells undergo a multitude of molecular and metabolic changes that will ultimately lead to functionally mature β-cells that are able to respond to glucose stimuli.

During embryonic development of rodents, the differentiation and fate of β-cells depends on the dynamic expression of a multitude of genes and transcription factors (TFs) such as PDX1 and NKX6-1, which remain to be expressed in adult β-cells [23-25]. After birth, β-cells, which are still considered immature, undergo a bi-phasic maturation process. The first wave of maturation takes place within the first two weeks after birth, when β-cells still proliferate and acquire the expression of TFs that are necessary for future adult β-cell identity e.g. PDX1 [26]. Increasingly, β-cells lose the ability to proliferate and acquire the ability to secrete insulin in response to glucose (GSIS). A second maturation wave takes place between the third week of life and the time of weaning (P21), when various metabolic pathways adapt to the changes in diet as depicted in Figure 3 [23]. In this late

postnatal maturation phase, Maf-transcription factors are important to finally establish β-cell identity [27]. For β-cells, the switch from *Mafb* expression, which is active in embryonic β-cells, to *Mafa* expression is considered crucial. Interestingly, in humans, *MAFB* remains to be expressed at high levels in adult β-cells, whilst in rodents *Mafa* is mostly restricted to mature α-cells. Such differences between rodents and humans must always be considered when translating rodent-based research to humans.

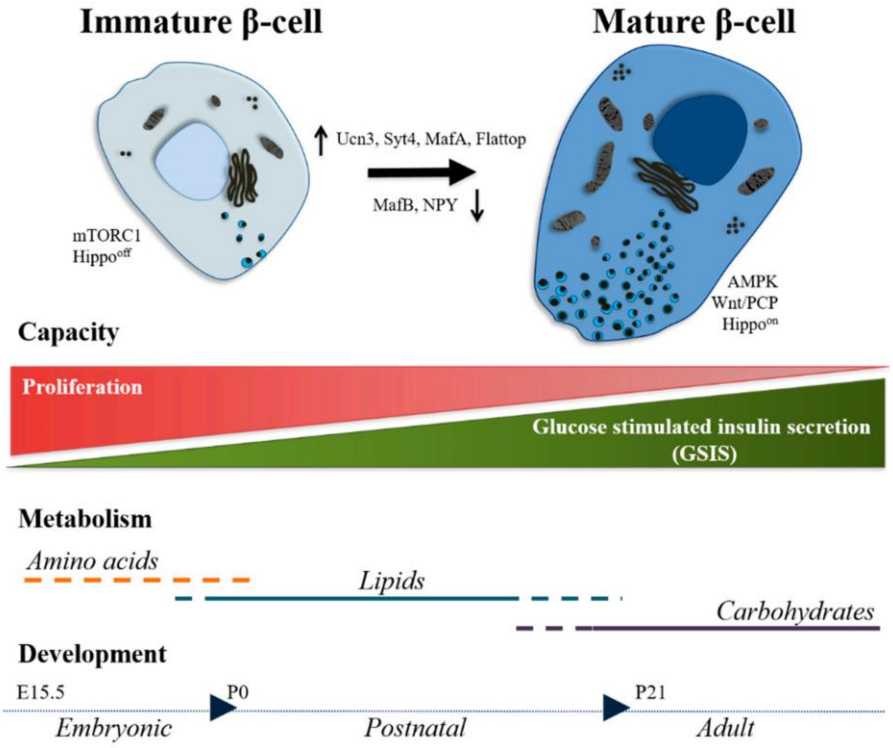

Figure 3 Immature and mature β-cells

During the post-natal maturation process, β-cells undergo a variety of molecular changes. They increasingly lose the ability to proliferate and acquire the ability to perform GSIS. This Figure is adapted from Salinno et al., 2019.

On a side note, it has been shown in both humans and rodents that not all β-cells acquire full maturity in life. Some cells retain immature characteristics, which describes a pronounced β-cell heterogeneity [23, 28].

Taken together, several transcription factors provide functional and morphological identity to β-cells. Some of them, for example PDX1, are also required to regulate insulin expression [29]. Typical signature genes for mature β-cells include *Ucn3*, *Slc2a2*, *Pdx1*, *Mafa*, *Ins2* and *Nkx6-1* [23, 26]. A low expression of these genes and increased expression of progenitor markers such *Ngn3* are associated with dysfunctional β-cells,

which can lead to hyperglycemia and ultimately diabetes. The dedifferentiation and transdifferentiation of β-cells during sustained hyperglycemia and diabetes are described in detail in the next section in 1.4.

1.4 Causes and effects of β-cell dysfunction or loss of β-cells in diabetes

Loss of β-cell function or loss of β-cells has dramatic effects on glucose homeostasis and is the underlying reason for all types of diabetes (see chapter 1.5 for detailed information on diabetes). Several factors can contribute to β-cell dysfunction, for example glucotoxicity due to persistent hyperglycemia, changes in the differentiation state of β-cells, endoplasmic reticulum (ER)- and oxidative stress, or mutations in genes relevant to β-cell function. Mutations in some of these genes are known causes for monogenic diabetes [30-32]. In the following chapter, these factors are described in more detail.

1.4.1 Physiological ER-stress and insulin (mis)folding

Pancreatic β-cells are strongly adapted to physiological ER-stress due to their immense protein turnover, especially that of insulin. The need to continuously meet metabolic demands naturally also leads to misfolding, which is why β-cells are heavily dependent on a functioning cellular machinery to take care and dispose of misfolded proteins. Disturbances of the system such as a massively increased demand during insulin resistance and obesity, inflammatory processes in type 1 diabetes mellitus (T1DM) or mutations in relevant genes put additional burden on β-cells and can thus progressively increase ER-stress and eventually lead to β-cell death [33-35].

The folding and misfolding of proinsulin and its effects have been studied and reviewed in detail in recent years [36, 37]. The processes are shown and described in Figure 4 below. In brief, after transcription of the preproinsulin gene in the nucleus and translocation of the protein into the ER, a peptidase cleaves the signal peptide. The proinsulin molecules then rapidly undergo oxidative folding. Members of the ER-resident family of protein disulfide isomerases (PDIs) with their oxidoreductase and isomerase activities facilitate the formation of the three disulfide bridges and thus play a key role in insulin biosynthesis. ER-oxidoreductases (EROs) shuttle the reducing equivalents and regenerate oxidized PDIs [36, 38].

The mature insulin molecule consists of one A- and one B-chain, connected by two interchain disulfide bonds (A7-B7; A20-B19) and one intrachain disulfide-bond in the A-chain (A6-A11). Disulfide pairing is an intricate process that has been researched and reviewed in detail by M. Liu and colleagues over many years [39-44]. Folded proinsulin is stored in vesicles. Upon stimulation, peptidases cleave the proinsulin and mature insulin is released into the blood stream with equimolar amounts of C-peptide.

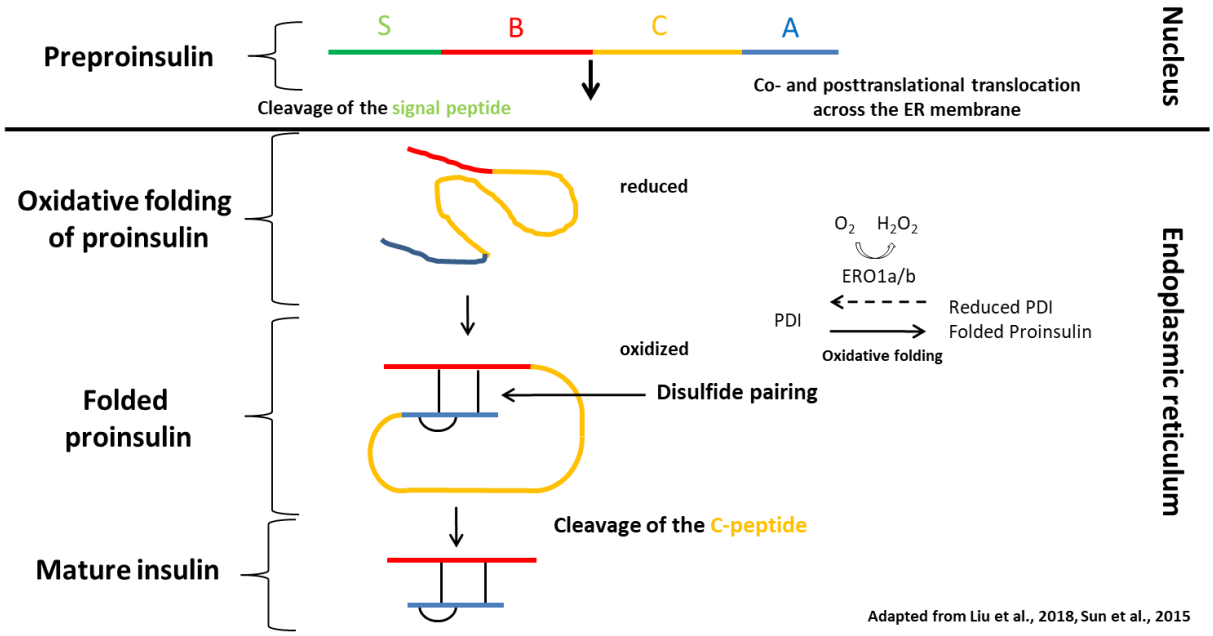

Figure 4 Insulin folding and processing

The preproinsulin molecule consists of 4 segments: Signal peptide (green), B-chain (red), C-peptide (yellow) and A-chain (blue). After transcription, the molecule enters the ER by co- and posttranslational translocation across the ER membrane and the signal peptide gets cleaved. Now the molecule is called proinsulin. Within the ER, proinsulin first remains in an unfolded, reduced state. The subsequent oxidative folding and disulfide pairing is thought to be facilitated by PDIs, which are regenerated by EROs. During oxidative folding, the three disulfide bonds of the insulin molecule are formed. Upon stimulation, the C-peptide is excised from the molecule and mature insulin is released to the blood stream. This Figure was created based on Liu et al., 2018 and Sun et al., 2015.

Mutations in the coding sequence of proinsulin or in genes that alter the folding environment in the ER often lead to deficient insulin production and resulting diabetes. This has been analyzed in a variety of mouse models and humans with a variety of different mutations, some of which are described in other sections (1.6.1).

1.4.2 **ER-stress and UPR**

When there is a misbalance between metabolic demand and the capacity for protein folding, ER-homeostasis is disrupted, resulting in ER-stress. When misfolded proteins accumulate, as it is regularly the case in β-cells due to the high transcription load to meet the high metabolic demand of insulin, the unfolded protein response (UPR) gets activated in order to restore ER-homeostasis [33]. Another system, ERAD, removes unfolded proteins from the ER to the cytosol for proteasomal degradation. ERAD and UPR are in a constant crosstalk to maintain ER-homeostasis [45].

There are three classic ER-stress sensors located in the ER membrane: PERK, IRE1A and ATF6. Under normal conditions, binding immunoglobulin protein (BiP, encoded by *Hspa5*) associates with the 3 sensors. When misfolded proteins or other stressors are detected, BiP dissociates from the sensors and gets recruited by the misfolded proteins, thereby activating the ER-stress response, UPR. Activation of the signaling cascades leads to a variety of effects that are described in detail below. An overview of the three UPR arms is provided in Figure 5 [46].

PERK, encoded by *Eif2ak3*, has long been described as an important regulator of proinsulin trafficking and quality control in the secretory pathway [47]. Upon activation, the PERK-eIF2α-pathway reduces transcription and by that, decreases protein load and accumulation in the ER, especially that of insulin. Phosphorylation of eIF2α by activated PERK, the second step in the signaling cascade, has even been described as the Achilles heel of pancreatic β-cells by Cnop et al. [33]. In *Eif2ak3*-null cells and mice, a severely distended ER was observed, suggesting that PERK plays a role in maintaining ER-homeostasis and is an important indicator of ER-stress [47, 48]. A mouse model with an eIF2α-S51A mutation, recapitulated the effect of *Eif2ak3*-null on the ER, including an increased and unregulated translation of proinsulin [49]. Finally, the expression of CHOP (encoded by *Ddit3*), which is activated via the same pathway, increases reactive oxygen species (ROS), which increases oxidative stress and ultimately leads to β-cell death [50].

In humans, mutations in in the coding gene *EIF2AK3* result in a severe form of permanent neonatal diabetes mellitus (PNDM), also called Wolcott-Rallison syndrome [51].

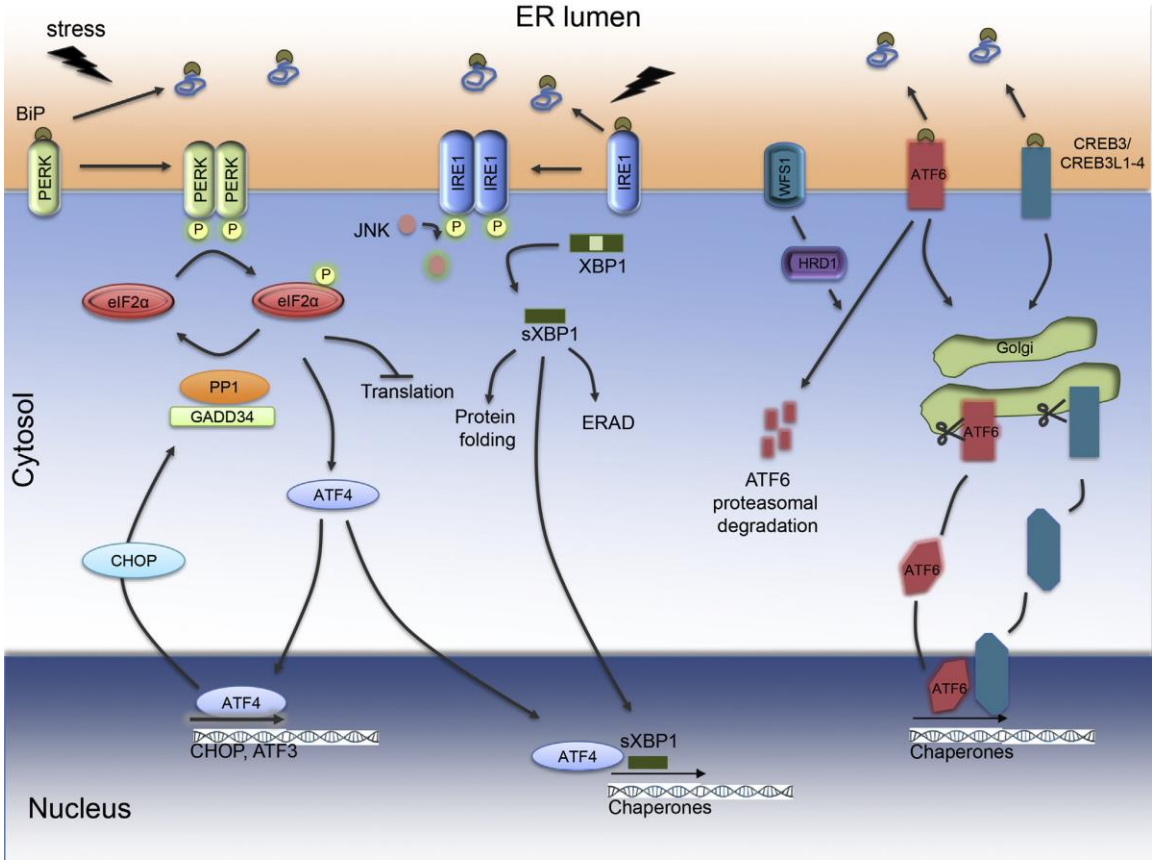

Figure 5 ER-stress transducers and activated pathways

During ER-stress, the chaperone BiP dissociates from the three ER-stress transducers PERK, IRE1 and ATF6 and binds to misfolded proteins. Activated PERK phosphorylates eIF2α, generally reduces transcription and induces chaperone and CHOP expression. Activated IRE1 splices XBP1 that upregulates chaperone expression to improve protein folding and ERAD. Activated ATF6 initiates chaperone expression via the Golgi apparatus. This Figure is adapted from Cnop et al., 2017.

The IRE1A-XBP1 is the second and most conserved branch of UPR. Upon activation, IRE1A splices *Xbp1*-mRNA which then upregulates chaperone expression and ERAD. In addition, it activates the regulated *Ire1*-dependant decay (RIDD) of ER-associated mRNAs [52], including itself, thereby effectively reducing the transcription load [53]. During mild stress, IRE1A promotes cell survival, but under high and unresolvable ER stress, it can also stimulate cell death [33, 54]. Deletion of IRE1A from β-cells in adult mice resulted in overt diabetes and the deregulation of several hundred genes important for GSIS [55]. In addition, the expression of genes associated with ROS was increased, which increased oxidative stress and eventually caused β-cell failure [55]. Interestingly,

deletion of IRE1α in NOD mice, a mouse model for T1DM, induced transient dedifferentiation of β-cells resulting in reduced β-cell apoptosis [56].

The third sensor is ATF6, a transcription factor trafficking to the Golgi upon activation where it is cleaved. Its activated fragment is a potent transcriptional activator for genes with complementary functions such as those activated by sXBP1. Upon metabolic stress by a high fat diet (HFD), ATF6α-null mice became glucose intolerant and showed blunted insulin secretion, suggesting a role for ATF6α in β-cell failure and protection from ER-stress [57].

In summary, the three pathways are intertwined and their combined activation eventually eliminates misfolded proteins to alleviate ER-stress and restore homeostasis in the ER. However, if ER-stress persists, cell death can be initiated via the same pathways, effectively reducing β-cell mass [33, 36, 46]. From the above-mentioned studies (and many others), it appears that ER-stress and increased UPR significantly contribute to diabetes pathogenesis.

1.4.3 **Oxidative stress: PDIs and EROs in β-cells**

Oxidative stress is another potent disruptor of ER-homeostasis [58]. The oxidative folding of insulin (shown in Figure 4) is facilitated by PDIs and EROs, which provide β-cells with important functions and regulate their oxidative milieu. Several studies have shown that deleting some PDIs or EROs dramatically decreases insulin secretion and disrupts glucose homeostasis [59-62]. Furthermore, they have been found to be deregulated during diabetes and potentially contribute to the pathogenesis of the disease by causing misfolding and leading to ER-stress.

PDIA1 is the most abundant of to date 17 known ER-oxidoreductases. The β-cell specific deletion of *Pdia1* resulted in increased glucose intolerance during metabolic stress and diminished insulin granule content. High molecular weight complexes, an indication for misfolded molecules, were detected in the ER [61]. PDIA6, albeit being lesser-known, was found to be important for the regulation of insulin secretion and its gene *Pdia6* was upregulated in a streptozotocin (STZ)-treated diabetes model (STZ is toxic specifically to β-cells and causes T1DM) [60, 63, 64].

EROs are responsible for regenerating oxidized PDIs. In mammals, the known genes are *Ero1a* and *Ero1b*. *Ero1b* is specifically expressed in the pancreas, whilst *Ero1a* is also found in other tissues [62]. *Ero1b* has been shown to be important for glucose homeostasis and to be required for oxidative folding of insulin in β-cells [59]. In *Ero1b*-deficient mice, glucose tolerance and GSIS were impaired [62]. In addition, *ERO1B* was found to be dysregulated in type 2 diabetes mellitus (T2DM) patients [59, 62].

Taken together, disruptions of the PDI/ERO oxidative folding system increase oxidative stress, disturb insulin production and lead to increased misfolding events, consequently also increasing ER-stress and the UPR.

1.4.4 **Autophagy**

In addition to ER-associated degradation, there is also lysosomal degradation that aids in the removal of misfolded proteins. One of the pathways to reach the lysosomes is autophagy, which has attracted attention in recent years as it has been shown to protect against ER-stress and to help regulate insulin homeostasis. Indeed, upon genetic disruption or inhibition of autophagy, proinsulin content in β-cells was increased [65, 66]. *In vivo*, autophagy-deficient mice showed β-cell degeneration, insulin deficiency and glucose intolerance [67]. In human islets exposed to ER-stress, induced autophagy prevented β-cell apoptosis. In addition, in T2DM donor islets, stimulation of autophagy by rapamycin has improved β-cell function and survival [65].

One important autophagy receptor protein is SQSTM1 (also called P62) which selects and binds to substrate molecules. P62 then delivers the molecules to the autophagosome by interacting with MAP1LC3, subsequently called LC3, which is anchored in the autophagosome membrane. The whole structure, including the two molecules themselves, will then be degraded by autophagy [68, 69].

Taken together, these findings show that autophagy and its modulation should be considered when analyzing β-cell dysfunction and ER-stress.

1.4.5 **β-cell dedifferentiation and loss of mature β-cell function**

Dedifferentiation, or loss of functionally mature identity of β-cells, is an ongoing matter of studies. So far, dedifferentiation has been based on the idea that β-cells lose the

expression of maturity markers such as *Insulin*, *Pdx1*, *Mafa* and *Nkx6-1* [70] and regain the expression of some progenitor-like markers such as *Ngn3* [71]. However, by performing lineage-tracing and RNA-sequencing, newer studies [72] found that dedifferentiation does not describe the reversal back to a progenitor-like type of cell, but rather differs greatly between diabetes types. A new model for dedifferentiation has been proposed, in which, for each type of diabetes, β-cells dedifferentiate in their own way. This model was named the Anna Karenina Model of β-cell maturation [72]. In either case, these two ideas support a paradigm where the loss of β-cell identity during diabetes, not the loss of cells *per se*, contributes to the loss of β-cell mass. Another study provided hints that maintaining β-cells in an immature state might prevent T1DM progression in NOD mice [70]. Further decoding of the key pathways will provide new targets for each type of diabetes to restore healthy function in dysfunctional β-cells by pharmacological treatment [23, 71].

Transdifferentiation or islet cell plasticity describes the ability of specific cell types to express transcription factors (TFs) and hormones that are normally characteristic of other endocrine cell types. When β-cells were ablated in mice, it was found that other cell types such as α- and δ-cells began to produce insulin [73]. A similar phenomenon was found in donor islets from T1DM patients, where other cells types expressed low amounts of insulin [74]. The removal of the expression of *Pdx1,* one major TF, in β-cells of mice did not only lead to severe hyperglycemia, but also changed the transcriptional profile of affected cells, now resembling the profile of α-cells [75]. Taken together, in extreme conditions, such as during long-standing T1DM and chronic hyperglycemia, polyhormonal cells frequently arise [30, 74]. It was therefore hypothesized by multiple groups of scientists that trans- or dedifferentiation protects β-cells from autoimmune destruction or cell death [23, 28, 70, 71]. Remarkably, upon normalization of blood glucose, changes in islet structure and also function could be reversed, further proving the plasticity of islet cells [30]. This knowledge about the transdifferentiation potential of islet cells offers novel opportunities for regenerative therapies. However, more research is needed to ensure translatability to the clinic.

Usually, senescence of β-cells is associated with ageing. However, some studies described premature senescent β-cell subpopulations during hyperglycemic and autoimmunity conditions in NOD mice and T1DM patients. The elimination of this subpopulation was able to stop the autoimmune destruction of β-cells, which indicates a new potential therapeutic approach for T1DM [23, 76].

In summary, it could be shown that islet cells retain a certain plasticity and are able to regain functional maturity. Research on de- and transdifferentiation provides the much-needed knowledge to differentiate induced pluripotent stem cells for regenerative medicine. In addition, the modulation of β-cell identity and function offers promising targets for new therapeutic fields.

1.5 Diabetes – a global epidemic on the rise

As discussed in the previous chapter, diabetes is the result from β-cell dysfunction or loss of β-cells. In 2021, 537 million adults worldwide were living with diabetes mellitus (DM). If numbers continue to rise, around 783 million people will be affected by 2045 [77]. The burden on the health systems worldwide from diabetes and its complications is enormous. By 2030, the total global health expenditure related to diabetes will reach one trillion US dollars [77].

Diabetes is a chronic condition in which the body is either unable to produce enough insulin to maintain normoglycemia or to respond to the insulin it produces, or both, resulting in chronic hyperglycemia. The most common forms of diabetes are type 1 diabetes mellitus (T1DM) and type 2 diabetes mellitus (T2DM), which are complex and heterogeneous diseases. Genetic, environmental and lifestyle factors eventually lead to progressive loss of β-cell function and mass [78]. Less common are monogenic forms of diabetes, making up roughly 1.5-2% of all diabetes patients [77, 79, 80]. These rarer forms usually have clinical similarities to T2DM, but are genetically distinct. Causative mutations occur within a single gene and can happen either spontaneously or are inherited mostly in an autosomal-dominant manner. The environmental contribution is minimal [81].

What all these patients have in common, independent from the type of diabetes, is the risk of developing many associated chronic complications such as retinopathy, neuropathy, kidney damage and cardiovascular diseases, especially if hyperglycemia is not managed well [80]. Different forms of diabetes are discussed below.

1.5.1 Polygenic forms of DM

1.5.1.1 T2DM

The most common form of diabetes is T2DM, making up around 90% of all diabetes cases. T2DM is characterized by the progressive loss of β-cell function and the inability to secrete enough insulin to meet the metabolic demand. The causes are not completely understood, but risk factors include genetic predisposition, lifestyle (including, for example, overeating, obesity and a sedentary lifestyle), ethnicity, family history and age. Nutritional overload in insulin-sensing tissues and subsequent inflammatory effects, changes in hormonal factors and ER-stress lead to the development of insulin resistance

[82]. Often, this goes unnoticed at first, since at early stages the β-cells are still able to compensate by secreting higher levels of insulin. The blood glucose is often only elevated slightly. This condition nowadays is referred to as prediabetes [83]. Eventually though, β-cells are exhausted, resulting in β-cell death and ultimately, T2DM as a result of the depletion of the insulin-producing β-cells [82]. T2DM is most commonly seen in older adults, however younger adults and children are increasingly affected due to physical inactivity, poor diet and obesity. Treatment includes lifestyle interventions and/or oral anti-diabetic medication such as metformin or sulfonylureas. When oral medications do not suffice anymore to maintain normoglycemia, insulin injections are unavoidable [80, 81].

1.5.1.2 T1DM

T1DM is caused by T-cell mediated autoimmune destruction of β-cells, resulting in total insulin deficiency. T1DM patients make up around 5-10% of all cases. However, the etiology of the disease is not yet fully understood. Most likely, a combination of genetic susceptibility together with an additional environmental trigger initiate the autoimmune destruction of β-cells. Viral infections, toxins and few dietary factors are potential environmental triggers. Mostly, the condition develops early in life during childhood. Patients require regular blood glucose monitoring and lifelong treatment with insulin. If monitored closely and managed well, patients can live normal lives and avoid chronic complications. However, in economically disadvantaged countries, access to diabetes education and insulin is often limited. Bad management of the disease can lead to severe disabilities and to the development of diabetic ketoacidosis resulting in early death [78, 80].

1.5.2 **Monogenic forms of diabetes**

The increasing availability and affordability of genetic screening has enabled medical professionals to identify a wide variety of genes that cause monogenic diabetes, with a single mutation in one of these genes leading to diabetes. Symptoms may resemble T1DM or T2DM, however disease onset is generally much earlier in life, which means that patients are often misdiagnosed as T1DM or T2DM. Therefore, the current numbers may be underestimated. If atypical diabetes is found, genetic testing is recommended if, compared to T1DM, there are no autoantibodies or residual β-cell function is still present

after 5 years; or if, compared to T2DM, the diagnosis was made early in life, there are no signs of insulin resistance, the BMI is normal, or one of the parents is also diabetic [84]. Exact diagnosis is of utmost importance as clinical management is very variable. The most common form is maturity onset diabetes of the young (MODY), other forms are neonatal diabetes mellitus (NDM), mitochondrial diabetes and some forms of multi-organ syndromes [32, 81].

An overview of genetic defects of the β-cell that cause diabetes and the subcellular compartments that are affected are shown in the following Figure 6:

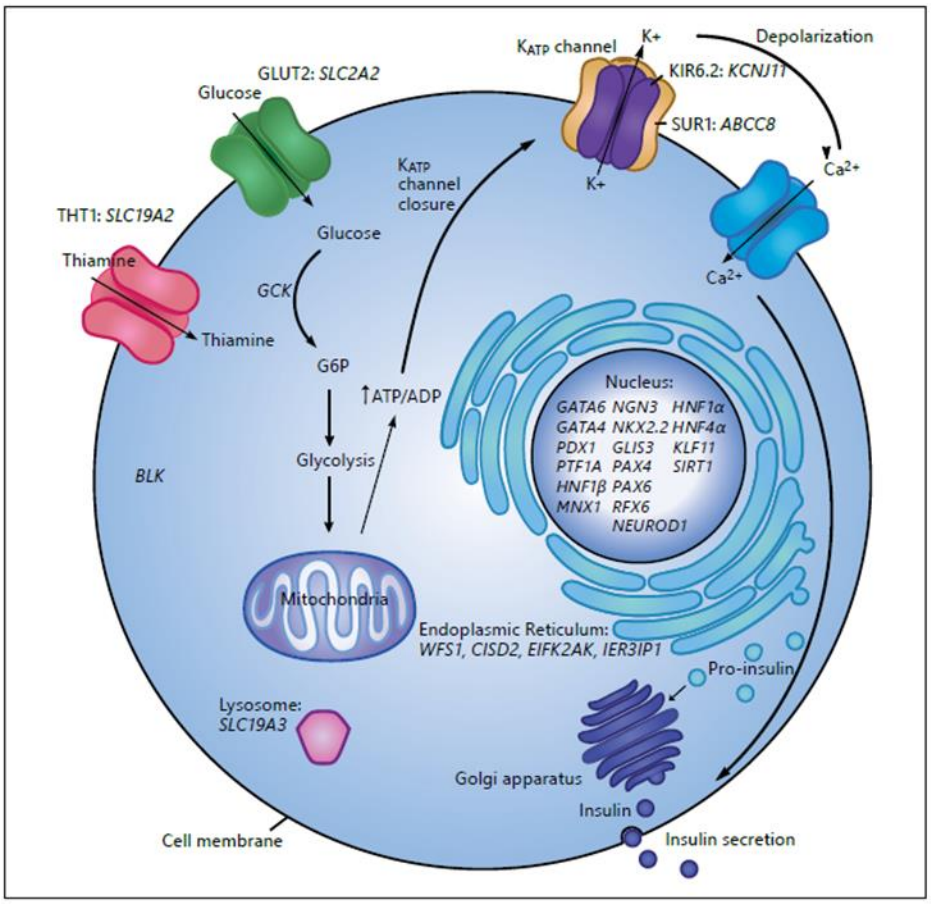

Figure 6 Genetic defects of the β-cell that cause diabetes

The schematic overview of the β-cell shows subcellular localizations and steps within the insulin secretory pathway in response to glucose stimuli (as described in 1.2) in which individual defects can occur. This figure is adapted from Stekelenburg et al., 2016.

1.5.2.1 MODY

The age of onset of MODY is usually between 6 months and 35 years. So far, 14 different subtypes have been defined. Depending on the genes affected, the phenotypes are very

variable. Most common are HNF1A-MODY (MODY3), HNF4A-MODY (MODY1) and GCK-MODY (MODY2) [32, 81]. Subject of this study are mouse models for MODY1. MODY1 is described in detail in section 1.6.3.

1.5.2.2 NDM

Neonatal diabetes mellitus (NDM) usually occurs very early within the first 6 months of life, less often between 6 months and a year. With 1 in 90,000 live births, NDM is a rare disease [85]. Two forms of NDM are distinguished. More common is transient NDM (TNDM), which usually resolves after about 4 months. In contrast, permanent NDM (PNDM) requires lifelong treatment. Clinically, NDM is more similar to T1DM, as it is often accompanied by ketoacidosis, making differential diagnosis difficult. It is therefore recommended to perform genetic testing in patients who show symptoms of diabetes before 180 days of age in order to identify a possible mutation in a diabetes-causing gene [32].

One subject of this study are mouse models with mutations in the *Insulin2* (*Ins2*) gene. Mutations in the human *INS* gene are the second most prevalent cause of PNDM [86] and are described in more detail in 1.6.1. A further subject of this study are mouse models with mutations in the *Pdia6* gene [87]. More details are described in 1.6.2.

1.6 Forms of monogenic diabetes investigated within the scope of this thesis

1.6.1 Neonatal diabetes caused by *INS* mutations (MIDY)

INS mutations are the second most prevalent cause of PNDM and make up around 8% of all cases. Sometimes, the disease is also referred to as mutant *INS*-gene induced diabetes of youth (MIDY) [36, 43]. Some patients show a milder phenotype with a later onset that resembles more that of a MODY [86]. Up to date, more than 90 dominantly-acting mutations have been identified in all regions of the preproinsulin molecule [86]. In more than 50% of the cases, the affected amino acid residues are associated with the formation of the three disulfide bonds. Mutations in the *INS* gene negatively impact biosynthesis, folding and the 3D structure of insulin molecules. Mutant proinsulin molecules accumulate in the ER and activate the ER-stress response (see 1.4.2),

resulting ultimately in β-cell apoptosis [86]. Patients are lifelong dependent on insulin treatment.

A lot of research regarding MIDY is performed in cell lines and rodent models. Rodents, however, have two non-allelic insulin genes, *Ins1* and *Ins2*, which compensate for each other if one of them is lost [88]. In contrast, humans have only one *INS* gene [29]. In the past years, several mouse models with *Ins2* mutations have been established: *Ins2*Akita (C96Y) [89], Munich*Ins2* (C95S) [90], KINGS (G32S) [91] and *Ins2*(Q104del) [92] (Figure 7). Akita and Munich*Ins2* mice both harbor cysteine mutations that affect the disulfide bonds A7-B7 and A6-A11, respectively. Their phenotype is very prominent with severe early-onset hyperglycemia [89, 90]. The phenotype in the two above-mentioned models with non-cysteine mutations is generally milder [91, 92]. In KINGS mice, only a modest retention of G32S proinsulin in the ER was observed with no effect on the β-cell mass [91].

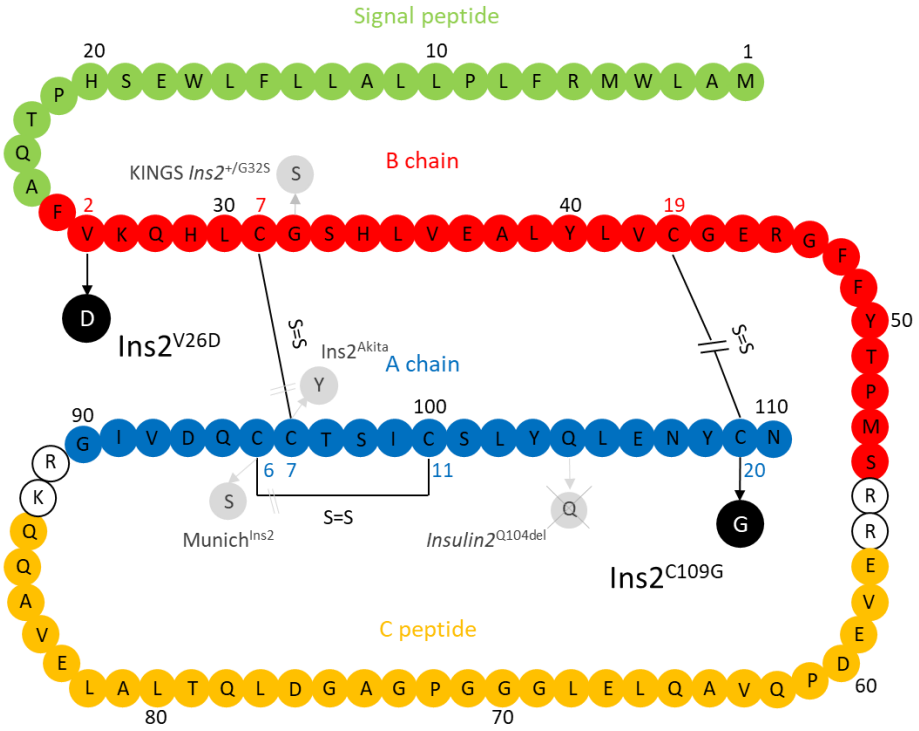

Figure 7 Amino acid sequence of the preproinsulin molecule

Amino acid (AA) sequence of the preproinsulin molecule is numbered in black letters (1-110). The sequence was obtained from https://www.uniprot.org/uniprot/P01326. **Green:** Signal peptide (AA1-24); **Red:** B-chain (AA25-54); **Yellow**: C-peptide (AA57-87); **Blue**: A-chain (AA90-110). AA of the A- and B-chain are numbered in red and blue, respectively. Included are disulfide bridges (S=S) (A7-B7; A20-B19; B6-B11). Mutations of the novel mouse models (*Ins2*^{V26D}, *Ins2*^{C109G}) are shown in black circles. Previously existing mouse models are shown in grey circles (KINGS Ins2$^{+/G32S}$, Munich^{Ins2}, Ins2^{Akita}, *Insulin2*^{Q104del}).

In vitro and *in vivo*, the Akita proinsulin is by far the most investigated. In rodent models and in β-cell lines it has been shown that mutant C96Y proinsulin formed aberrant, disulfide-linked high-molecular weight complexes (HMW) with wild-type proinsulin in the ER, which effectively hindered the exit of healthy molecules and induced swelling of the ER with severe ER-stress, ultimately resulting in the loss of β-cell mass [39]. Several ER-stress markers were found to be increased in Akita cells [93, 94], whereas *Ero1b* was found to be decreased [62]. In all *Ins2* models, sexual dimorphism was observed in which female mice were only slightly affected. This observation can be explained at least in part by protection through endogenous estrogen [95].

Taken together, other mutations beside Akita are only poorly researched, but humans are affected by a variety of different mutations, which offers many opportunities for future studies. In addition, there is no comprehensive study that evaluates all findings *in vivo*.

1.6.2 **Potential neonatal diabetes caused by *Pdia6* mutations**

PDIA6, a lesser known and characterized member of the PDI family (see chapter 1.4.3) is ubiquitously expressed in both humans and mice [96]. Complete ablation of PDIA6 in a mouse model led to prenatal lethality [97]. PDIA6-deficient HeLa cells were shown to be hyper-responsive to ER-stress by consistent activation of IRE1α-target genes, which finally led to apoptosis [98].

In β-cells, PDIA6 has been shown to associate with misfolded proinsulin and possibly play a role in the clearance of misfolded proteins [58, 63, 64]. The absence of PDIA6 in INS-1 cells increased the ER-stress response, but did not affect the folding or disposal of insulin [98]. Instead, the *Ins1* and *Ins2* expression was reduced because IRE1α was persistently active [60], which directly influenced the insulin transcript abundance. These *in vitro* experiments suggest an influence of PDIA6 on the β-cell function also *in vivo*. In fact, in a recent study with an ENU-induced point mutation in the first thioredoxin domain of PDIA6, researchers reported severe developmental defects, loss of PDIA6 protein, decreased *Ins2* expression, and altered insulin tolerance [97]. However, other effects on β-cell development and function remained unevaluated. Further support for the involvement of PDIA6 in β-cell function is provided by a study on a T1DM mouse model, where *Pdia6* was found to be deregulated before the advent of diabetes [99]. These

finding suggests that mutations in PDIA6 might lead to neonatal diabetes also in humans. Our lab has generated a mouse model with a *Pdia6* point mutation in the second thioredoxin domain (Pdia6^{F175S}), which is also subject in this thesis and was published recently [100].

1.6.3 MODY1 caused by *HNF4A* mutations

MODY1 patients usually present with young-onset diabetes (typically before 25 years of age) with impaired insulin secretion. Macrosomia is found in approximately 50% of affected newborns. In most cases, patients are sensitive to sulfonylurea treatment and do not require insulin until later in life. In very rare cases, patients also have transient neonatal hypoglycemia due to hyperinsulinemia. MODY1 is caused by mutations in the *HNF4A* gene, including missense, frameshift, nonsense, splicing or promoter mutations [81, 101, 102].

Hepatocyte nuclear factor 4 alpha (HNF4A) is an orphan member of the nuclear receptor family of ligand-activated transcription factors that binds DNA as a homodimer [101]. It is mainly expressed in the liver, intestines, pancreas, kidney and stomach. The expression levels are not the same in different tissues, for example the expression in pancreatic islets is lower than in the liver. This possibly explains why MODY1 patients present with GSIS defects but have only mild liver dysfunction [103]. Two alternative promoters (P1 and P2) enable the expression of 9 tissue- and development-specific isoforms [104-106].

In the pancreas, HNF4A, together with HNF1A, has been shown to regulate β-cell function. HNF4A expression in islets has been reported to be dependent on HNF1A, linked in a hierarchical regulatory relationship. Both TFs regulate a similar set of genes, are interdependent, and synergistically regulate common targets [103, 107, 108]. Individually, HNF4A was found to be essential for β-cell function and the maintenance of glucose homeostasis [107].

The exact mechanism why HNF4A mutations cause defective insulin secretion resulting in diabetes remains unclear, however some evidence suggests that altered function of the K_{ATP} channel (for the role of the K_{ATP} channel in insulin secretion confer to 1.2) seems to be involved [109]. Reduced expression of one of its subunits in *Hnf4a*-deficient β-cells suggests a similar thing [110]. Further, HNF4A was shown to be in a functional interplay

with PDX1, which in turn is important for β-cell identity (see also 1.3) [111]. Deletion of HNF4A in β-cells resulted in impaired GSIS, but paradoxically also to hyperinsulinemia in fasted and fed states and not to a diabetic phenotype [110, 112]. The expression of a defective form of HNF4A in INS-1 cells altered the expression of, for example, *Insulin* and *Glut2*, whereas overexpression of the wild-type form increased the GSIS capacity, e.g. by increasing *Glut2* [103].

HNF4A is an important TF in many tissues and it is therefore not surprising that homozygous disruption in mice lead to early embryonic death (E6.5) [113]. However, heterozygous ablation did not produce any phenotype in mice [114]. So far, only models with targeted deletions in the pancreas [108] or only in β-cells were viable [110, 112] and showed mild phenotypes. Upon a comprehensive analysis, Harries et al. found significant differences in the expression of HNF4A and HNF1A between rodents and humans, which are much higher in rodents [115]. The potential effects and conclusions resulting from this discovery are discussed in detail in the discussion part of the thesis.

Within the scope of this thesis, by applying a variety of different approaches, I aimed to identify at least one suitable mouse model that reflects the human MODY1 phenotype. The results are given in chapter 4.3.

1.7 Current therapy for monogenic diabetes

As mentioned before, the various types of diabetes are often first treated with lifestyle interventions and oral anti-diabetic drugs such as sulfonylureas, metformin or GLP-1 receptor agonists [116]. However, patients develop unresponsiveness to these treatments with progression of the disease and, eventually insulin treatment is necessary for the rest of life [78]. In monogenic diabetes, which is the result of a genetic mutation, drugs and lifestyle interventions however do not address the underlying genetic defects. Patients are life-long dependent on medication, some of them from a very young age as exemplified in patients with PNDM, where disease onset is before 2 years of age (see 1.5.2.2). Therefore, novel treatment options are urgently needed. The genetic cure of monogenic diabetes has never been attempted before. Yet, transfer of therapeutic genes to the pancreas could *per se* be curative and benefits compared to existing therapies are

to be expected. A one-time treatment comes with the prospect of lifelong beneficial effects.

1.8 Gene therapy for monogenic diabetes using rAAVs

1.8.1 What is gene therapy?

The idea of gene or cell therapy has come up in the early 1970ies and has first been attempted in the late 1980ies [117]. Ever since, with the development of many novel tools and general advancements especially in the last 10 years, the field has accelerated substantially. Gene/cell therapy describes a highly specific and precise procedure that has the intent to fix a genetic problem. For example, if a dysfunctional protein is produced by a mutated gene, a healthy copy of the gene that was artificially introduced, e.g., by a vector, can take over and produce a functional protein, thereby providing a therapeutic effect. This technique is suitable for monogenic diseases, particularly those where drug treatment is not satisfactory such as blindness or hemophilia. Options include either *ex vivo* treatment, where samples are taken form the patient, treated and cells are returned to the system, or vectors can be directly delivered *in vivo. In vivo* delivery requires a suitable method for direct delivery to the organ/cell or potential options for systemic administration [118]. Transfer of mRNA or DNA to cells has been attempted by a variety of non-viral (e.g., in cationic liposomes) and viral gene transfer methods. The choice of the right vector is one of the biggest challenges, since the wrong one can lead to death [119]. Until 2017, around 2600 clinical trials were conducted and few products have been successfully approved for the market, e.g., GlyberaR®, a recombinant adeno-associated viral vector for the treatment of lipoprotein lipase deficiency or Strimvelis®, a lentiviral vector for the treatment of a severe immunodeficiency [118, 119].

1.8.2 rAAV vectors

In clinical trials either lentiviruses or adeno-associated viruses were utilized [120]. Adeno-associated viruses (AAVs) are small, single-stranded DNA viruses of about 4.8 kb of length and contain three genes, *Rep* (replication), *Cap* (capsid) and *aap* (assembly), encoding for at least nine gene products by different promoters, translation start sites and alternative splicing. These genes are flanked by inverted terminal repeats (ITRs) [121]. AAVs, which lack pathogenicity and have a low immunogenicity, efficiently transduce

dividing and non-dividing cells and do not integrate into the genome, but persist as episomes in the cytoplasm or nucleus of transfected cells and mediate long-term transgene expression [121]. In the case of recombinant AAVs (rAAVs), which are used for gene therapies and are replication deficient, the coding region is replaced by an expression cassette, which, together with the remaining ITR regions, must not exceed 4.7 kb [122].

Different virus serotypes show tropism for different cell types and tissues [123]. By choosing the right serotype and promoter for the expression cassette, the expression of therapeutic genes can be directed specifically, for example to the β-cell. So far, no associations of AAVs with human diseases have been reported, which is why rAAVs are considered safe and efficient vectors for gene therapy [121]. Proof of efficacy has been demonstrated in several animal models, for example in mice or dogs [124-126], and in humans for several organs, such as the liver [127, 128] or the eye [129]. Although rAAVs have proven to be safe and highly efficient vectors for gene therapy, not all hurdles have been overcome. For example, during the first clinical trials there were indications of pre-existing immunity to AAVs in humans. A pre-check of immunogenicity against AAV serotypes as well as a capsid and genome engineering of rAAVs are possible solutions to avoid immune reactions in humans [130, 131].

1.8.3 Gene transfer to the pancreas and diabetes treatment

The successful treatment of diabetic animal models with rAAVs has already been demonstrated. The rAAV-mediated co-expression of insulin and glucokinase in skeletal muscles of diabetic dogs corrected the hyperglycemia [132] and the rAAV-mediated expression of FGF21 in liver, adipose tissue and skeletal muscle improved obesity and corrected the insulin resistance of ob/ob mice [125]. The pancreas, however, is a complex organ and pancreatitis as a result of treatment is a major concern. Previous experiments with systemic delivery of AAV only led to a short-term transduction of β-cells [133]. The transfer of the surgical technique of endoscopic retrograde cholangiopancreatography from humans to mice for intraductal delivery led to a more localized gene expression in the pancreas [134]. Further experiments comparing different AAV serotypes demonstrated that intraductal delivery of serotypes 6, 8 and 9 efficiently transduced β-

cells and the exocrine pancreas [135]. In 2017, it was finally shown that the AAV8-mediated overexpression of *Igf1* in the pancreas counteracted autoimmune diabetes in the NOD mouse model, which further proves its feasibility [126]. To further limit expression of the therapeutic gene to β-cells, a β-cell specific promoter can be used. Several different rat and mouse insulin promoters (RIP and MIP) have been tested experimentally [136]. Finally, our collaborators at UAB demonstrated that the usage of a specifically engineered human insulin promoter led to a highly efficient β-cell specific expression of a selected gene in mice (Fatima Bosch, personal communication). The efforts of our partners at UAB have clearly shown that the selection of the right promoter has an enormous impact on the strength and effectiveness of the expression of the therapeutic gene of interest. Therefore, careful consideration must be given to which type of promoter should be used in order to achieve the desired expression and not cause any toxic effects. Further, the gene dose has to be evaluated carefully. One dose containing 5×10^{11} vg (viral genomes) has been shown to transduce all β-cells (Fatima Bosch, personal communication).

In summary, it can be said that gene therapy for monogenic diabetes by intraductal delivery of specially designed rAAV8 vectors containing a correspondingly strong promoter appears feasible in order to deliver therapeutic genes to β-cells.

2. Aims and objectives of the study

2.1 *Ins2* project

While a lot of information on *INS* and *Ins2* mutations is available in parts in several publications, most data has been generated in β-cell lines and only some aspects have been verified in mouse models. A comprehensive study examining most of these points *in vivo* in more than just the Akita mouse model is lacking so far. In humans, many insulin mutations are known at many different positions and not all of them affect disulfide bonds, but the phenotype is present and severe [86]. In the frame of this thesis, I hope to close this gap in knowledge by evaluating two new different *Ins2* mouse models, one with and one without a cysteine mutation, and compare results to detect differences to existing models. To achieve this, $Ins2^{C109G}$ and $Ins2^{V26D}$ mice were closely monitored for 18 weeks with regular checks of body weight, blood glucose and plasma hormone levels. Insulin tolerance tests (ITT) were performed to determine insulin sensitivity at two time points. At the age of 8 weeks, organs were withdrawn for *in vitro* analysis including immunofluorescent staining and TEM imaging of pancreatic sections as well as gene and protein analysis in isolated pancreatic islets, covering the evaluation of the state of islets and the β-cells specifically, ER-stress, oxidative stress and autophagy.

2.2 *Pdia6* project

PDIs are important molecules facilitating insulin folding in β-cells. Within the protein family, relatively little is known about PDIA6. Some *in vitro* experiments suggested involvement of PDIA6 in β-cell function. One study reported a mouse model with a V32A point mutation in PDIA6 showing loss of PDIA6 protein and altered glucose metabolism [97]. However, many molecular aspects of β-cells remained unexplored in this study, which focused on the concomitant immunodeficiency.

To shed more light on the involvement of PDIA6 in β-cell development and function, a new mouse model with a F175S mutation ($Pdia6^{F175S}$) was analyzed in detail within this thesis. Besides *in vivo* experiments, immunofluorescent staining was applied to pancreatic tissues sections, protein expression was analyzed in pancreatic tissue and gene expression was analyzed in isolated islets. The focus was to evaluate the state of

the islets and especially of the β-cells covering the aspect of β-cell dedifferentiation, oxidative state of the islets and ER-stress.

2.3 MODY1 and gene therapy project

A lot of information is available about MODY1 patients, their mutations and phenotypes, and about treatment options. However, to the best of our knowledge, there is no mouse model published that reproduces the human phenotype.

As part of a multi-center project on MODYs, our group aimed to identify a mouse model that closely mirrors the human MODY1 phenotype and subject it to an innovative gene therapy approach using a rAAV8 vector to treat β-cells.

In this work, six different *Hnf4a* mouse models were phenotyped, one of which was additionally subjected to rAAV8-mediated gene therapy as proof of concept. Animals were monitored *in vivo* for phenotypic variation e.g. by regular checks of the blood glucose levels. *In vitro* analysis of pancreatic islets and the liver were performed to evaluate the expression of genes and proteins associated with *Hnf4a*. One model with significant decrease of *Hnf4a* expression in islets was chosen for gene therapy treatment.

3. Material and Methods

3.1 Materials

3.1.1 Chemicals

Table 2 List of chemicals

Chemical	Supplier	Ordering number
Ampuwa® (ultrapure H_2O)	Fresenius Kabi	B230672
BSA	Sigma Aldrich	A3311-100G
Collagenase P	Sigma Aldrich	11213873001
dH_2O	From lab water supply	
EDTA	Sigma Aldrich	ED2SS 1kg
Absolute Ethanol (EtOH)	Sigma Aldrich	1.00983
FBS	Gibco	26140079
Glucose solution (20%)	B. Braun	2356746
HCl	Carl Roth	9277.1
HEPES solution (1 M)	Sigma Aldrich	28973.363
Horse serum (heat inactivated)	Gibco	26050088
KCl	Merck	1.049.361.000
KH_2PO_4	Merck	1.048.731.000
Methanol (MeOH)	Sigma Aldrich	1.06009
$MgCl_2$	Merck	8.147.330.500
Mineral Oil	Sigma Aldrich	M5904-500ML
NaCl	Merck	1.064.045.000
0.9% NaCl solution for injections	B. Braun	02737756
Na_2HPO_4	Th.Geyer	86641000
NP40	Invitrogen	FNN0021
OptiPrep™ Density Gradient Medium	Sigma Aldrich	SI D1556-250ML
PFA	Sigma Aldrich	P6148-1KG
Pluronic™ F-68	Thermo Fisher Scientific	24040032
QIAzol Lysis Reagent	Qiagen	79306
Trizma base	Sigma Aldrich	T1503-1KG
Tween®-20	VWR	KRAF21440.2000
Triton™ X-100	Sigma Aldrich	T9284
Xylene	VWR	28973.363

3.1.2 Buffers and solutions

3.1.2.1 Genotyping

Table 3 Lysis buffer for genotyping

Lysis Buffer	Final concentration	for 500 ml
Tris pH 8.3	10 mM	3.3 ml 1.5 M Tris
$MgCl_2$	2.5 mM	0.625 ml 1 M $MgCl_2$
KCl	50 mM	1.863 g KCl
H_2O		Dissolve in 489.712 mL H_2O
		autoclave
NP40	0.45% (v/v)	2.25 ml NP40
Tween®-20	0.45% (v/v)	2.25 ml Tween-20
		Add after autoclaving, store at 4 °C

3.1.2.2 Tissue fixation and immunofluorescent staining

Table 4 Buffers for tissue fixation and immunofluorescent staining

Buffers and solutions	Final concentration	Recipes
PBS pH 7.4 (1x)	137 mM 2.7 mM 10 mM 1.8 mM	NaCl KCl Na_2HPO_4 KH_2PO_4 Dissolve in dH2O, adjust pH to 7.4 with HCl/NaCl
PBS-T (Wash buffer)	0.1%	Tween®-20 in 1x PBS
4% PFA ≈ 10% Formalin	4%	PFA (Sigma) in 1x PBS prepare fresh on day of use; heat PBS until too hot to touch, remove from heat, add PFA under fume hood and stir until dissolved; let cool down, store under fume hood until use
Immunofluorescence buffer		1% BSA 5% Horse Serum 0.3% Triton X-100 in 1x PBS
Tris-EDTA Antigen Retrieval buffer (pH 9)	10 mM 1mM 0.05%	Tris Base EDTA Tween®-20 In 1.5L dH_2O

3.1.2.3 Islet isolation, cultivation, lysis

Table 5 Buffers for islet isolation, cultivation and lysis

Buffers and solutions	Recipes
G-solution	500 mL HBSS with calcium, magnesium, no phenol red (Life technologies; 14025092) 5 mL antibiotic-antimycotic solution (Sigma Aldrich) 5 g BSA Dissolve, then sterile-filter; store at 2-8 °C for up to 1 month
Collagenase solution	Dissolve 1 mg/mL of Collagenase P (Roche) in G-solution 8 mL are needed per mouse
RPMI Medium	445 mL RPMI 1640 medium with UltraGlutamine (Lonza) 5 mL antibiotic-antimycotic solution (Sigma Aldrich) 50 mL fetal bovine serum (Gibco) store at 2-8°C for up to 3 months
10% RPMI	5 mL RPMI medium 45 mL G-solution store at 2-8°C for up to 1 month
Optiprep	20 mL OptiPrep™ Density Gradient Medium (Sigma Aldrich) 9.7 mL DBPS (Lonza) 300 µL 1M HEPES (Lonza) store at 2-8 °C for up to 1 month
Optiprep/RPMI	5 mL Optiprep for islet isolation 3 mL 10% RPMI Prepare fresh on the day of use
Acid ethanol (0.18 M HCl in 71% EtOH)	375 mL absolute Ethanol (Merck) 117.5 mL dH_2O 7.5 mL concentrated HCl (x) Store at -20°C

3.1.2.4 Protein isolation and western blotting

Table 6 Buffers for protein isolation and western blotting

Buffers and solutions	Recipes
RIPA buffer	10 mL of RIPA Lysis and Extraction buffer (Thermo Fisher #89901) were supplemented with 1 tablet cOmplete® Mini Protease Inhibitor Cocktail (Roche) 1 tablet PhosSTOP™ (Roche)
Running buffer	50 mL SDS MES Running Buffer (20x) (Life technologies) 950 mL dH_2O

Transfer buffer	50 mL Transfer Buffer (20x) (Life technologies) 200 mL MeOH 750 mL dH_2O
Blocking buffer	Intercept Blocking Buffer (TBS) (Li-COR)
TBS (1x)	50 mL Pierce™ 20X TBS Buffer (Thermo Fisher) 950 mL dH_2O
TBS-T	0.1% Tween® 20 (Sigma Aldrich) in 1x TBS

3.1.3 Consumables and kits

Table 7 Consumables

Consumable	Company	Order number (if applicable)
384-well plates	Roche	04729749001
96-well plates	Fortitude	
Chirlac (suturing material)	CHIRANA T. Injecta	PG0203-2
Contour®Next One + sensors	Ascensia Diabetes Care	
Corning® Cell strainer pore size 70 µm	Sigma Aldrich	CLS431751-50EA
Corning® filter system pore size 0.22 µm	Sigma Aldrich	CLS431097-12EA
Coverslips 24x50mm	Roth	5000510
Deepwell, 1.1 mL plates	VWR	732-3322
Gloves (Nitril NextGen)	Meditrade	5000445
Lab wipes	Kimtech Science	7558
Microvette CB 300 LH (Lithium-Heparin)	Sarstedt	16.443
Microvette CB 300 EDTA K3 (Kalium-EDTA)	Sarstedt	16.444
Pasteur pipettes	Sarstedt	5000416
Pipette tips 200-1000 µL, 200 µL, 100 µL, 0.5- 20 µL, 0.2-20 µL	Biosphere	5001194, 5001563, 5001565
Reaction tubes 50 mL, 15 mL	Sarstedt	5000755;
Reaction Tubes, Safe Lock; 2 mL, 1.5 mL, 0.5 mL	Sarstedt	5000634; 5000631; 5000445

Serological pipets 50 mL, 25 mL, 10 mL, 5 mL	Greiner	5000549; 5000550; 5000551; 5000552
S-Monovette	Sarstedt	
SuperFrost® Plus slides	VWR	5000504
Syringes (OMNICAN 50 0.5ML 0.30X8MM G30x1/2)	Neolab	9151117

Table 8 Kits

Kit	Company	Order number
C-peptide ELISA	BioCat	EKL56453-BM
Insulin ELISA	Mercodia	10-1247-10
Glucagon ELISA	Mercodia	10-1281-01
High Pure Viral NA Large Volume Kit	Roche Diagnostics	5114403001
Micro BCA™ Protein Assay Kit	Thermo Fisher	23235
Pierce™ BCA Protein Assay Kit	Thermo Fisher	23227
Proinsulin ELISA	Mercodia	10-1232-01
QuantiFast SYBR Green PCR Kit	Qiagen	204057
RNeasy Plus Micro Kit	Qiagen	74004
Superscript IV First-Strand Synthesis System	Thermo Fisher	18091050

3.1.4 Laboratory equipment

Table 9 Laboratory Equipment

Equipment	Supplier
Axio Imager M2 (Microscopy)	Zeiss
AxioScan.Z1	Zeiss
Centrifuge (plates)	Eppendorf
Centrifuge (small tubes)	Heraeus
Centrifuge (bigger tubes)	Hettich
Centrifuge (small tubes, cooled)	Heraeus/Thermo Fisher
ClipTip pipette	Thermo Fisher
Cold room	Integrated into the building
Fine scale	Ohaus
Freezer -20°C	Liebherr

Fridge +4°C	Liebherr
Glassware	Schott
Incubator (Cell culture)	Heraeus
Isoflurane Machine	Zevenaar Holland
Lightscanner	Idaho Technology
LSM880 (Confocal microscope)	Zeiss
Magnetic stirring plate	IKA Labortechnik
Matrix pipettes (30 µL, 125 µL)	Thermo Fisher
Microtome	Thermo Scientific
Multichannel pipettes	Dunn
NanoPhotometer®	Implen
PCR cycler	Tetrad
pH meter	Fisher Scientific
Pipettes	Eppendorf Research® plus (P1000, P200, P100, P20, P10, P2.5)
Ring-light	Leica
Rocking Platform	VWR
Scale (laboratory)	Ohaus
Scale (mouse work)	Sartorius
Sonicator	Apogent Discoveries
Stereomicroscope	Leica
Sterile work bench	Schulz Lufttechnik GmbH
Timer	Roth
Tools for mouse work/surgery	Fine Science Tools
Varioskan LUX (Plate Reader)	Thermo Fisher
Vortexer	Neolab
Water bath	Julabo

3.1.5 PCR and RT-qPCR primer pairs

3.1.5.1 PCR primer pairs for genotyping

Table 10 Genotyping primer pairs

Mouse line	forward	reverse
Ins2^{C109G}	GCGTGGCATTGTAGATCAG	GTGCTCATTCAAAGGTTTTATTCA
Ins2^{V26D}	GCCTATCTTCCAGGTTATTGTTT	GTGTAGAAGAAGCCACGC
Hnf4a^{tm1b}	ACTGGAGGCTGAAGTTCAGAT	GCGTTTCACCCTGCCATAA
Hnf4a^{R333L}	GGTTAGGAGTCATTCGGTCT	GAACTGGATCTGTTCGATCA
Hnf4a^{G124A}	GATAAGAGGAACCAGTGTCG	CCTGTCACAGAGCCATAAAG
Hnf4a-KI	CGATCACCAAGCAAGAAGCC	CTGAGGGTATGAGCCAGCAG
Pdia6^{F175S}	GTCATGTTGCTGTGACAGG	TCCACACCACGGAGCATA
Vector Shedding	CGATCACCAAGCAAGAAGCC	CTGAGGGTATGAGCCAGCAG

3.1.5.2 RT-qPCR primer pairs for gene expression analysis

Table 11 Housekeeping genes primer pairs

Gene	forward	reverse
Actb	GCCACCAGTTCGCCAT	CATCACACCCTGGTGCCT
Atp5b	GGTTTGACCGTTGCTGAATAC	TAAGGCAGACACCTCTGAGC
B2m	GCTATCCAGAAAACCCCTCA	GGGGTGAATTCAGTGTGAGC
Cyc1	CGGGAAAGTAAGGGTTGAAATAG	GTTCGAGCTAGGCATGGTG
Fbxw2	ATGGGTCACCAAGGTGGTT	TCCCAATTGGCCAAATCTT
Gapdh	CATTGTCATACCAGGAAATGAGC	TGGAGAAACCTGCCAAGTATG
Hmbs	GCTGAAAGGGCTTTTCTGAG	TGCCCATCTTTCATCACTGT
Rpl13a	TGAAGCCTACCAGAAAGTTTGC	GCCTGTTTCCGTAACCTCAA
Sdha	GCAATTTCTACTCAATACCCAGTG	CTCCCTGTGCTGCAACAGTA
Tbp	CCCCACAACTCTTCCATTCT	GCAGGAGTGATAGGGGTCAT
Tuba1a	AAGGAGGATGCTGCCAATAA	GCTGTGGAAAACCAAGAAGC
Ubc	GCAGATCTTTGTGAAGACCC	GAAGGTACGTCTGTCTTCCT
Ywhaz	TGCAGCCAGAAGAATATCCA	AAGAGACAGTACATCGTTGCAGA

Table 12 RT-qPCR primer pairs

Gene	forward	reverse
Abcc8	TCAACTTGTCTGGTGGTCAGC	GAGCTGAGAAAGGGTCATCCA
Atf6	GAGTCAGTCCATGTTCTGTTT	CGTTCCTGAGGAGTTGGAT
Brn4	CGAGAACACGTTGCCATAC	CCAACCTCTGATGAGTTGGAA
Ddit3	ATATCTCATCCCCAGGAAACG	TCTTCCTTGCTCTTCCTCCTC
Eif2ak3	TTCCACTTCTCACTGCCG	AGTGGAAAGCTGAGGTATATCT
Ero1a	TCTGAAGCTTGCCCCAC	GATACTTCATGAAATCAAGTCATTTCC
Ero1b	CACGCTAAGTAACGAAAGCAA	CCGCTCATCATCAAGTTCAC
Gcg	AGGCTCACAAGGCAGAAAAA	CAATGTTGTTCCGGTTCCTC
Gck	CTGTTAGCAGGATGGCAGCTT	TTTCCTGGAGAGATGCTGTGG
Ghrl	AGGCTCCAGCTTCCTGA	GTTTAGCTGGTGGCTTCTTG
Hnf1a	GGTCCACGGTGTACGGTA	GTGGCTGAGACCAGCTT
Hnf4a_1	GTTCTGTCCCAGCAGATCACC	CTTCTTTGCCCGAATGTCGC
Hnf4a_2	CGTGCTGCTCCTAGGCAATG	CATCGAGGATGCGGATGGAC
Hspa5	GTTCTTGAACACACCGACGC	GTGTGTGAGACCAGAACCGT
Ins1	GCAAGCAGGTCATTGTTTCA	CACTTGTGGGTCCTCCACTT
Ins2	CAGCAAGCAGGAAGCCTATC	GCTCCAGTTGTGCCACTTGT
Ire1a	CTGTGGTCAAGATGGACTGG	GAAGCGGGAAGTGAAGTAGC
Kcnj11	AAGGGCATTATCCCTGAGGAA	TTGCCTTTCTTGGACACGAAG
Mafa	CAGCAGCGGCACATTCTG	GCCCGCCAACTTCTCGTAT
Mafb	CTTCACGTCGAACTTGAGAAGG	TAGCGATGGCCGCGGAG
Map1lc3	TAAGATCCCGGTGATCATCG	GGCGCCGGATGATCTTGA
Neurog3	GTCGGGAGAACTAGGATGGC	GGAGCAGTCCCTAGGTATG
Pdia1	CAAGATCAAGCCCCACCTGAT	AGTTCCCCCCAACCAGTACTT
Pdia4	AGCTCCTTGGCAGCTTTCTC	TGCAGACATTATTTTGGTGGA
Pdia6	TGGCTCCAGGTTTTTGCAGT	ATTGTAGATGCCGCCCTCAG
Pdx1	CAGTGGGCAGGAGGTGCTTA	GCCCGGGTGTAGGCAGTAC
Ppy	GGCCTAGGTATGGGAAGAGA	CAGGGAATCAAGCCAACTG
Slc2a2	GGGGACAAACTTGGAAGGAT	TGAGGCCAGCAATCTGACTA
Sqstm1	CCTACAGCTGAGTCAGCTT	ACATCAATGTCAACCTCAATGC
Sst	ACCGGGAAACAGGAACT	CATCTCGTCCTGCTCAG
Ucn3	GCTGTGCCCCTCGACCT	TGGGCATCAGCATCGCT

Xbp1 (u+s)	ACACGCTTGGGAATGGACAC	CCATGGGAAGATGTTCTGGG
Xbp1 (s)	CAAAAGGATATCAGACTCAGAATC TGAA	GAGTCCGCAGCAGGTGC

3.1.6 **Antibodies**

3.1.6.1 Antibodies for immunofluorescent staining

Table 13 Primary and secondary antibodies for immunofluorescent staining

Primary antibody	Host	Working dilution	Company	Catalogue number
Calnexin	goat	1:200	Novus biological	NBP1-37774
Calreticulin	rabbit	1:200	Abcam	ab92516
Cleaved Caspase 3	rabbit	1:200	Cell Signaling	#9664
Glucagon	mouse	1:1000	Sigma Aldrich	G2654
GRASP65	rabbit	1:200	Invitrogen	PA3-910
Insulin	rabbit	1:500	Cell Signaling	#3014
Insulin	mouse	1:300	Abcam	ab6995
KI-67	rabbit	1:200	Cell Signaling	#12202
NKX6-1	goat	1:200	R&D Systems	AF5857-SP
Proinsulin	mouse	1:200	DSHB	GS-9A8
P62	rabbit	1:200	Cell Signaling	#5114

Secondary antibody	Host	Working dilution	Company	Catalogue number
AlexaFluor® 488 anti-rabbit	donkey	1:500	Life technologies	A-21206
AlexaFluor® 488 anti-mouse	donkey	1:500	Life technologies	A-21202
AlexaFluor® 488 anti-goat	donkey	1:500	Life technologies	A-11055
AlexaFluor® 594 anti-rabbit	donkey	1:500	Life technologies	A-21207
AlexaFluor® 594 anti-mouse	donkey	1:500	Life technologies	A-21203
AlexaFluor® 647 anti-mouse	donkey	1:500	Life technologies	A-31571
AlexaFluor® 647 anti-rabbit	donkey	1:500	Life technologies	A-31573
DAPI (nuclear dye)		1:1000	Sigma Aldrich	D9542

3.1.6.2 Antibodies for western blot

Table 14 Primary and secondary antibodies for western blot

Primary antibody	Host	Working dilution	Company	Catalogue number
α-Tubulin	mouse	1:5000	Abcam	ab7291
α-Tubulin	rabbit	1:5000	Abcam	ab4074
BiP (Grp78)	rabbit	1:1000	Proteintech	11587-1-AP
CHOP	mouse	1:1000	Cell Signaling	#2895
HNF4A	rabbit	1:1000	Abcam	ab199431
IRE1A	rabbit	1:1000	Cell Signaling	#3294
P-IRE1A	rabbit	1:1000	Novus	NB100-2323
P62 (SQSTM1)	rabbit	1:1000	Cell Signaling	#5114
PDIA1	rabbit	1:1000	Proteintech	11245-1-AP
PDIA4	rabbit	1:1000	Proteintech	14712-1-AP
PDIA6	rabbit	1:1000	Proteintech	18233-1-AP
PERK	rabbit	1:1000	Cell Signaling	#3192
P-PERK	rabbit	1:1000	Cell Signaling	#3179
VCP	mouse	1:5000	Proteintech	10736-1-AP

Secondary antibody	Host	Working dilution	Company	Catalogue number
IRDye® 680RD Goat anti-Mouse IgG Secondary Antibody	goat	1:15000	Li-COR	926-68070
IRDye® 800CW Goat anti-Rabbit IgG Secondary Antibody	donkey	1:15000	Li-COR	926-32211

3.2 Methods

3.2.1 Animal husbandry and ethics statement

Animals were kept under specific-pathogen free (SPF) conditions in individually-ventilated cage systems (IVC) with a 12 h dark/light cycle (6 am – 6 pm) and free access to standard chow diet and water. Cages were enriched with nesting material, gnawing sticks and mouse houses. Colonies were propagated by natural mating and maintained on their original genetic background (see Table 15). All experiments were performed in compliance with the animal welfare guidelines and were approved by the state ethics committee by the government of Upper Bavaria.

3.2.2 Overview of mouse lines

In Table 15, an overview of all mouse lines that were analyzed for this thesis is provided. Details on the identification of the models are described in the results section.

Table 15 Overview of mouse lines

Project	Name of mouse line	Genetic background	Chapter
MIDY	$Ins2^{C109G}$	C3HeB/FeJ	4.1.1
MIDY	$Ins2^{V26D}$	C3HeB/FeJ	4.1.1
MODY1	$Hnf4a^{tm1b}$	C57BL6/NTac	4.3.2
MODY1	$Hnf4a^{R333L}$	C3HeB/FeJ	4.3.3
MODY1	$Hnf4a^{G124A}$	C3HeB/FeJ	4.3.3
MODY1	$Hnf4a^{tm1b/R333L}$	C57/C3H	4.3.4
MODY1	$Hnf4a^{tm1b/G124A}$	C57/C3H	4.3.4
MODY1	Hnf4a-KI	C57BL6/NCrl	4.3.5
PDIA6	$Pdia6^{F175S}$	C3HeB/FeJ	4.2.1

3.2.3 Genotyping

DNA was isolated from ear punches by overnight digestion at 56 °C in 180 µL of Lysis buffer (see Table 3) and 3 µL Proteinase K (Qiagen). The next day, Proteinase K was deactivated for 10 min at 95°C. DNA content was measured in a NanoPhotometer® (Implen) device and subsequently diluted to ≈50 ng/µL. 2 µL of DNA were evaporated in a 96-well plate for 1-2 h at 37 °C before adding 10 µL of Lightscanner Mastermix (see Table 16) to each sample. Genotyping primers are listed in Table 10.

Table 16 Lightscanner mastermix for genotyping

Lightscanner Mastermix	Final concentration	per sample (µl)
H_2O (Ampuwa)		7.55
Phire Reaction Buffer (5x)	1x	2
dNTPs (10 mM) (Serva Electrophoresis)	200 µM	0.2
LC Green Dye (10x)	1x	1
Primer 1 (200 µM)	0.5 µM	0.025
Primer 2 (200 µM)	0.5 µM	0.025
Phire Hot Start II DNA Polymerase		0.2
Final volume		**11**

Reaction mixture was covered with 15 µL mineral oil (Sigma), then the plate was heat sealed. DNA was amplified by PCR with annealing temperatures adjusted for each primer set. The PCR was followed by high-resolution melting analysis using a LightScanner® device (Idaho Technology Inc.) as described in detail elsewhere [137]. Analysis of the melting curve was performed using the accompanying LightScanner® software. This method is specifically suitable to detect single nucleotide polymorphisms (SNPs).

Table 17 PCR protocol

Number of cycles	Step	Temperature	Time
1x	Initial denaturation	98 °C	30 s
40x	Denaturation	98 °C	5 s
	Annealing	to be adjusted	5 s
	Elongation	72 °C	5 s
1x	Final elongation	72 °C	1 min
1x	Improve heteroduplex	98 °C	30-60 s
1x		20 °C	∞

3.2.4 **Overview of experimental procedures**

For each mouse line, an individualized set of *in vivo* and *in vitro* experiments were performed depending on experimental plans and outcomes of the experiments. This is

described in detail in the results section for each model. Here, a general overview of experiments is provided. Detailed descriptions of the procedures can be found below.

3.2.4.1 Organ collection

Figure 8 shows an overview of organ collections and subsequent processing of the tissues for various experiments. Blood was withdrawn from the retrobulbary plexus or the tail for further analyses. The pancreas was withdrawn for tissue analysis, islet isolation or protein isolation. The liver was withdrawn for protein isolation.

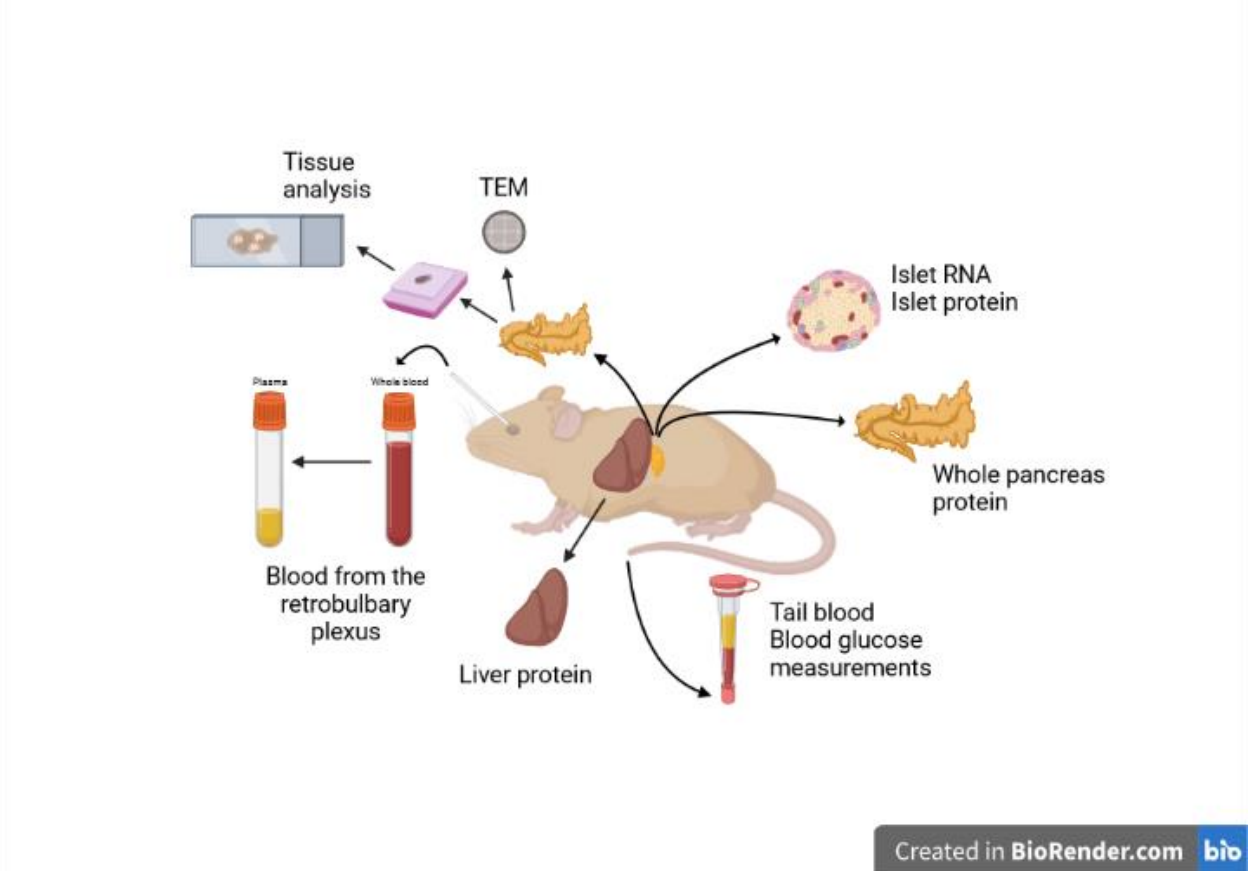

Figure 8 Overview of organ collection

Overview of organ collections and subsequent processing of the tissues for various molecular analyses (created in BioRender.com).

3.2.4.2 Phenotyping (in vivo)

After weaning, the body weight and blood glucose levels of all 9 mouse lines were regularly measured weekly or bi-weekly.

Three of the mouse models ($Ins2^{C109G}$, $Ins2^{V26D}$, Hnf4a-KI) were additionally phenotyped following a standardized protocol for 18 weeks to analyze progression of the diabetic phenotype. Measurements included regular monitoring of body weight, blood glucose levels and plasma insulin. Additionally, mice were challenged with glucose or insulin to determine their metabolic response at two different ages. Between each experiment, mice were given 2 weeks to recover from procedures. An overview is provided in Figure 9. Experiments marked in green are optional experiments. Experiments marked in grey and blue were performed for all animals. For MIDY mouse models, experiments started at 4 weeks of age, since MIDY manifests very early in life in humans. Typically, MODY1 manifests only in the early adult age in humans, therefore experiments with MODY1 models were only started at 6 weeks of age.

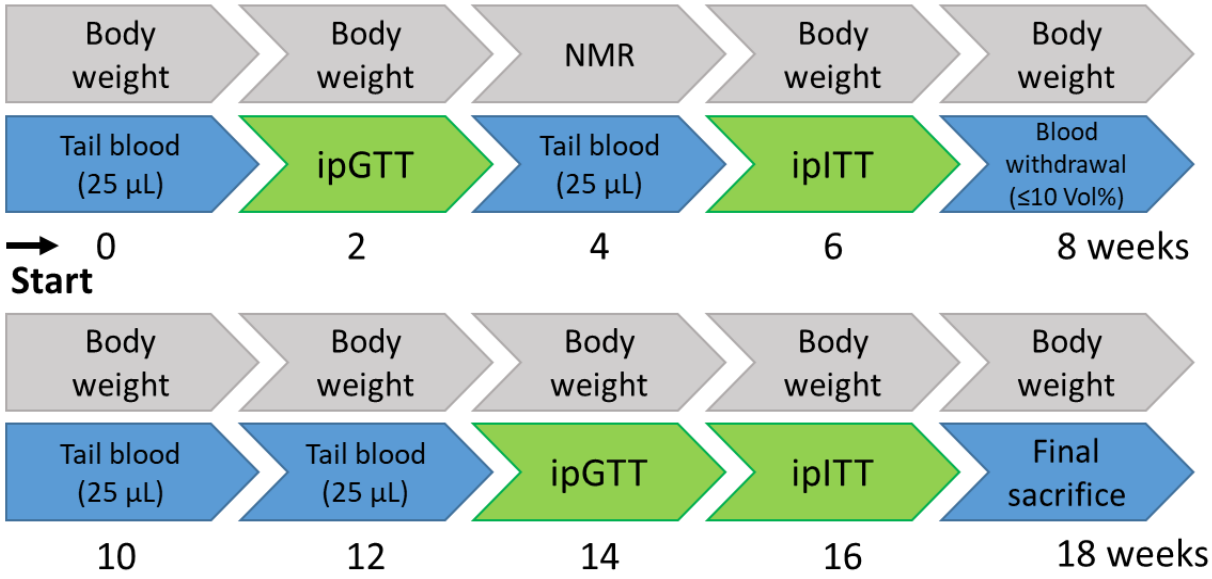

Figure 9 Overview of the in vivo phenotyping pipeline

Mice were phenotyped following a standardized pipeline of experiments. For $Ins2^{C109G}$ and $Ins2^{V26D}$, mice were phenotyped starting from 4 weeks of age. Hnf4a-KI mice were phenotyped starting from 6 weeks of age. Grey: Bi-weekly measurements of body weight and blood glucose Blue: Experiments performed for all animals; Green: Optional experiments.

Hnf4a^{tm1b} mice were phenotyped following standard procedures from the German Mouse Clinic (GMC) of the hypothesis-driven pipeline G “Glucose Metabolism”: https://www.mouseclinic.de/research/gmc-pipelines/hypothesis-driven-pipelines/index.html.

3.2.4.3 Gene therapy of Hnf4a-KI (in vivo)

Surgery for intraductal delivery of AAV gene-therapy vectors was performed on animals aged 4 weeks. Mice were left to recover for another 4 weeks, before entering the same experimental pipeline as described in Figure 9.

3.2.5 ***In vivo* physiological methods and metabolic studies**

3.2.5.1 Monitoring of body weight, blood glucose levels and body composition

Body weight was measured weekly using a standard balance (Sartorius). Blood glucose measurements were performed bi-weekly at 2 pm in *ad libitum* fed animals from tail blood using Contour®Next One and matching sensors (Ascensia Diabetes Care). Analysis of body composition was carried out using non-invasive nuclear magnetic resonance (NMR) (Bruker Minispec) to determine fat mass and lean mass.

3.2.5.2 Isoflurane anesthesia

Isoflurane anesthesia was used for blood sampling from the retrobulbary plexus. Anesthesia induction was performed in an induction chamber with 5% isoflurane in air (flow rate: 1-1.5 L per minute) using an appropriate device. Mice were removed from the chamber to collect plasma. Anesthesia lasts for approximately 1-2 min, which is sufficient for the procedure.

3.2.5.3 Plasma collection from the retrobulbary plexus

For *in vivo*-collection of plasma, a maximum of 10% of total blood volume (ca. 200-350 µL) was collected into EDTA- or Heparin-coated tubes (Sarstedt) from the retrobulbary plexus under deep isoflurane anesthesia using capillaries. Samples were centrifuged for 10 min at 10°C at 5000×g to obtain plasma. Samples were immediately snap frozen in liquid nitrogen.

3.2.5.4 Plasma collection from the tail

For *in vivo*-collection of plasma, a maximum of 50 µL blood was withdrawn from the tail. A small cut was made at the end of the tail, then the tail was massaged carefully to extract blood from the tip directly into EDTA- or Heparin-coated capillary tubes (Sarstedt). Samples were centrifuged for 2 min at 10°C and 8000 rpm (Heraeus Fresco) to obtain plasma and were immediately snap frozen.

3.2.5.5 Metabolic studies: ipGTT and ipITT

Mice were fasted for 6 h (7 am to 1 pm) prior to *ip* injection of 2 g/kg glucose (20%, Braun) for an intraperitoneal glucose tolerance test (ipGTT) or 0.75 U/kg insulin (Huminsulin, Eli Lilly) for an intraperitoneal insulin tolerance test (ipITT). Blood glucose was measured from tail blood at time point 0 using Contour®Next One and matching sensors (Ascensia Diabetes Care). Afterwards, blood glucose was measured at several time points after injection of glucose or insulin:

- ipGTT: 5, 15, 30, 60, 90 and 120 min; additionally: plasma collection from tail blood into EDTA-coated tubes (Sarstedt) at time points 0, 15 and 30 and subsequent plasma isolation.
- ipITT: 15, 30, 60 and 90 min

3.2.6 **Retrograde pancreatic intraductal AAV injection to Hnf4a-KI mice**

For the gene therapy of Hnf4a-KI mice, recombinant AAV8 (rAAV8) particles containing the *Hnf4a* gene under a β-cell specific promoter (described in the patent application EP21382080, schematically shown in Figure 10) were injected directly into the pancreas via a microsurgical procedure, namely retrograde intraductal injection. Intraductal injections were performed as described by Loiler et al. in 2005 [134] with some modifications. This method is commonly used by our collaborators of the laboratory of Fatima Bosch at the Autonomous University (UAB) [126, 135]. After intense training at the Barcelona facility, we optimized the protocol to adapt to local circumstances and recent discoveries. Exact procedures as performed are described in the results section (4.3.6.1).

Table 18 Buffer for AAV vectors (PBS+pluronics)

Buffer for AAV vectors (PBS)	Final concentration [mM]
KCl	2.68
KH_2PO_4	1.46
NaCl	137.89
Na_2HPO_4	8
Pluronics F-68 10% (Gibco)	0.001%
	Dissolve in dH_2O, adjust pH to 7.4, sterile filtrate and aliquot

Animals were separated into 2 groups: control group and treatment group. The control group was injected with 200 µL of PBS solution (Table 18). For the treatment group, rAAV8 vectors (5×10^{11} viral genomes (vg)) were diluted in 200 µL of the same buffer. As determined by our collaborators at UAB, one dose containing 5×10^{11} vg is sufficient to transduce most of the β-cells.

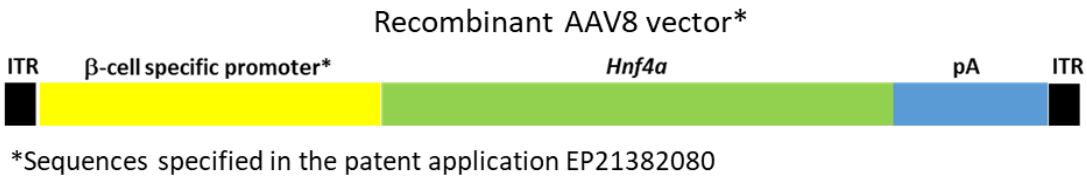

Figure 10 Schematic of the recombinant AAV8 vector

Structure of the recombinant AAV8 vector used for gene therapy treatment. The vector includes ITRs (inverted terminal repeats), a β-cell specific promoter, the *Hnf4a* gene and a polyadenylation sequence (pA).

3.2.7 **Organ collection**

Before the final sacrifice, mice under deep isoflurane anesthesia were bled from the retrobulbary plexus as described in section 2.2.5.3. Afterwards, mice were sacrificed by cervical dislocation. Blood samples (up to 1 mL per mice upon final sacrifice) were centrifuged for 10 min at 10 °C and 5000×g to obtain plasma, which were aliquoted and immediately snap-frozen. Finally, the desired organs, such as the liver and pancreas, were removed. Depending on the intended use, tissue was processed for fixation or snap-frozen immediately for later RNA or protein extraction (see Figure 8 for an overview).

3.2.8 Plasma analysis

To analyze hormone content in the plasma, ELISA kits were utilized. Insulin, proinsulin and glucagon were measured using mouse ELISA kits from Mercodia, C-peptide using BioCat mouse ELISA. All procedures followed the manufacturer's instructions. All samples were measured as duplicates. A Varioskan LUX (Thermo Fisher) reader was used to measure the absorption. The duplicates were averaged, then the standard deviation and %CV were calculated to assure measurement quality. Subsequently, a standard curve was calculated from the calibrators using a 4P logistic curve or cubic spline regression. Based on the standard curve, hormone concentrations were calculated for each sample.

3.2.9 Tissue processing for paraffin embedding (pancreas)

After excision, pancreata were fixed for 24 h in 4% PFA (w/v, phosphate-buffered, pH 7; see Table 4). Tissues were than processed for paraffin embedding using a Sakura Tek VIP Tissue Processor following the manufacturer's protocol. After processing, pancreata were embedded in paraffin blocks for subsequent sectioning using a specialized device (Thermo Scientific HistoStar).

3.2.10 Immunofluorescent staining of paraffin-embedded pancreas sections

Pancreas sections were cut at 4 µm using a microtome (Thermo Scientific MICROM HM340E) and pulled onto SuperFrost® Plus slides (Thermo Scientific). Pre-staining, sections were deparaffinized in Xylene and rehydrated in a descending alcohol series (2x 100% EtOH → 2x 96% → 80% → 70% → 50%). For recipes of buffers used in IF staining see Table 4. Heat-induced antigen retrieval was performed in a pressure cooker for 3 min at full pressure in Tris-EDTA pH 9. After cooling in washing buffer, blocking was performed in IF buffer for 2 h. Slides were incubated with primary antibodies in blocking buffer overnight at 4°C, washed 3x 5 min in washing buffer, followed by incubation at RT for 45 min with appropriate fluorophore-conjugated secondary antibodies and DAPI. Slides were then washed 3-4x for 10 min in washing buffer before mounting with Vectashield® Vibrance medium (Vector Laboratories). Finally, slides were left to dry for at least 12 h before imaging. Primary and secondary antibodies as well as their working dilutions are provided in Table 13. Confocal images were obtained using a Zeiss LSM880

microscope at 20x or 63x magnification. Images were further processed using ZEN 2.6 blue (Zeiss) and Fiji software.

3.2.11 Morphometric analysis of the pancreas

To determine the α- and β-cell mass, fresh pancreata were dissected, briefly dabbed on paper towel and weighed. Processing of samples, staining and scanning procedures as well as image analysis were performed as previously described [138]. In brief, paraffinized pancreata were cross-sectioned into 4-6 parallel, equidistant slices per sample, vertically embedded in paraffin and cut at 4 µm. The staining was carried out with an automated tissue stainer (Ventana) or as described in 3.2.10. Sections were digitally scanned using an AxioScan.Z1 digital slide scanner (Zeiss) equipped with a 20x magnification objective. Automated digital image analysis was performed by Annette Feuchtinger (Helmholtz Zentrum München) using the image analysis software Definiens Developer XD2 (Definiens AG) to determine several morphometric parameters, e.g. islet size, insulin- or glucagon-positive area or number of cells. Finally, the α- and β-cell mass [mg] was calculated by multiplying the detected relative glucagon-positive and insulin-positive cell area by total pancreatic weight, respectively. Antibodies are provided in Table 13.

3.2.12 Transmission electron microscopy

Five to eight pancreas samples (≈1 mm^3) were excised from random locations in the pancreas and fixed in 2.5% electron microscopy-grade glutaraldehyde in 0.1 M sodium cacodylate buffer pH 7.4 (Science Services). The samples were then post-fixed in 2% aqueous osmium tetraoxide, dehydrated in gradual ethanol (30–100%) and propylene oxide, then embedded in Epon (Merck) and cured for 24 hours at 60°C. All following procedures were performed by Thomas Kurth (TU Dresden). Semithin sections were cut at 0.5-1 µm and stained with toluidine blue to be examined microscopically for the presence of islet section profiles. Corresponding ultrathin (70 nm) sections of islets were mounted on slot copper grids and contrasted with uranyl acetate and lead citrate. Sections were examined with a Jeol JEM 1400 Plus transmission electron microscope equipped with a Jeol Ruby-CCD Camera.

3.2.13 Islet isolation, cultivation and lysis

To isolate pancreatic islets, mice were first sacrificed by cervical dislocation before the abdominal cavity was opened. Mice were placed under a stereomicroscope with the anterior end facing towards the experimenter. The common bile duct was exposed by dislocation of the gut and the liver. A micro bulldog clamp (Roboz) was placed on the Ampulla of Vater, the site where the common bile duct enters the duodenum. For buffers that were used for islet isolation please confer to Table 5. Then, the common bile duct was entered with a 30G1/2 needle (Braun) and 3-4 mL of collagenase solution were perfused into the pancreas. After perfusion, the pancreas was removed from the cadaver and immediately placed on ice in a 15 mL reaction tube containing 3.5 mL collagenase solution. Reaction tubes with perfused pancreata were kept for a maximum of 60 min on ice before proceeding to the next step, thereby limiting the number of animals per experimenter to approximately 6-8. Once all samples were collected, digestion of the pancreata was carried out in a water bath at 37°C for 15 min with a gentle shaking step at 7.5 min. All further steps were performed under a sterile working bench. First, 10 mL of ice-cold G-solution were added to the tubes to stop the reaction, then samples were centrifuged at 290×g for 2 min at RT. The supernatant, which contains mostly exocrine tissue and fat, was carefully decanted. Using 10 mL of G-solution, the leftover pancreatic digest was dissolved by repeated vigorous pipetting. The solution was filtered through a metal mesh (pore size ca. 1 mm) into a 50 mL reaction tube to remove larger undigested pieces. Another 10 mL of G-solution, used to rinse the 15 mL tube, were also filtered through the metal mesh. Finally, the metal mesh was rinsed with another 20 mL of G-solution to avoid loss of islets. The complete filtrate was centrifuged at 290×g for 2 min at RT. After decanting the supernatant, containing mostly acinar cells, the pellet was resuspended in 5.5 ml of Optiprep-RPMI solution. This resuspension was slowly pipetted along the wall into a new 15 mL tube containing 2.5 mL Optiprep-RPMI, generating a gradient. This gradient was then overlaid with 6 mL of G-solution to obtain a third layer. Samples were allowed to incubate for further 10 min on the bench to improve gradient formation and then centrifuged at 290×g for 15 min at RT with adjusted slow acceleration and no break to avoid mixing of the gradients. Islets can now be found between the second and the third layer of the gradient. They were carefully collected with a serological

pipet and subsequently filtered through a 70 µm cell strainer to remove leftover acinar tissue. Islets were captured from the cell strainer by turning the strainer and rinsing with G-solution into an untreated suspension culture dish. Then, islets were hand-picked under a stereomicroscope and placed in a new suspension culture dish containing 12 mL islet culture medium with a maximum of 60-80 islets per dish. Islets were left to rest and recover overnight in an incubator at 37°C with 5% CO_2 infusion and humidified air before subsequent islet lysis, RNA isolation or protein isolation.

To measure insulin content, 15 similar-sized islets were handpicked and immediately lysed in 500 µL of ice-cold 0.81M acid-ethanol (Table 5). Lysates were immediately frozen at -20 °C and kept for maximum ½ year until analysis.

3.2.14 RNA isolation from islets

After overnight resting, islets were hand-picked for RNA or protein isolation. RNA was isolated using the RNeasy Micro kit (Qiagen) following the manufacturer's instructions. RNA concentration was measured using a NanoPhotometer® (Implen) device before storing the RNA at -80 °C until use.

3.2.15 Gene expression profiling by qRT-PCR

3.2.15.1 Synthesis of cDNA

For cDNA synthesis, equal amounts of RNA were reverse-transcribed using SuperScriptIV (Thermo Fisher). In brief, primers were annealed to template RNA by heating to 65°C for 5 min and chilling on ice for 5 min. Then the real-time reaction mix was added, mixed gently and briefly centrifuged before incubating at 50-55°C for 10 min and subsequent inactivation of the reaction at 80°C for 10 min in a thermal cycler. Reagents are provided in Table 19. Nuclease-free water was added to obtain a final concentration of 2.5 ng/µL of cDNA. The cDNA was stored in aliquots at -20 °C until use.

Table 19 cDNA synthesis

Primer annealing	Volume [µL]
50 µM random primers (NEB)	1
10 mM dNTPs	1
RNA template	X ng (maximum up to 11 µL)
RNAse free H_2O	To 13 µL
RT Reaction Mix	**Volume [µL]**
5x SSIV Buffer	4
100 mM DTT	1
Superscript IV Reverse Transcriptase	1
RNaseOUT	1
Prepare master mix, add 7 µL to annealed RNA	**To total of 20 µL**

3.2.15.2 Quantitative real-time PCR (qRT-PCR)

Quantitative real-time PCR (qRT-PCR) is a method that can be used to perform quantification of relative gene expression from cDNA samples using a fluorescent dye such as SYBR Green. To obtain sequence information for desired genes, the ENSEMBL genome browser (https://www.ensembl.org/index.html) was used. Primers were designed manually for exon-exon junctions of each gene to ensure amplification of only mRNA. Further, primers were designed aiming for final transcription products with a length within a range of 70-300 bp to get optimal results. Primer-BLAST (https://www.ncbi.nlm.nih.gov/tools/primer-blast/) was used as tool to design the primers according to before-mentioned criteria. It was further used to exclude unspecific binding to other areas of the genome. Primers were ordered from metabion international (Planegg, Germany) and dissolved upon arrival to obtain a final stock concentration of 100 µM. Primer pairs were first tested on WT cDNA to ensure correct product size. The melting curve was analyzed to further ensure specificity of the primer and amplification of only one product.

The qRT-PCR was performed using QuantiFast SYBR Green PCR Kit (Qiagen) with 0.5 ng (islets) or 2 ng (liver) of cDNA per well in 384-well plates. Primers pairs were pre-diluted in RNAse-free H_2O to obtain a 3 µM primer master mix that were first pipetted into

the wells. Three to four technical replicates were measured per sample to ensure quality of the measurement. Matrix Electronic Pipettes (Thermo Fisher) or E1-ClipTip Electronic Multichannel Equalizer Pipettes (Thermo Fisher) were used for efficient and precise pipetting. Sequences of the primer pairs are provided in Table 12. The QuantiFast master mix (see Table 20) containing all other components was then added on ice.

Table 20 QuantiFast master mix

Component	Final concentration	Volume [µL]
Primer master mix (fwd. +rev.) (3 µM)	0.3 µM	2
cDNA	0.5/2 ng/well	Variable (x)
QuantiFast SYBR Green Master Mix (2x)	1x	10
RNAse-free H_2O		8-x
Total Volume		**20 µL**

After pipetting, the plate was sealed to avoid evaporation and centrifuged before being placed into a LightCycler® 480 device (Roche). The experiments were ran using the following cycling conditions:

Table 21 LightCycler 480 cycling conditions

Number of cycles	Temperature [°C]	Time
1x	95	10 min
35x	94	15 s
	60	60 s
1x	55-95	Melting curve

When the reaction was finished, data was extracted and Crossing point (C_p) values were calculated from the accompanying software by the second derivative maximum method. Averages and standard deviations were calculated for the technical replicates to ensure data quality. Melting temperatures (T_m) were checked to assure amplification of only one fragment.

For relative quantification, normalization to suitable housekeeping genes is key to the experiment. Since mouse strains, genotypes or experimental set ups are different, the optimal housekeeping genes must be sought individually. Therefore, for each new set-up, a set of housekeeping genes (see Table 11) was analyzed. By using the BestKeeper Excel tool [139], the most stable housekeepers were determined. Gene expression for

Ins2^{C109G} was normalized to *Rpl13a* and *Ubc*, for Ins2^{V26D} to *Rpl13a* and *Tbp*, for Hnf4a-KI to *Atp5b* and *Rpl13a*, and for Pdia6^{F175S} to *Rpl13a* and *Ubc*.

Finally, data were analyzed as previously described using the Livak ΔΔCt method [140], normalized to housekeeping genes and shown as relative expression compared to the control group.

3.2.16 **Protein extraction from islets**

For protein extraction, hand-picked islets were collected in a 1.5 mL tube and centrifuged for 1 min at 12,000 rpm. If less than 150 islets per animal were collected, samples of two mice of the same genotype were pooled. Then, the medium was carefully removed and the pellet washed in 1 mL of PBS without Ca_2^+ and Mg_2^+ (Lonza) and centrifuged again for 1 min at 12,000 rpm. The supernatant was discarded and islets were resuspended in 100 µL of ice-cold RIPA Buffer (Thermo Fisher) supplemented with protease- and phosphatase-inhibitors (Table 6). Samples were shaken at 1,400 rpm at 4°C (Thermo Mixer C, Eppendorf) and sonicated 4×30 s to extract protein with in-between cooling steps of 30 s on ice. Finally, samples were centrifuged at 13,000 rpm and 4°C for 10 min to dispose insoluble components. The supernatant was transferred to a new 1.5 mL reaction tube and stored at -80°C until use.

3.2.17 **Protein extraction from whole pancreas and liver**

For protein extraction from liver, tissue was first dissected into small pieces. For protein extraction from the pancreas, the whole tissue was utilized. To extract tissue protein, a Precellys Evolution instrument (Bertin Instruments) equipped with a Cryolys Evolution cooling unit (Bertin Instruments) was used. For each sample, one tube from the CK14 2 mL Lysing Kit (Bertin Instruments) was prepared by adding 650 µL of ice-cold RIPA Buffer (Thermo Fisher) supplemented with protease- and phosphatase-inhibitors (Table 6) to the tube and subsequent pre-cooling on ice. Samples were brought on dry ice and only added to the pre-cooled buffer shortly before isolation. Tubes were then placed in the Precellys centrifuge and lysed together (up to 24 samples) using the following settings (Table 22):

Table 22 Precellys setting

Number of cycles	Temperature [°C]	Time	Speed [rpm]
3x	4	20 s	6000
	4	30 s	pause

After isolation, samples were immediately kept on ice. To get rid of cell debris, samples were centrifuged at full speed (13000 rpm) at 4°C for 30 min. To enhance storage conditions, small tubes were pre-cooled on ice. After centrifugation, 3 layers are visible: debris, protein solution, fat. Carefully, only the protein solution was pipetted and stored in small aliquots at -20°C until use.

3.2.18 **Western blot analysis**

Islet protein concentrations were determined using the Micro BCA™ Protein Assay Kit (Thermo Fisher) (dilution: 1:10). Liver and whole pancreas protein concentrations were determined using the Pierce BCA Assay Kit (Thermo Fisher) (dilution: 1:100 or 1:200) according to manufacturer's instructions. For western blot analyses, samples were prepared as reduced samples using BOLT reagents as suggested by the manufacturer (Life technologies) (Table 23). For islets, due to low protein amount, 2 µg of protein per sample were prepared, for liver and whole pancreas 40 µg. Once mixed together, samples were denatured for 10 min at 70°C.

Table 23 Preparation of reduced samples for western blot

Components	Reduced Sample
Sample	*x* µL
BOLT LDS Sample Buffer (4X)	2.5 µL
BOLT Reducing Agent (10X)	1 µL
Deionized Water	To 6.5 µL
Total Volume	**10 µL**

After denaturation, samples were loaded onto BOLT 4-12% gradient or 12% Bis-Tris Plus gels (Life technologies). The Chameleon Duo Ladder (LI-COR) was used to visualize protein separation during electrophoresis and to estimate the molecular weight of proteins. For buffers, see Table 6. Gels were placed into the chamber (Mini Gel Tank, Life technologies), loaded and the chamber was filled with SDS MES running buffer (Life technologies). 1 mL of BOLT Antioxidant (Life technologies) was added to 400 mL of 1x

SDS Running Buffer (Life technologies) to keep reduced conditions. After gel electrophoresis (35 min at 200 V constant), proteins were transferred to nitrocellulose membranes (0.45 µm or 0.20 µm pore size, Life technologies) in the Mini Blot Module (Life technologies) for 60 min at 10 V constant. After transfer, Ponceau solution (Sigma) was applied to check for proper protein transfer to the membrane, then membranes were washed in TBS-T until the red color disappeared. Blocking was performed in Intercept® (TBS) Blocking Buffer (LI-COR) shaking for 2 h at RT. Subsequently, primary antibodies were incubated at 4°C overnight (shaking). After washing in TBS-T, fluorophore-conjugated secondary antibodies were incubated at RT for 45 min in blocking buffer (shaking). Membranes were washed thoroughly 3-4x for 10 min in TBS-T to reduce fluorophore-conjugates before infrared detection using an Odyssey Infrared Imaging System (LI-COR) for membrane scanning. Subsequent densitometric quantification was performed using the accompanying software Image Studio Lite Ver5.2 (LI-COR). Data was normalized to α-tubulin expression and is shown as relative fluorescence intensity (RFI). Antibodies and working dilutions are provided in Table 14.

3.2.19 Statistics and reproducibility

All statistical analyses were performed using GraphPad Prism 9. To compare two groups, a two-tailed homoscedastic Student's t-test or heteroscedastic with Welch's correction was performed. To analyze data generated from repeated measurements, a 2-way ANOVA (analysis of variance) or mixed-effect analysis with Bonferroni correction for multiple testing was performed. Values of $p \leq 0.05$ were considered significant and marked with one *, values $p \leq 0.01$ were marked with two **, values $p \leq 0.001$ were marked with three *** and values where $p \leq 0.0001$ were marked with four ****. The letter 'n' describes the number of samples. A Shapiro-Wilk test was performed to check for normal distribution in case $n>10$. Bar graphs were plotted displaying individual values, the bars themselves equal mean values. Error bars equal either standard error of the mean (SEM) where $n>10$, or standard deviation (SD) if $n \leq 10$.

4. Results

4.1 Neonatal diabetes mellitus caused by mutations in insulin: Characterization of two novel mouse models Ins2^{C109G} and Ins2^{V26D}

Two novel mouse models for neonatal diabetes mellitus caused by insulin mutations, often referred to as MIDY, were characterized *in vivo* following the standardized procedure as described in 3.2.4.2. Additional molecular analyses for islet morphology, β-cell identity, ER-stress, and autophagy were performed to determine the underlying mechanisms of how different *Ins2* mutations lead to severe diabetes and how different models with different mutations differ from one other. In the following chapter, only a selection of results is presented in order to highlight important findings. Additional data from younger animals and data from females, who exhibit a milder phenotype, are provided in the appendix.

4.1.1 Identification of two novel *Ins2* mutant mouse lines: Ins2^{C109G} and Ins2^{V26D}

The mouse models Ins2^{C109G} and Ins2^{V26D} were identified for the first time on the basis of phenotypic variation (hyperglycemia) in the Munich ENU mutagenesis screen [141, 142]. The chromosomal positions of the causative mutations were determined as previously described [142] and *Ins2* was suggested as the candidate gene. After 10 generations of outcrossing to C3HeB/FeJ wild-type (WT) mice to reduce off-target mutations, point mutations in the *Ins2* gene were confirmed by sequence analysis (experiments performed by Bernhard Aigner; LMU) (Figure 11A). In Ins2^{C109G}, the cysteine at position 109 is exchanged for a glycine (C109G). In Ins2^{V26D}, the valine at position 26 is exchanged with aspartic acid (V26D). The positions of the new mutations in the preproinsulin molecule are shown in Figure 11B in comparison to already known *Ins2* mutations in other mouse models. Only heterozygous mice, denoted here as Ins2^{C109G} and Ins2^{V26D}, and their corresponding WT littermates were analyzed. Homozygous mice were viable, but showed severe hyperglycemia at weaning age, which is why they were not included in these studies for ethical reasons.

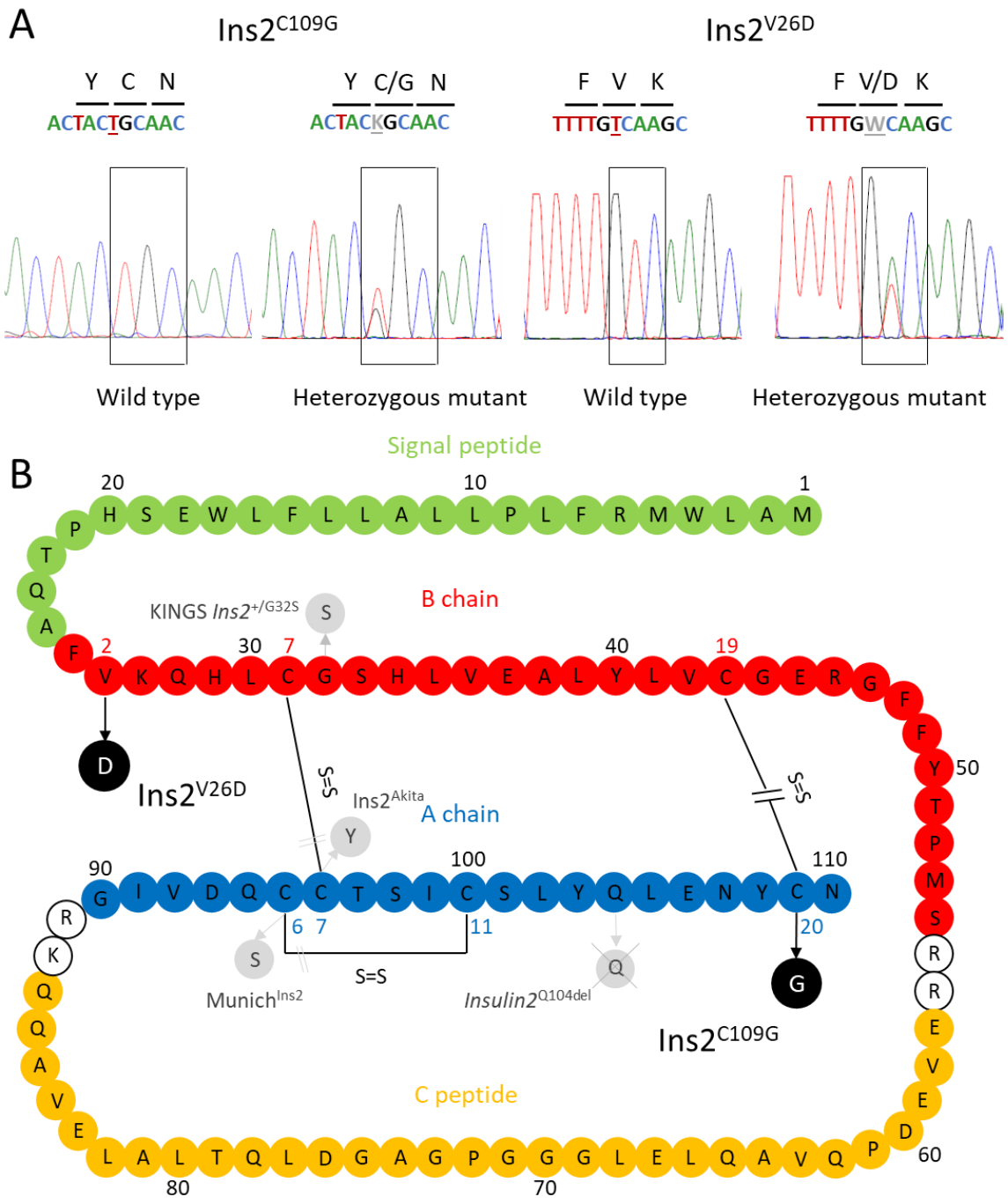

Figure 11 Identification of novel Ins2 mutations

(A) Electropherograms of amino acid substitutions in Ins2^{C109G} and Ins2^{V26D}.

(B) Amino acid (AA) sequence of the preproinsulin molecule is numbered in black letters (1-110).. **Green:** Signal peptide (AA1-24); **Red:** B-chain (AA25-54); **Yellow**: C-peptide (AA57-87); **Blue**: A-chain (AA90-110). AA of the A- and B-chain are numbered in red and blue, respectively. Included are disulfide bridges (S=S) (A7-B7; A20-B19; B6-B11). Mutations of the novel mouse models (Ins2^{V26D}, Ins2^{C109G}) are shown in black circles. Previously existing mouse models are shown in grey circles (KINGS Ins2$^{+/G32S}$, Munich^{Ins2}, Ins2^{Akita}, *Insulin2*^{Q104del}). The sequence was obtained from https://www.uniprot.org/uniprot/P01326.

4.1.2 Severe, early-onset diabetes and sexual dimorphism

In order to determine the onset and progression of the diabetic phenotype, 4-week-old mice were subjected to the standardized procedure for phenotyping as described in 3.2.4.2. In contrast to females, mutant male mice of both mouse lines from an age of 15 weeks ($Ins2^{C109G}$, Figure 12A-A') or 16 weeks ($Ins2^{V26D}$, Figure 12D-D') showed a significantly reduced body weight compared to controls. Progressive hyperglycemia was evident in males from an age of 6 weeks ($Ins2^{C109G}$, Figure 12B) or 4 weeks ($Ins2^{V26D}$, Figure 12E), while in females of both models from an age of 4 weeks a significantly and consistently increased blood glucose level was observed (Figure 12B' and E'). Interestingly, the blood glucose levels in $Ins2^{V26D}$ males rose rapidly above 25 mM (at 8 weeks of age) and continued to rise, while in $Ins2^{C109G}$ males the blood glucose levels never reached 25 mM and decreased with age (beginning in 20-week-old mice). Plasma insulin in 8- or 16-week-old random-fed animals was significantly reduced in males at both time points, but in females only at the age of 8 weeks (Figure 12C-C', F-F'). Remarkably, in 16-week-old male animals no plasma insulin was detectable in 4 animals ($Ins2^{C109G}$) or in 11 animals ($Ins2^{V26D}$).

In summary, we observed severe early-onset diabetes in male animals and mild hyperglycemia in females, which is a pronounced sexual dimorphism. Hyperglycemia is accompanied by hypoinsulinemia in both females and males.

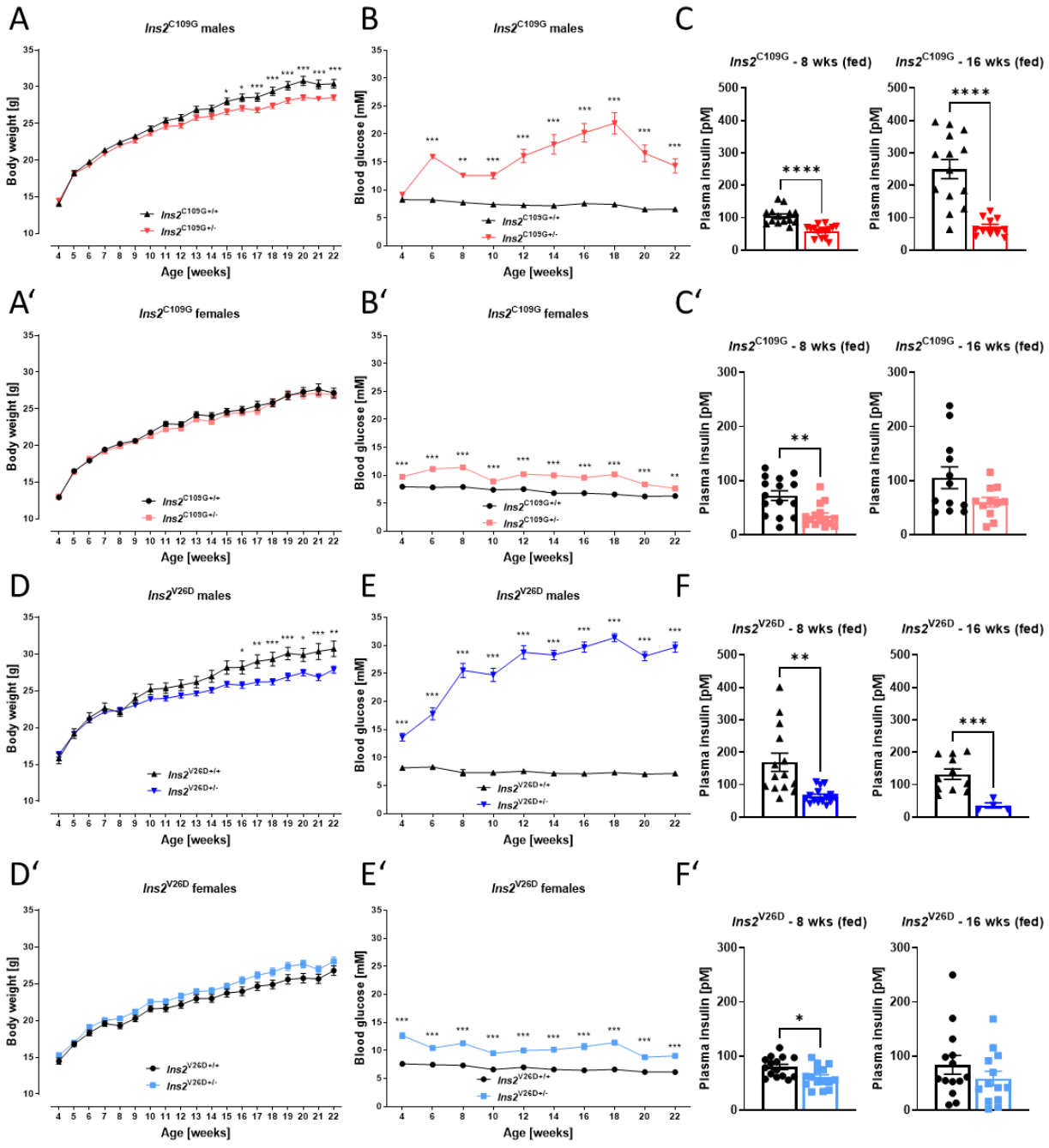

Figure 12 Severe early-onset diabetes and sexual dimorphism in Ins2^{C109G} and Ins2^{V26D}

(A-A') Body weight [g] from *ad libitum* fed Ins2^{C109G} and WT; n=15. **(B-B')** Blood glucose [mM] from *ad libitum* fed Ins2^{C109G} and WT; n=15. **(C-C')** Plasma insulin [pM] from *ad libitum* fed Ins2^{C109G} and WT aged 8 weeks and 16 weeks; n=11-15 (4 out of 15 male het samples at 16 weeks were below detection limit). **(D-D')** Body weight [g] from *ad libitum* fed Ins2^{V26D} and WT; n=14-15. **(E-E')** Blood glucose [mM] from *ad libitum* fed Ins2^{V26D} and WT; n=14-15. **(F-F')** Plasma insulin [pM] from *ad libitum* fed Ins2^{V26D} and WT aged 8 weeks and 16 weeks; n=4-15 (11 out of 15 male het samples at 16 weeks were below detection limit).

4.1.3 Effects of the mutations on islet morphology and β-cell mass

To analyze the effects of the mutations on islet morphology, we performed immunohistochemistry using insulin and glucagon on pancreatic sections from male and female animals at the age of 8 weeks. Throughout the islets of mutant animals of both models, we observed centrally dispersed α-cells after co-staining for glucagon (GCG, α-cells) and insulin (INS, β-cells) (Figure 13A), which deviates from the normal distribution in mice. The insulin content of islets was significantly reduced in all mutant animals (Figure 13B-B'). Furthermore, morphometric analysis in male Ins2^{C109G} showed decreased β-cell mass, while α-cell mass remained unaffected (Figure 13C). We also found that the mean islet size was reduced in Ins2^{C109G} (Figure 13D). Interestingly, we did not observe any of these changes in Ins2^{V26D} mice (Figure 13C'-D').

Since we observed very early onset of severe hyperglycemia, islets from animals aged P7, P15, and 4 weeks (1 month) were also co-stained with insulin and glucagon to observe morphologic changes throughout time. At all these ages, we did not observe any obvious differences in islet composition and α- and β-cell localization (Supplementary Figure 2A, C), hinting that disturbed islet morphology is a secondary effect.

Taken together, we observed a disturbed islet morphology and reduced insulin content in both models at 8 weeks. However, loss of β-cell mass and reduced mean islet size were only observed in Ins2^{C109G} animals.

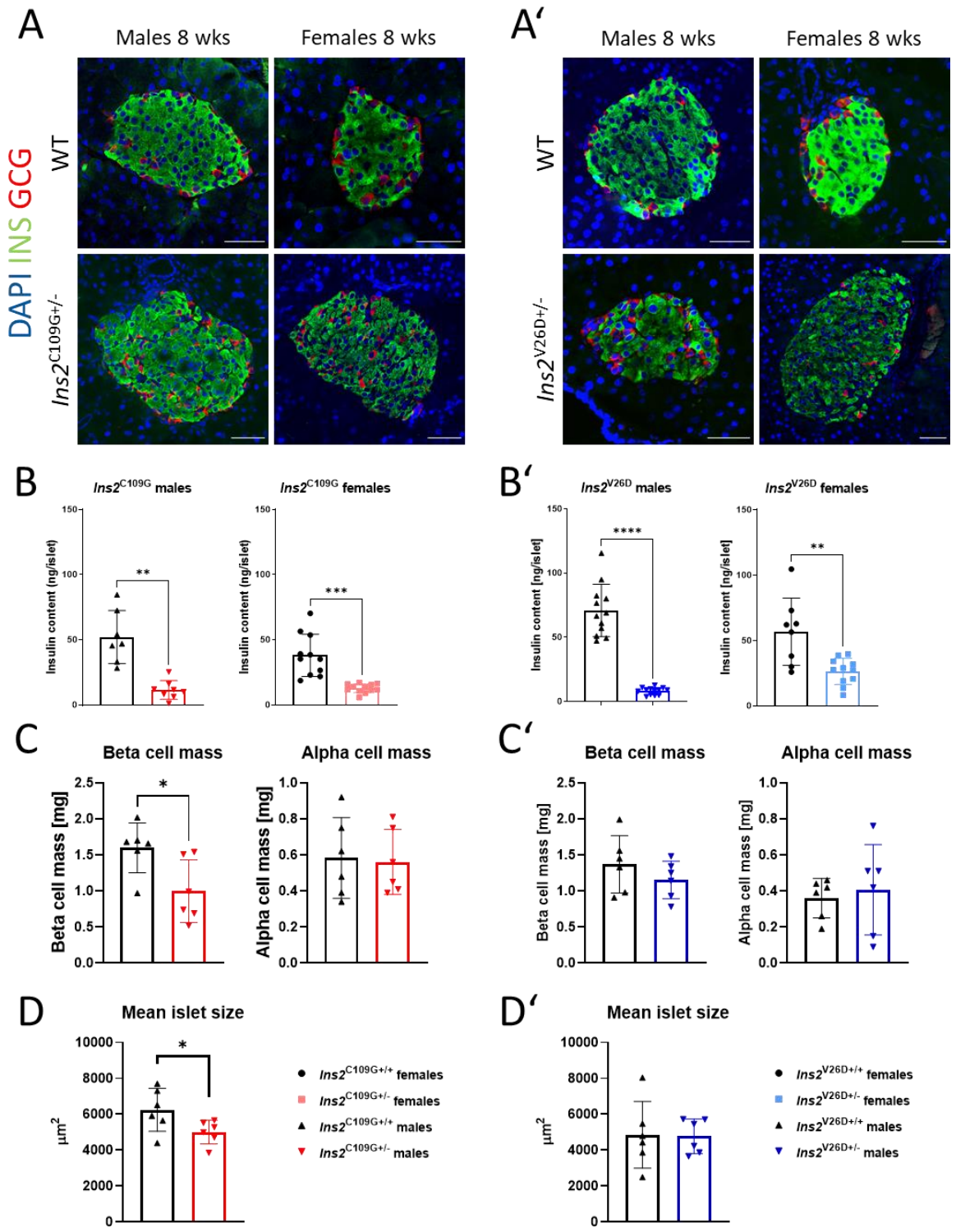

Figure 13 Islet morphology, insulin content, β- and α-cell mass and mean islet size in Ins2^{C109G} and Ins2^{V26D}

(A-A') Representative images of islets of Langerhans from WT, Ins2^{C109G} and Ins2^{V26D} animals. DAPI: blue, insulin: green, glucagon: red. Scale bars equal 50 µm. **(B-B')** Insulin content [ng/islet] of isolated islets from 8-week old animals, n=7-13. **(C-C')** Beta- and alpha cell mass in [mg]; **(D-D')** mean islet size in [µm^2] from WT, *Ins2*^{C109G} and *Ins2*^{V26D} males at the age of 8 weeks; n=6.

4.1.1 Reduced proinsulin staining and dysregulated secretion of hormones to the blood stream in 8-week-old mutants

Processing from proinsulin to insulin is tightly regulated in β-cells. It has been shown that an aberrant cellular localization of insulin and proinsulin can indicate deficits in the processing from proinsulin to the mature hormone [143]. To assess whether intracellular displacement occurs in our *Ins2* mutations, we performed immunohistochemistry using insulin (INS) and proinsulin (PROINS) in males. Normally, insulin and proinsulin do not co-localize [143], which we also did not observe in either of the two models, suggesting normal processing. However, we observed greatly reduced proinsulin staining in mutants of both models (Figure 14A-A').

Since we observed significantly reduced insulin content in isolated islets, reduced plasma insulin in randomly fed animals, and reduced proinsulin staining, we aimed to assess the effects of the mutations also on the secretion of insulin and proinsulin in fasted animals at 8 weeks of age. In addition, the ratio of insulin to proinsulin in plasma was assessed to confirm that no processing deficits occurred. In mutant males, fasting hyperglycemia was accompanied by hypoinsulinemia and hypoproinsulinemia, whilst the INS/PROINS ratio was comparable between the groups (Figure 14B-B'). In addition, the plasma concentrations of glucagon and C-peptide were checked and found comparable between mutant and wild-type males of both lines (Figure 14C-C').

In females of both lines, we observed only mild fasting hyperglycemia. However, hyperglycemia was not accompanied by significant changes in plasma insulin and proinsulin, including the INS/PROINS ratio (Supplementary Figure 1A-B). We also did not detect differences in plasma glucagon and C-peptide (Supplementary Figure 1B-B'). Yet, we found reduced insulin content in isolated islets (Figure 13B-B').

To analyze the onset of secretory deficits, we analyzed blood glucose levels and plasma insulin in P7, P15 and 1 month old animals (Supplementary Figure 2 B, D, E, and F). P7 and P15 animals were not fasted prior to analysis, 1 month old animals were fasted for 6 h.

Whilst blood glucose levels in $Ins2^{C109G}$ were already significantly elevated from P7 on at all further time points, plasma insulin was not significantly different. At 1 month, more

hormones were checked including analysis of insulin content from isolated islets. Indeed, insulin content was found to be already reduced at 1 month, indicating a very early onset of insulin deficiency (Supplementary Figure 2E). In the plasma, insulin and proinsulin were found to be decreased with one sample in even below the detection limit in Ins2^{C109G}. Additionally, at this age, the INS/PROINS ratio was significantly increased, differing from animals aged 8 weeks. The other hormones remained unaffected (Supplementary Figure 3A).

In contrast, in Ins2^{V26D} animals, blood glucose levels and plasma insulin were similar at P7 and P15 (Supplementary Figure 2D). Only at 1 month of age, fasting blood glucose was increased whilst plasma insulin and insulin content in isolated islets both were significantly reduced (Supplementary Figure 2F). Proinsulin was also significantly reduced which was accompanied by an increased INS/PROINS ratio (Supplementary Figure 3B). Further, glucagon was significantly upregulated and there was less C-peptide detected which was not the case in 2-month-old animals.

In conclusion, we show that the phenotype manifests very early in life, in Ins2^{C109G} already at P7, differing thereby from Ins2^{V26D}, where the first significant differences are observed at 1 month of age. Interestingly, INS/PROINS ratios were significantly increased at 1 month of age, but not at 2 months. Further, it can be stated that in both mouse lines the respective mutation manifests itself in a stronger phenotype in males compared to females.

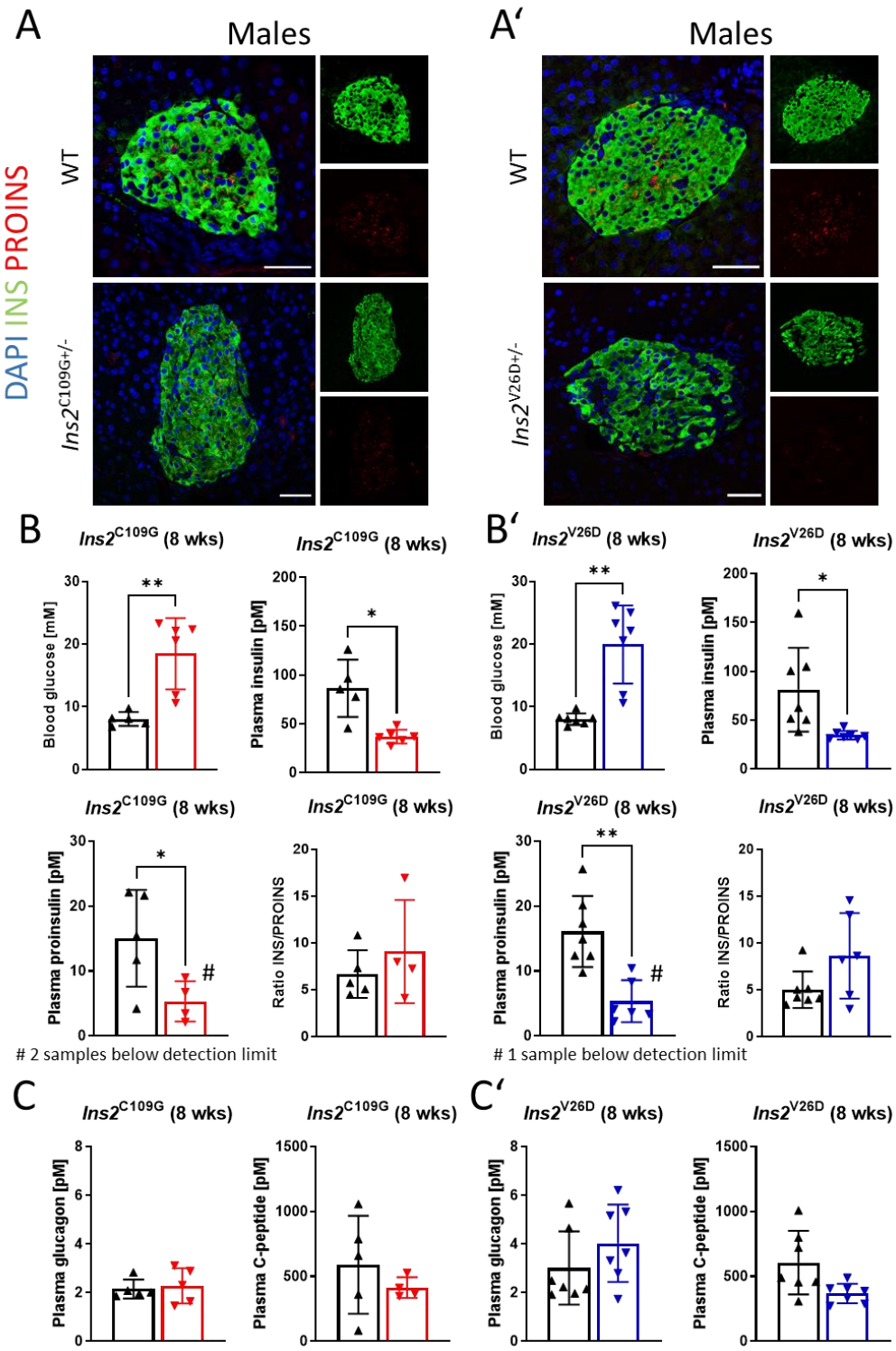

Figure 14 No aberrant localization of proinsulin, but reduced insulin and proinsulin secretion to the plasma in males

(A-A') Representative images of islets of Langerhans of **(A)** Ins2^{C109G} or **(A')** Ins2^{V26D} and WT animals. DAPI: blue, insulin: green, proinsulin: red. Scale bars equal 50 µm. **(B-B')** Blood glucose [mM], plasma insulin [pM], plasma proinsulin [pM] and ratio of insulin/proinsulin from 8-week-old 6 h fasted **(B)** Ins2^{C109G} and **(B')** Ins2^{V26D} and WT mice; n=4-7. **(C-C')** Plasma glucagon [pM] and plasma C-peptide [pM] from 8-week-old 6 h fasted **(C)** Ins2^{C109G} and **(C')** Ins2^{V26D} and WT mice; n=4-7.

4.1.2 Altered insulin tolerance in 20-week-old animals

To analyze whether animals remain sensitive to insulin and to examine whether sensitivity changes over time, ipITTs were performed at 10 weeks and 20 weeks of age as described in 3.2.4.2. At 10 weeks, animals of both lines did not show signs of impaired insulin tolerance (Figure 15A-B). However, in 20-week-old animals we observed differences between the two mouse lines. Exogenous insulin lowered blood glucose significantly stronger in $Ins2^{C109G}$ males compared to WT including a smaller AUC (Figure 15A'). In contrast, $Ins2^{V26D}$ males showed a delayed response to insulin, which was associated with an increased AUC.

In females, effects were less pronounced. Only in 20-week-old $Ins2^{C109G}$ females a slightly delayed response to insulin without any concomitant change in the AUC was observed. In $Ins2^{V26D}$ females, no significant changes were observed (Supplementary Figure 4A-A').

In summary, mutant animals develop an aberrant response to exogenous insulin over time.

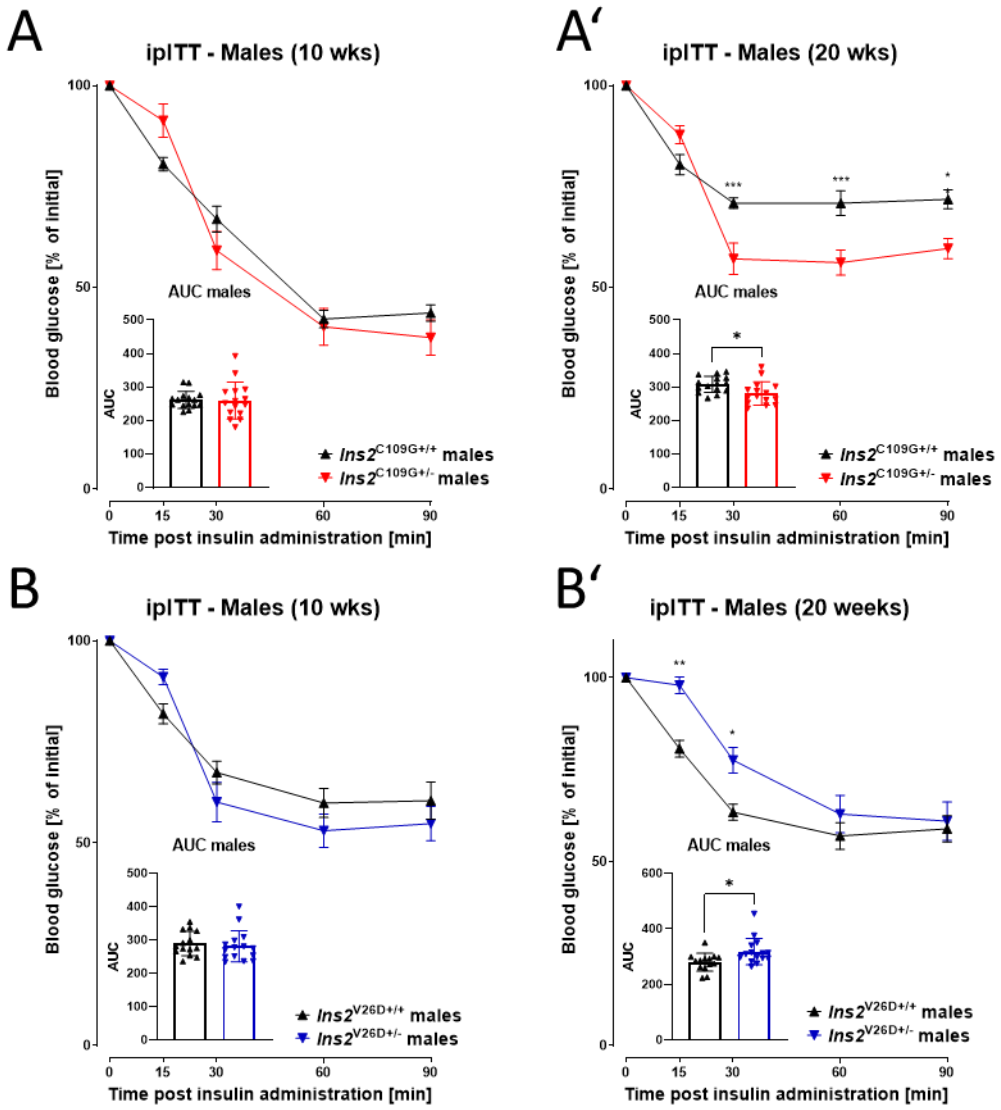

Figure 15 Altered insulin tolerance in 20-week-old males

(A) ipITT (0.75U/kg BW) in 10-week-old Ins2^{C109G} and WT; AUC; n=14-15. **(A')** ipITT (0.75U/kg BW) in 20-week-old Ins2^{C109G} and WT, AUC; n=14-15. **(B)** ipITT (0.75U/kg BW) in 10-week-old Ins2^{V26D} and WT, AUC; n=15. **(B')** ipITT (0.75U/kg BW) in 20-week-old Ins2^{V26D} and WT, AUC; n=14-15.

4.1.3 **Loss of functionally mature β-cell identity**

Hyperglycemia, or diabetes, independent of the type, is either accompanied by or the result of β-cell dysfunction. In a next step, we tested the expression of genes associated with the maturation and identity of functional β-cells [23] in isolated islets from 8-week-old animals. We observed a significant downregulation of *Ins2*, *Ins1*, *Pdx1*, *Mafa*, *Ucn3* and *Slc2a2* (Figure 16A-A') in male mutants compared to wild types of both lines, while *Pax6* was only downregulated in $Ins2^{C109G}$ animals (Figure 16A). In females, the aforementioned genes were also downregulated significantly in both models, although to a lesser degree. Interestingly, *Ins2* and *Ins1* were not downregulated in $Ins2^{C109G}$ females (Supplementary Figure 4B-B'), providing a possible explanation for the milder phenotype and stressing again the sexual dimorphism.

In addition, we performed immunohistochemistry on pancreatic sections of male animals aged 8 weeks with a combination of INS, GCG and NKX6-1, another crucial β-cell identity marker [25]. We counted mature β-cells as double positive for INS and NKX6-1 and observed a significantly decreased number of NKX6-1+/INS+ double positive cells in $Ins2^{V26D}$ mutant animals, but only a trend towards a decreased number in $Ins2^{C109G}$ mutants (Figure 16B-B') compared to wild types. Furthermore, in $Ins2^{V26D}$ mutants we also detected an increased number of cells positive for INS and GCG, which may indicate the existence of polyhormonal cells. A few of them are highlighted in the images (Figure 17B').

Taken together, these results suggest loss of functionally mature β-cell identity in mutant males of both $Ins2^{C109G}$ and $Ins2^{V26D}$ at the age of 8 weeks, while effects of the mutation in females were less pronounced.

We next analyzed the expression of genes encoding for other pancreatic hormones. The α-cell genes *Gcg* and *Mafb*, as well as the genes encoding for the pancreatic hormones somatostatin (*Sst*), pancreatic polypeptide (*Ppy*) and ghrelin (*Ghrl*) as well as glucokinase (*Gck*), were not significantly regulated in $Ins2^{C109G}$ islets (Figure 16C), while in $Ins2^{V26D}$ only *Gcg* expression was upregulated (Figure 16D) compared to expressions in wild types. In conclusion, in $Ins2^{C109G}$ and $Ins2^{V26D}$ mutant animals, other cell types were largely unaffected, suggesting a β-cell-specific effect of both mutations.

Similar gene expression analyses were performed in younger animals aged 4 weeks to check progression of the disease and analyze potential differences compared to 8 weeks-old animals. Indeed, we observed downregulation of all the aforementioned genes associated with mature β-cells already at younger age. Further, *Ngn3* was increased significantly (see also 1.4.5). The data is shown in Supplementary Figure 5A-B and Supplementary Figure 6A-B and is discussed in the discussion section of this thesis.

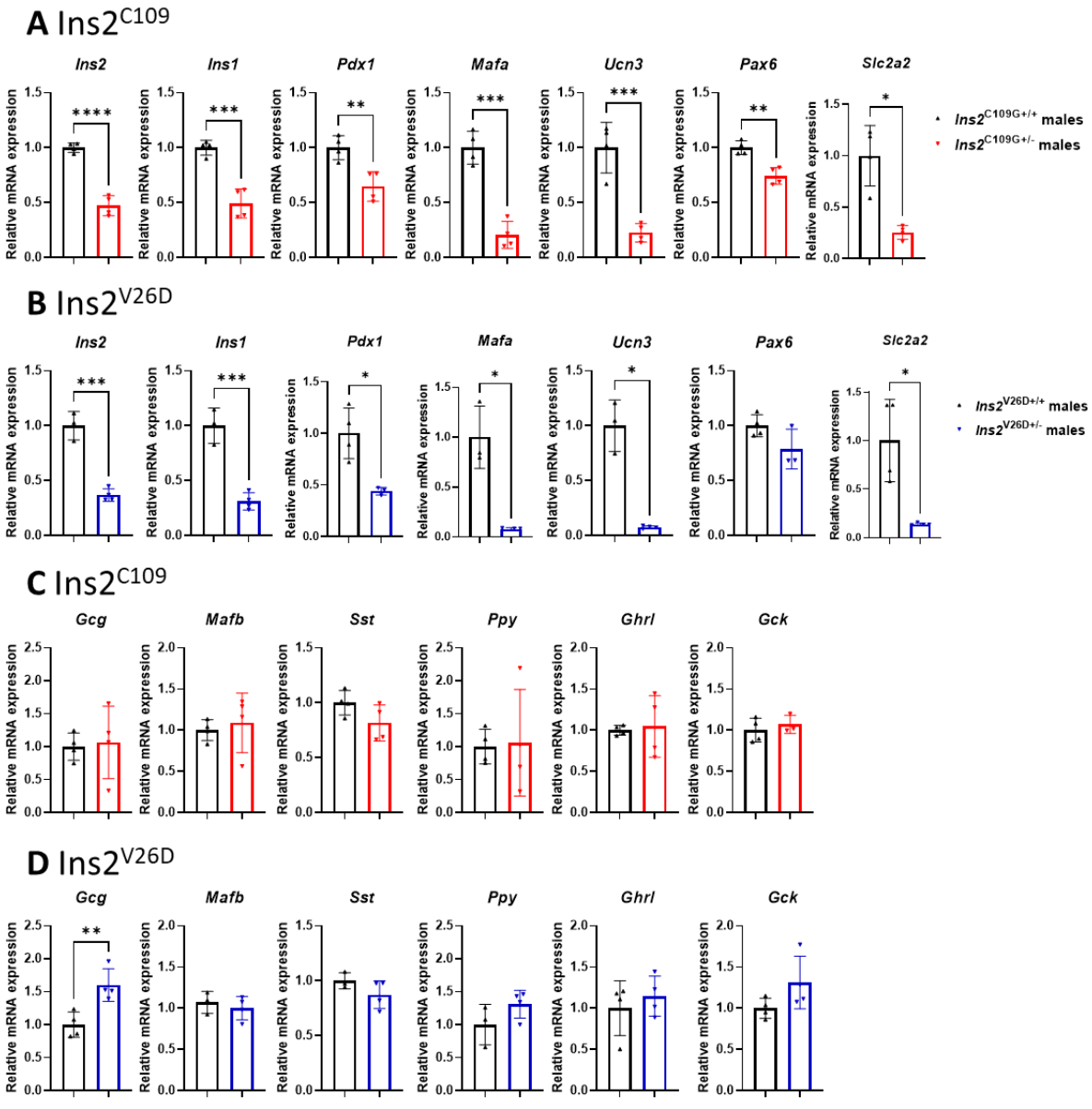

Figure 16 Loss of functionally mature β-cell identity

(A-B) Relative mRNA expression of *Ins2*, *Ins1*, *Pdx1*, *Mafa*, *Ucn3*, *Pax6* and *Slc2a2* in 8 weeks old **(A)** Ins2^{C109G} and **(B)** Ins2^{V26D} males compared to WT; n=3-4. **(C-D)** Relative mRNA expression of *Gcg*, *Mafb*, *Sst*, *Ppy*, *Ghrl* and *Gck* in **(C)** Ins2^{C109G} and **(D)** Ins2^{V26D} males compared to WT; n=3-4.

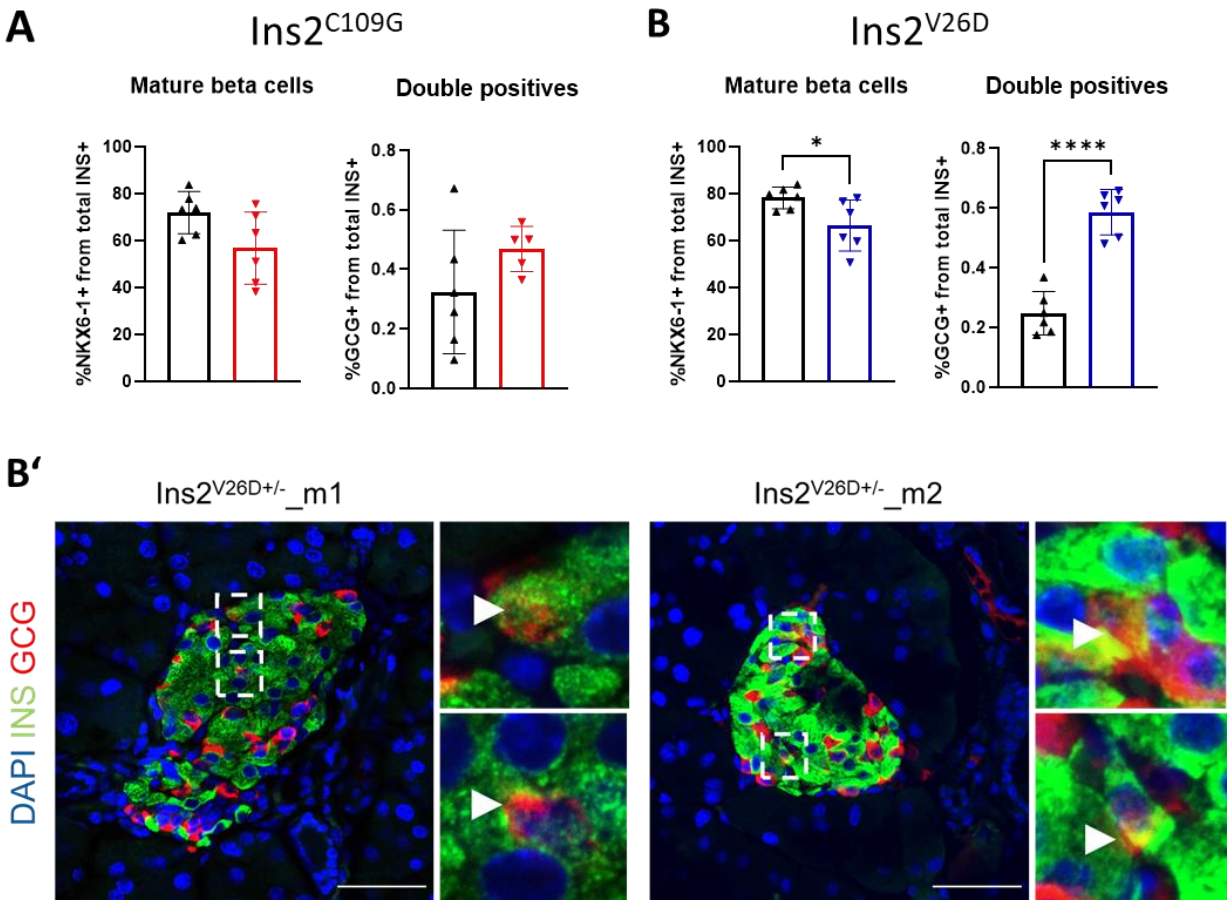

Figure 17 Mature β-cells and double positive cells (INS+GCG+)

(A-B) Evaluation of NKX6-1+ from INS+ cells in % and GCG+ from INS+ cells in % of 8 weeks old **(A)** *Ins2*^{C109G} and **(B)** *Ins2*^{V26D}. **(B')** Representative images of islets of Langerhans highlighting the presence of insulin and glucagon double-positive cells in Ins2$^{V26D+/-}$ mice. Scale bars equal 50 µm in all panels; n=6.

4.1.4 Severe dilation of the ER and displaced calreticulin

As described in the introduction, misfolding of insulin is quite common due to the generally high load of proinsulin synthesis. Mutations in the insulin gene can additionally increase misfolding and lead to potential accumulation of misfolded molecules in the ER (see also 1.4.1). As known for *Ins2* mutant C96Y (Akita), misfolded proinsulin accumulates in the ER [89]. We therefore analyzed β-cells of *Ins2* mutants C109G and V26D together with wild-type littermates aged 8 weeks by transmission electron microscopy (TEM) (imaging performed by Thomas Kurth, TU Dresden). In addition, we performed immunohistochemistry on pancreatic sections from animals of the same age to detect proinsulin and calreticulin, which is an ER-resident soluble chaperone [144].

In fact, we observed a highly distended rough endoplasmic reticulum (rER) in mutants of both models compared to wild types (Figure 18A-A'). Other organelles appeared normal. The subsequent co-staining of proinsulin (PROINS) and calreticulin (CALR) showed that calreticulin was not as clearly arranged around the nucleus as observed in the wild types and it did not co-localize with proinsulin, especially in C109G mutants (Figure 18B-B') whilst in wild types, co-localization was visible.

A co-staining of proinsulin with the Golgi membrane-marker GRASP65 was inconspicuous in both models (Supplementary Figure 7) and, as in the wild type, showed co-localization of proinsulin with the Golgi apparatus in both mutants (arrows in Supplementary Figure 7). The additional staining for the ER-membrane marker calnexin (CALN) showed a less dense signal, which is consistent with the observed displaced CALR staining.

Taken together, we observed a severely dilated ER in the β-cells of both models, concomitant with displaced calreticulin and calnexin. Otherwise, proinsulin is present in the Golgi apparatus.

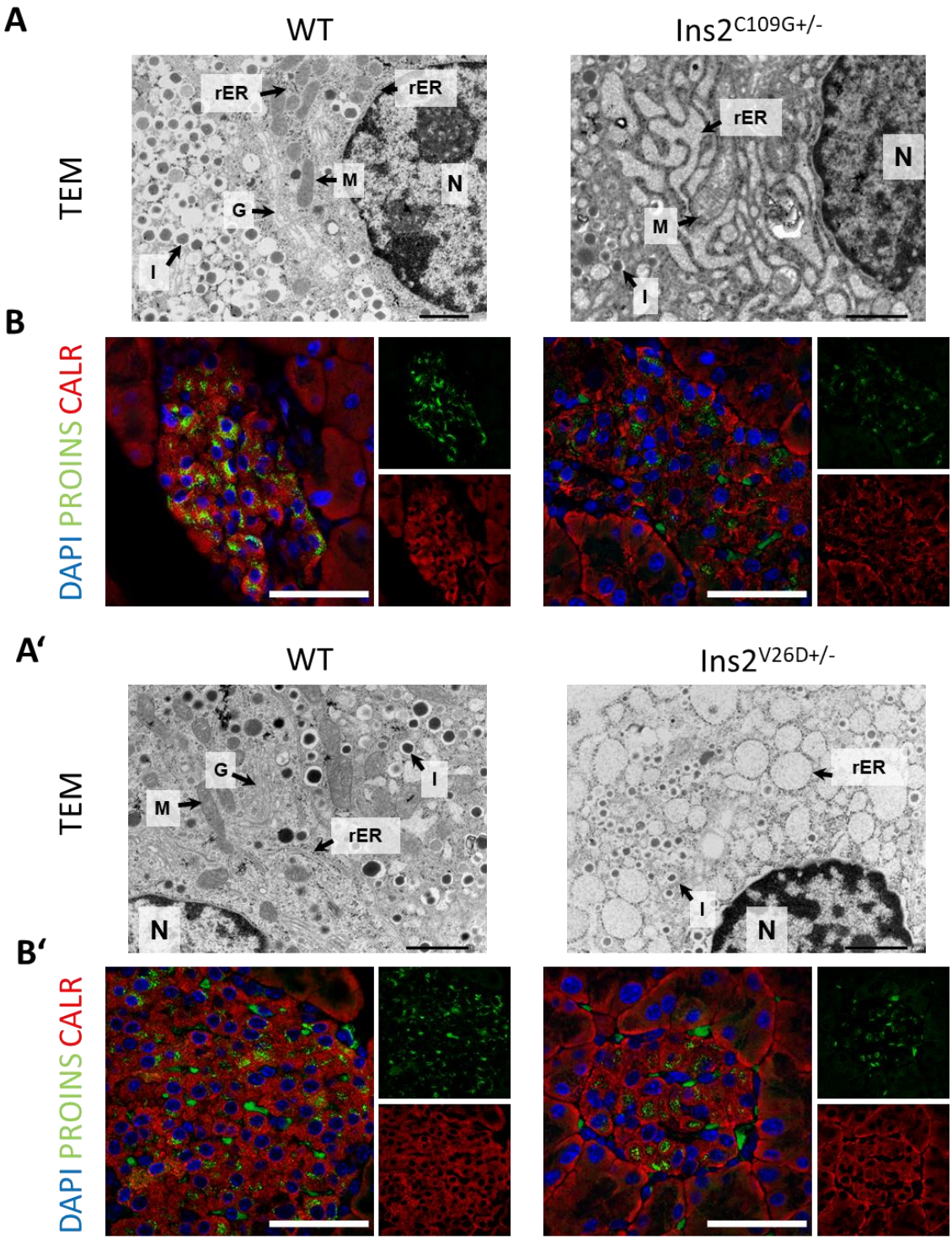

Figure 18 Severely enlarged rER and displaced calreticulin

(A-A') Representative transmission electron microscopic (TEM) images of β-cells of 8-week-old **(A)** Ins2^{C109G} and **(A')** Ins2^{V26D} and respective WT males. Scale bars equal 5 µm. Exemplary cellular structures are denoted as follows: G= Golgi apparatus; I= insulin granule; M= mitochondrion; N= nucleus; rER= rough endoplasmic reticulum. **(B-B')** Representative images of islets of Langerhans' of **(B)** Ins2^{C109G} and **(B')** Ins2^{V26D} and respective WT males. DAPI: blue, proinsulin: green, calreticulin: red. Scale bars equal 20 µm.

4.1.5 Dysregulation of PDI genes, PDIA1 and ERO genes

The amino acid substitutions in the insulin gene and the observed severe dilation of the ER make a misfolding of proinsulin in both mouse models very likely [36], which is why we expected a different regulation of genes associated with oxidative folding of proteins, namely protein disulfide isomerases (PDIs) and ER-oxidoreductins (EROs) (see also 1.4.3 for the oxidative folding of proinsulin). Effects could be visible especially in $Ins2^{C109G}$, where one of the three disulfide bonds is disrupted due to the cysteine-to-glycine substitution. In $Ins2^{V26D}$ animals, no disulfide bond is disrupted, however we observed an equally strong dilation of the ER, which prompted further investigation.

We analyzed the expression of three key genes for protein disulfide isomerases (*Pdia1*, *Pdia4* and *Pdia6*), which have been shown to play important roles in insulin folding [61, 100] and two key ER-oxidoreductins (*Ero1a*, *Ero1b*) in the islets of 8 week-old mutant animals and wild types. ER-oxidoreductins are responsible for the re-oxidation of PDIs, especially of PDIA1 [59] and thus also play an important role in proinsulin folding. *Ero1a* is expressed in most tissues, while *Ero1b* is specifically enriched in pancreatic islets [62]

In $Ins2^{C109G}$ animals, the expressions of *Pdia4* and *Pdia6* were significantly upregulated compared to wild types, while this was not the case for *Pdia1*. However, when we analyzed protein expression of PDIA1, because it is the most abundant oxidoreductase and was shown to directly interact with proinsulin [61], we found significantly increased PDIA1 protein (Figure 19A). Additionally, *Ero1b* was significantly downregulated (Figure 19B).

Although no disulfide bond is disrupted in $Ins2^{V26D}$ animals, we observed an upregulation of *Pdia1*, *Pdia4* and *Pdia6* gene expression as well as PDIA1 protein expression, accompanied by a downregulation of both *Ero1a* and *Ero1b* (Figure 19A'-B') compared to wild types. This finding shows that non-cysteine mutations may influence the expression of genes and proteins that are involved in oxidative folding.

Some effects were also present in females aged 8 weeks. In $Ins2^{C109G}$ females, *Pdia4* was upregulated and *Ero1a* and *Ero1b* were downregulated (Supplementary Figure 9A-B) compared to wild types. In $Ins2^{V26D}$ females *Pdia1*, *Pdia4* and *Pdia6* were upregulated whilst *Ero1a* and *Ero1b* were downregulated compared to wild types. This shows again,

that whilst there is only small macroscopic effects (mild hyperglycemia), yet on the molecular layer effects are present.

Additionally, the same genes were analyzed in younger animals to determine the time course of gene dysregulation. Indeed, gene regulation in younger (1 month old) male animals was similar to animals aged 2 months, hinting that molecular effects are already present at younger ages (Supplementary Figure 5 C and Supplementary Figure 6 C).

Taken together, these results suggest that, in addition to the misfolding due to mutations, the folding in both models may also be further disturbed by unfavorable redox conditions. Remarkably, these effects were already visible in younger animals.

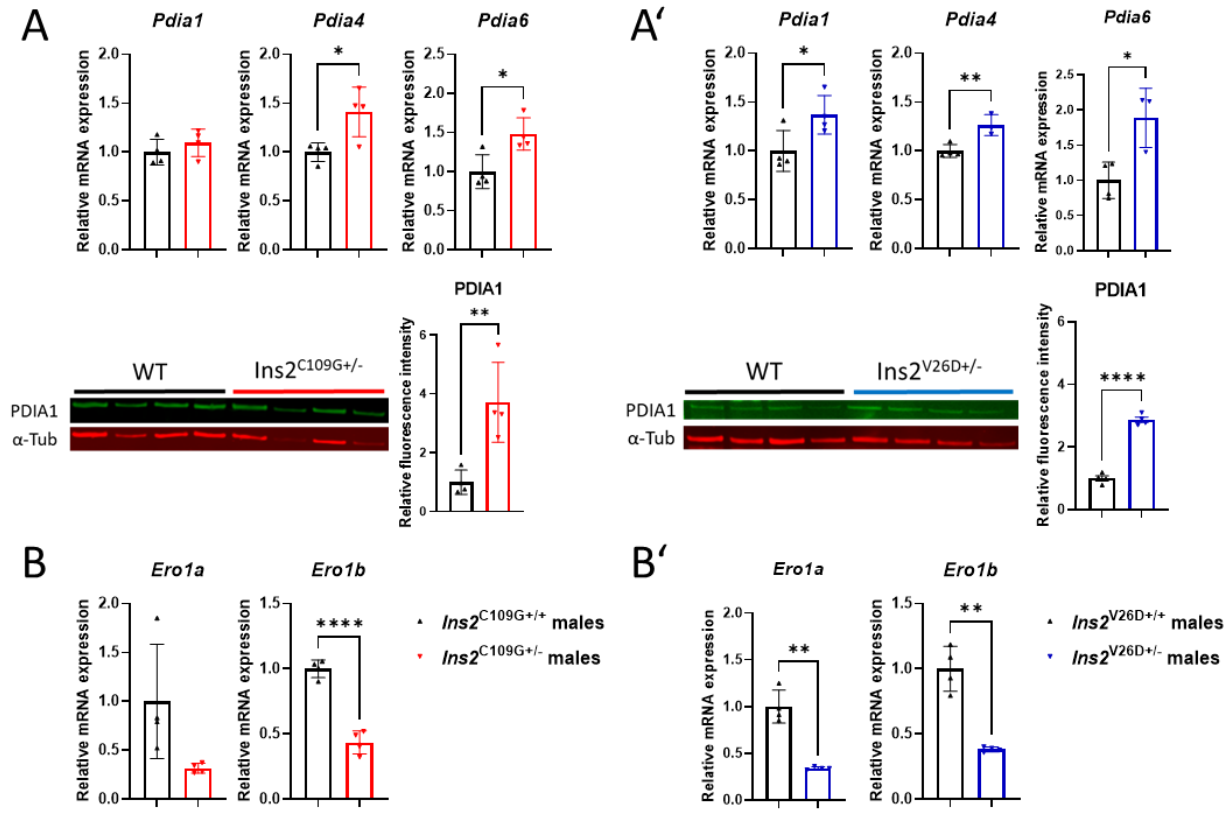

Figure 19 Dysregulation of PDI genes, PDIA1 and ERO genes

(A-A') Relative mRNA expression of *Pdia1*, *Pdia4* and *Pdia6* in **(A)** Ins2^{C109G} and **(A')** Ins2^{V26D} males at the age of 8 weeks compared to WT; n=3-4; PDIA1 protein expression as relative fluorescence intensity; n=4. **(B-B')** Relative mRNA expression of *Ero1a* and *Ero1b* in **(B)** *Ins2*^{C109G} and **(B')** *Ins2*^{V26D} males compared to WT; n=3-4.

4.1.6 Effects of the mutations on ER-stress, UPR and autophagy in islets

A severe dilation of the ER, as shown by TEM images (Figure 18), misfolding of proteins, which is suspected due to the mutations, and an unfavorable oxidative milieu, as illustrated by a dysregulation of PDI- and ERO genes (Figure 19), are all potentially accompanied by ER-stress and, subsequently, by an increase in the unfolded protein response (UPR) (as described in 1.4.2). Therefore, we analyzed the expression of a subset of ER-stress associated genes and some of its downstream targets in the islets of 8 week-old mutant and wild type animals. Contrary to our expectation, the three key transducers and sensors for ER-stress, *Ire1a*, *Eif2ak3* and *Atf6*, were not upregulated in both mutants compared to wild types. In Ins2^{C109G}, *Ire1a* was even downregulated (Figure 20A-A'). To further assess the downstream effects of possible ER-stress on UPR, we analyzed expression of the ER-resident chaperone BiP, which is encoded by *Hspa5* and known to recruit misfolded proinsulin [36]. Although *Hspa5* was not regulated in both models, we observed significantly increased BiP protein in the islets of *Ins2*^{C109G} mutants but not in *Ins2*^{V26D}. Interestingly, also *Ddit3*, encoding CHOP, expression was not significantly regulated in both models (Figure 20B-B') compared to wild types.

Next, we analyzed the expression of *Sqstm1* (encoding for P62) and *Map1lc3* (encoding for LC3B) in islets of 8-week-old animals, two key players in autophagy. Autophagy is tightly intertwined with insulin homeostasis in β-cells [66]. For more details on autophagy see also 1.4.4. Indeed, in both models we observed a significant downregulation of *Sqstm1* while *Map1lc3* expression remained unaffected compared to wild types. Upon western-blot analysis, P62 was detected only in the islets from wild types, but not in mutant animals (Figure 20C-C'). Further, staining with proinsulin and P62 showed that there is less P62 present in islets (Supplementary Figure 8).

We conclude, that whilst there is only few molecular signs of ER-stress such as increased BiP protein, both *Ins2* mutations appear to have effects on the expression of autophagy-associated genes and proteins.

Gene expression analysis was also performed in 8-week-old female animals. Some differential effects compared to males were present. In Ins2^{C109G} females, we found downregulated *Ire1a*, *Atf6* and *Sqstm1* compared to wild types. In Ins2^{V26D} females, we

found upregulated *Eif2ak3* and downregulated *Atf6* and *Sqstm1* compared to wild types. Results are shown in Supplementary Figure 9A-C.

Additionally, gene expression analysis of ER-stress- and autophagy-associated genes was performed in 4-week-old animals to investigate whether there are some age-dependent differential effects. Results are shown in Supplementary Figure 5D and Supplementary Figure 6D. At 1 month of age, different to 2 months, *Hspa5* was upregulated in $Ins2^{C019G}$ compared to wild types. Further, both *Sqstm1* and *Map1lc3* were downregulated. In $Ins2^{V26D}$ mutants, *Ire1a*, *Atf6*, *Ddit3* and *Sqstm1* were downregulated compared to wild types. *Hspa5* was upregulated. Taken together, these results show that with progression of the disease, expression profiles of genes change.

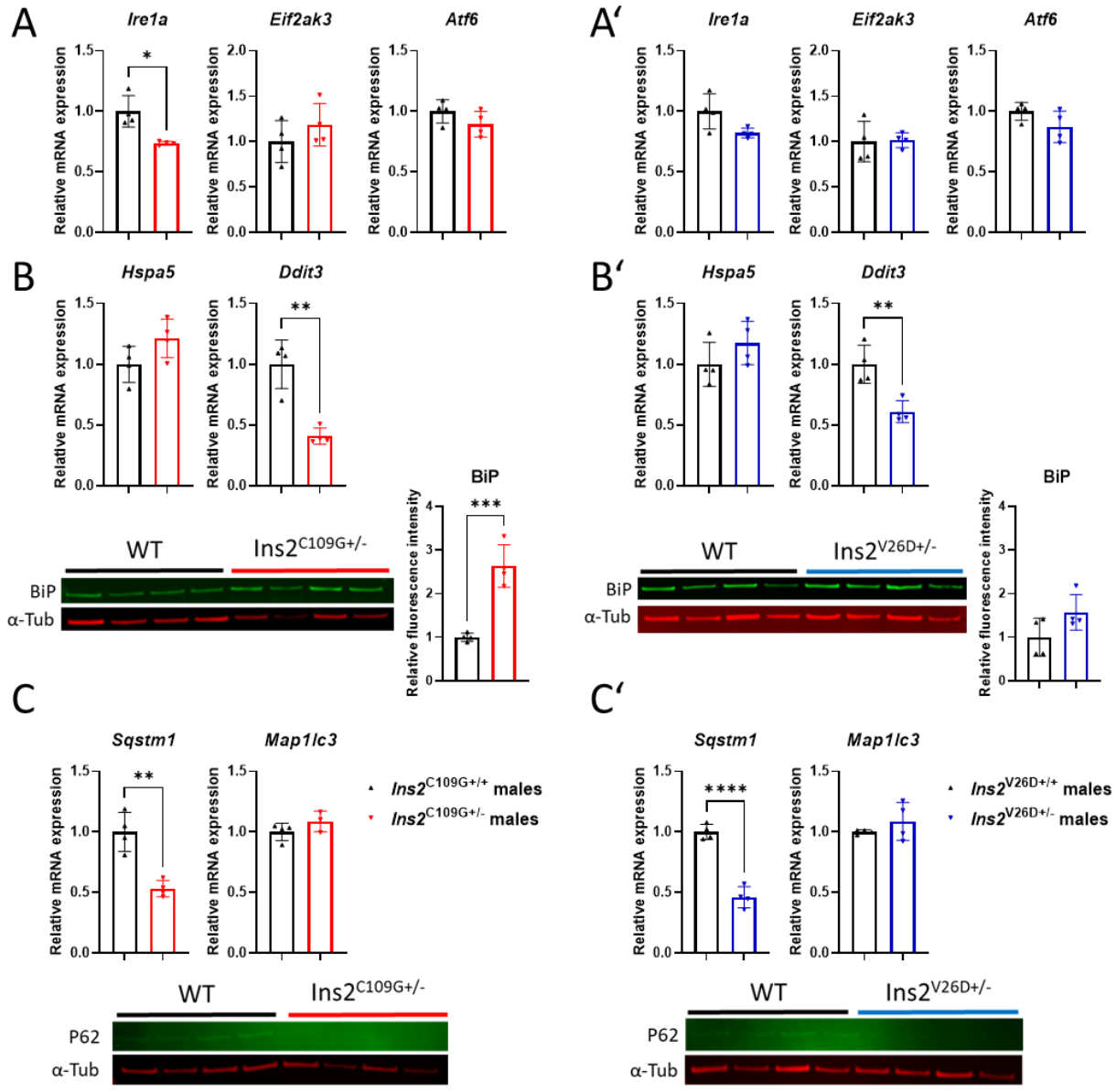

Figure 20 ER-stress sensors and autophagy in islets

(A-A') Relative mRNA expression of *Ire1a*, *Eif2ak3*, *Atf6* in 8-week-old **(A)** Ins2^{C109G} and **(A')** Ins2^{V26D} males compared to WT; n=3-4. **(B-B')** Relative mRNA expression of *Hspa5* and *Ddit3* in 8-week-old **(B)** Ins2^{C109G} and **(B')** Ins2^{V26D} males compared to WT; n=3-4. BiP as relative fluorescence intensity in 8-week-old **(B)** Ins2^{C109G} and **(B')** Ins2^{V26D} males compared to WT; n=4. **(C-C')** Relative mRNA expression of *Sqstm1* and *Map1lc3* in 8-week-old **(C)** Ins2^{C109G} and **(C')** Ins2^{V26D} males compared to WT; n=3-4.

4.1.7 Summary and conclusion for Ins2^{C109G} and Ins2^{V26D}

In summary, we observed severe early-onset hyperglycemia for both novel *Ins2* models, accompanied by hypoinsulinemia and hypoproinsulinemia. Reduced β-cell mass and a reduced mean islet size were only detected in Ins2^{C109G} animals. Furthermore, we demonstrated a loss of functionally mature β-cell identity for both *Ins2* models and a severely enlarged ER. The oxidative milieu seems to be disrupted, since we observed differences in PDI- and ERO-gene expression and PDIA1 protein between mutants and wild types in both models. Surprisingly, the ER-stress pathways were only marginally affected, suggesting that, in addition to ER-stress, other mechanisms may also play a role in disease pathogenesis. Indeed, we observed deregulation of *Sqstm1*/P62, suggesting that autophagy could be an additional mechanism. In conclusion, through in-depth phenotyping of two *Ins2* mouse models, we uncovered similarities and differences that provide valuable insights into the pathophysiology of MIDY and can help to explain why different mutations in the same gene lead to different phenotypes. In addition, these animals can provide valuable insights into β-cell survival mechanisms, which in turn are relevant for the more complex pathophysiology of the multifactorial diseases T1D and T2D. A summarized overview is provided below:

Summary Ins2^{C109G}

- First mouse model with loss of A20-B19 disulfide bond
- Human patient(s): yes
- Severity of the phenotype ↑ ↑
- β-cell mass, mean islet size ↓
- β-cell identity ↓
- Dilation of the ER ↑ ↑ ↑
- Oxidative milieu: PDIA1 ↑ ↑ *Ero1b* ↓
- ER-stress: *Ire1a* ↓ BiP ↑
- Autophagy: *Sqstm1* ↓ P62 ↓

Summary Ins2^{V26D}

- First mouse model with non-cysteine mutation at B2
- Human patient(s): no
- Severity of the phenotype ↑ ↑ ↑
- β-cell mass, mean islet size ↔
- β-cell identity ↓ ↓ ↓
- Dilation of the ER ↑ ↑ ↑
- Oxidative milieu: PDIA1 ↑ *Ero1a/b* ↓
- ER-stress: ↔
- Autophagy: *Sqstm1* ↓ P62 ↓

Legend: ↑ increased ↔ similar ↓ decreased

Figure 21 Summary for Ins2^{C109G} and Ins2^{V26D}

4.2 Neonatal diabetes mellitus caused by a *Pdia6* mutation: Characterization of the novel mouse model Pdia6^{F175S}

Within the scope of this thesis, one novel mouse model with a point mutation in the *Pdia6* gene was characterized. In a joint project with postdoctoral researcher Nirav Florian Chhabra (NFC), the Pdia6^{F175S} mouse model was recently published in September 2021 in Molecular Metabolism: "A point mutation in the *Pdia6* gene results in loss of pancreatic β-cell identity causing overt diabetes" (DOI: 10.1016/j.molmet.2021.101334) [100]. Therefore, the results are shown here in an abbreviated format presenting my personal contributions to the publication and unpublished data. A few results from our collaboration partners (from the Institute for Diabetes and Regeneration (IDR) at the Helmholtz Zentrum München) and from NFC, which serve to link results, are included, but clearly marked and cited. An overview of the different experimental contributions is provided in Figure 22.

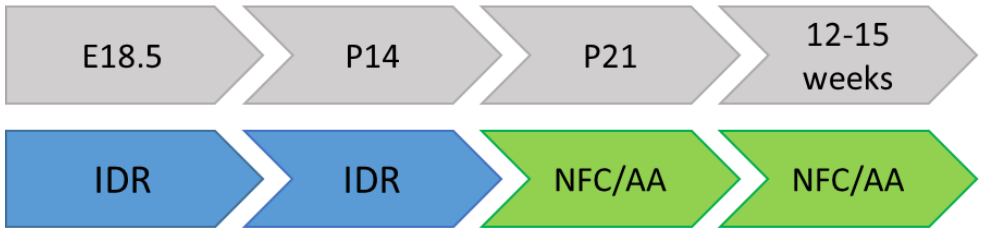

Figure 22 Overview of experimental contributions to the PDIA6 project

4.2.1 Identification of a novel *Pdia6* mutant mouse line

Like the two *Ins2* mouse lines, the Pdia6^{F175S} mouse line derived from the Munich ENU mutagenesis screen [141]. After identification of the chromosomal position as previously described [142] and at least 10 generations of outcrosses, the point mutation was confirmed by sequence analysis, which lead to the official name Pdia6^{F175SMhda}, here abbreviated to Pdia6^{F175S}. In Pdia6^{F175S} mice, the phenylalanine (hydrophobic, nonpolar) at position 175 in the second thioredoxin domain of the PDIA6 protein is exchanged for a serine (hydroxylic, polar uncharged), which could impair its catalytic properties [64]. For this study, wild type, heterozygous (het) and homozygous (hom) animals were analyzed. Since we observed a reduced Mendelian ratio in mutant animals, the data obtained from animals were not separated by sex and analyzed together.

4.2.2 Unchanged PDIA6 protein levels in the pancreas, but reduced proinsulin and insulin content in Pdia6$^{F175S-/-}$ mice

Homozygous Pdia6^{F175S} mutants (hereafter referred to as Pdia6$^{F175S-/-}$) developed severe hyperglycemia that began shortly after weaning age and was associated with decreased body weight gain. In addition, we observed a reduced Mendelian ratio as early as embryonic day E18.5, which worsened after birth. At the age of 12-15 weeks, the insulin and proinsulin content of isolated islets was drastically reduced in Pdia6$^{F175S-/-}$ animals, while the plasma insulin level was not detectable with the regular Mercodia ELISA kit (experiments performed by NFC) [100].

To determine whether the F175S mutation had any effect on PDIA6 protein abundance in the pancreas, we performed western blot analysis and observed similar expression of PDIA6 protein in wild type, heterozygous and homozygous animals at the age of 21 days (P21), revealing that the F175S mutation does not affect the amount of PDIA6 protein in the pancreas (Figure 23A-A').

Since it is known that PDIA6 plays a role in the folding and processing of proinsulin to insulin and in insulin secretion [60, 145], we analyzed insulin and proinsulin expression and their localization in sections of the pancreas. Consistent with the very low amounts of insulin and proinsulin in isolated islets at a similar age [100], staining for both insulin and proinsulin was drastically reduced in mutant animals around 12 weeks of age (Figure 23B). A comparative gene expression analysis of isolated islets from adult mice showed in mutants a decreased expression of genes associated with β-cell identity, together with an increase in α-cell associated genes, which resulted in an increased glucagon content of Pdia6$^{F175S-/-}$ islets [100].

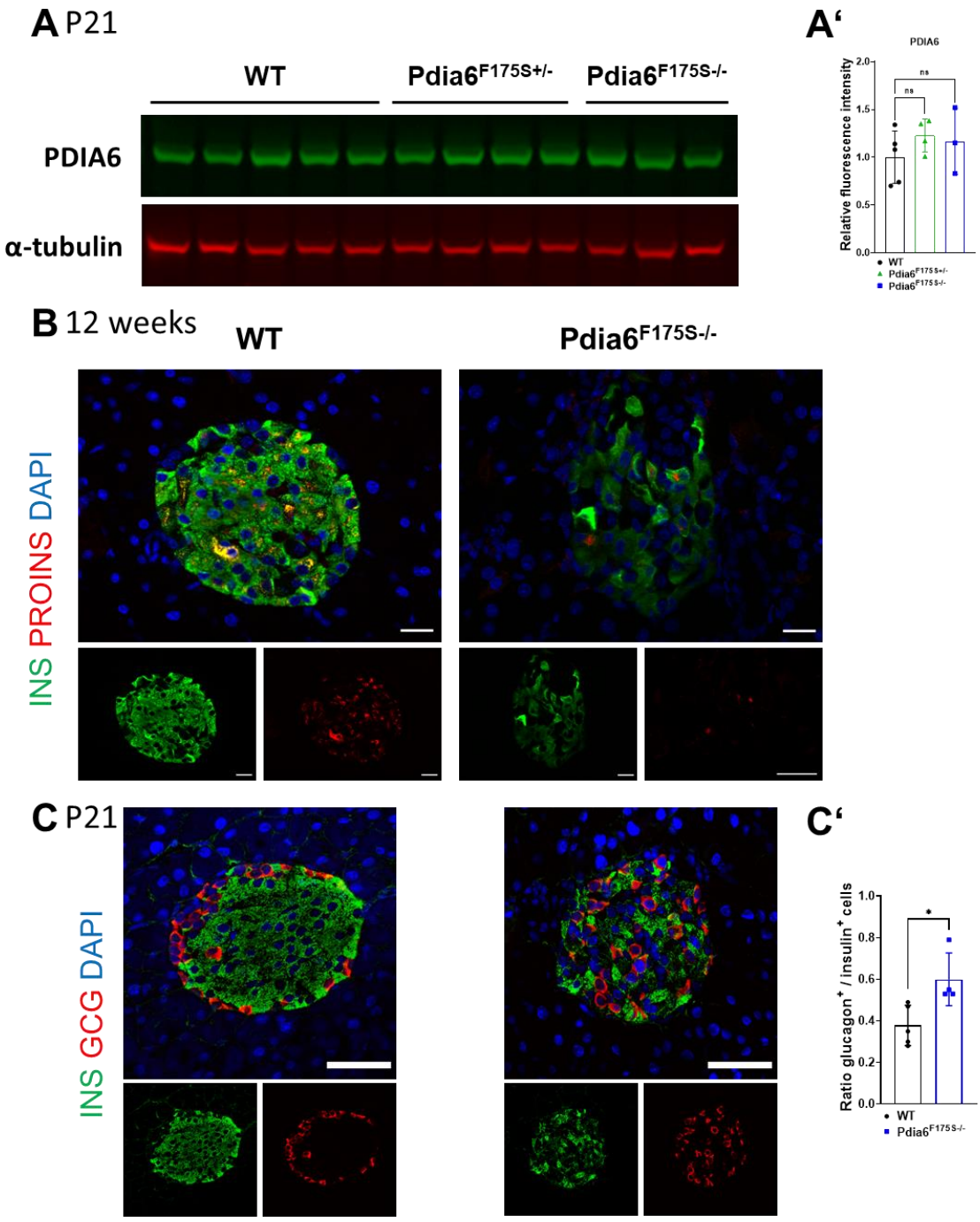

Figure 23 PDIA6, insulin, proinsulin and glucagon in the pancreas of Pdia6$^{F175S-/-}$

(A) Western blot analysis of pancreatic tissue from WT, Pdia6$^{F175S+/-}$ and Pdia6$^{F175S-/-}$ and **(A')** quantification thereof; n=3-5, age: P21. **(B)** Representative images of islets of Langerhans from Pdia6$^{F175S-/-}$ and WT animals. DAPI blue, insulin green, proinsulin red. Scale bars equal 20 µm; age 12 weeks. **(C)** Representative images of islets of Langerhans from Pdia6$^{F175S-/-}$ and WT animals. DAPI blue, insulin green, glucagon red. Scale bars equal 50 µm; Quantification: glucagon+ (α-cells) to insulin+ (β-cells)-cell ratio; age P21; n=4-5; This figure is adapted from Chhabra and Amend et al. 2021.

4.2.3 Loss of β-cells at postnatal stages without concomitant apoptosis

The elevated blood glucose levels of Pdia6$^{F175S-/-}$ mice as early as 4 weeks of age, together with a possible loss of β-cell identity in adult animals, prompted us to investigate earlier stages to determine the onset and progression of β-cell dysfunction.

Analysis of pancreatic sections from embryos in the late gestational phase (embryonic day E18.5) revealed no differences in islet composition [100]. However, at P14, α-cells were scattered across the islets, while their numbers were increased and the number of β-cells decreased [100]. These data suggest that pancreatic endocrine development is not disturbed *in utero* and that the effects of the Pdia6^{F175S} mutation on α- and β-cells must occur during postpartum maturation.

We next analyzed islets of mutant and wild type animals at weaning age (P21), where co-staining for insulin and glucagon revealed reduced insulin and centrally dispersed α-cells (Figure 23C). The morphometric analysis (carried out by Annette Feuchtinger) showed an increased α- to β-cell ratio (Figure 23C') similar to the observations in P14 [100].

We also examined the changes in α- and β-cell mass with regard to the occurrence of apoptosis or altered proliferation in multiple staining with chromogranin A, a marker of the endocrine lineage. We observed no changes in apoptosis and proliferation at P14 and normal expression of chromogranin A at P21, which supports the maintenance of endocrine lineage and lack of apoptosis [100].

Taken together, these results indicate that it is not β-cell death or α-cell proliferation that underlies the increased ratio of α- to β-cells. Thus, the apparent β-cell dysfunction and the resulting hyperglycemia must therefore be due to other mechanisms.

4.2.4 Loss of β-cell identity and presence of polyhormonal cells in pancreatic islets

As already mentioned, Pdia6$^{F175S-/-}$ islets showed a decreased expression of genes associated with β-cell identity and an increase in the expression of α-cell associated genes in adulthood [100]. Therefore, we analyzed the expression of a similar set of genes including *Pdia6* at P21 before the onset of extreme hyperglycemia. Interestingly, *Pdia6* mRNA levels were significantly upregulated in mutant islets. While *Ins2* expression was

significantly reduced, expression of the β-cell specific genes *Slc2a2, Ucn3* and *Mafa* was not regulated in Pdia6$^{F175S-/-}$ islets. On the other hand, *Gcg* expression was increased, while expression of the α-cell specific gene *Mafb* remained unchanged (Figure 24A). In addition, we analyzed the β-cell transcription factors NKX6-1 and PDX1 by immunostaining on pancreatic sections at P21 and found a significant reduction in the number of NKX6-1-positive and PDX1-positive cells in Pdia6$^{F175S-/-}$ animals compared to wild-type littermates (quantifications performed by NFC) (Figure 24B-C). These results prompted us to further investigate co-staining for INS and GCG in pancreatic sections at P21. Indeed, we observed several cells in Pdia6$^{F175S-/-}$ animals that were positive for both insulin and glucagon (Figure 24D).

Taken together, Pdia6^{F175S} animals show only some signs of loss of β-cell identity at P21, such as reduced expression of *Ins2*, PDX1 and NKX6-1. Furthermore, a subset of cells expresses both insulin and glucagon, which may explain the increased α- to β-cells ratio in the absence of apoptosis as mentioned above and in [100]. The loss of β-cell identity is more evident in comparison with the analysis of gene expression in adult mice (12-15 weeks), where the loss of β-cell-specific gene expression may have already been exacerbated by persistent hyperglycemia [30, 100]. Therefore, the data suggests that the F175S mutation results in a progressive loss of β-cell identity, beginning around weaning age and deteriorating with increasing age.

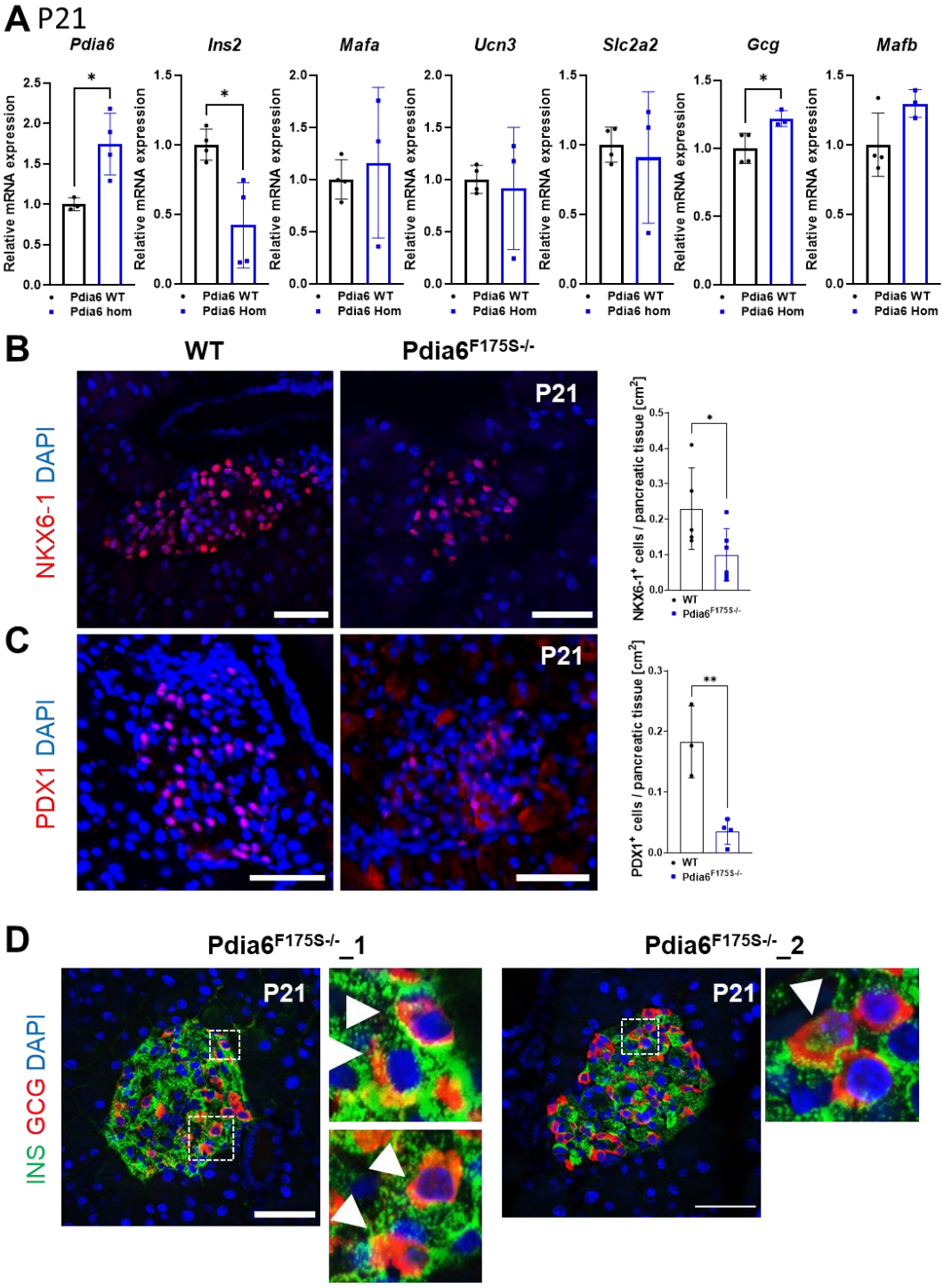

Figure 24 Loss of β-cell identity at P21 in Pdia6$^{F175S-/-}$

(A) Relative mRNA expression of *Pdia6*, *Ins2*, *Mafa*, *Ucn3*, *Slc2a2*, *Gcg* and *Mafb* in Pdia6$^{F175S-/-}$ and WT islets; n=3-4. **(B-C)** Representative images of islets of Langerhans and quantification of β-cell markers NKX6-1 **(B)** and PDX1 **(C)**; n=3-6. **(D)** Representative images of islets of Langerhans highlighting the presence of insulin and glucagon double-positive cells in Pdia6$^{F175S-/-}$ mutant mice. Scale bars equal 50 µm in all panels. Mice at age P21 were used in all experiments. This figure is adapted from Chhabra and Amend et al. 2021.

4.2.5 The Pdia6^{F175S} mutation leads to modest ER-stress

Since PDIA6 is involved in the formation of disulfide bridges and in the processing of proinsulin to insulin (as explained in 1.4.1) the F175S mutation could impair its function in such a way that misfolding, oxidative stress and, as a result, ER-stress arise.

We therefore assessed the expression of a subset of other PDI genes, ERO genes and genes associated with ER-stress on islet RNA from wild-type and mutant animals at P21. We found unchanged expression of *Pdia1*, *Pdia4* and *Ero1b*, while *Pdia6* was upregulated and *Ero1a* was downregulated (Figure 25A). Although the expression of the ER-stress sensor *Atf6* was not changed in Pdia6$^{F175S-/-}$ islets, the expression of *Ire1a*, *Eif2ak3*, *Hspa5* and *Ddit3* was increased (Figure 25A). In addition, we analyzed the same subset of PDIs (PDIA1, 4, 6) as well as some ER-stress sensors and effectors (IRE1A, PERK, BIP, CHOP) on the protein level using pancreatic tissue from animals at P21. We found an increase in BiP and PDIA4 protein and a decrease of CHOP, revealing a discrepancy with its gene expression (Figure 25B-D). PDIA6 (Figure 23A), PDIA1, IRE1A and PERK protein levels were not significantly changed between mutant and wild-type animals (Supplementary Figure 11). The levels of phosphorylated IRE1A and phosphorylated PERK, the active versions of the sensors, also did not change, which effectively resulted in unaltered P-IRE1A/IRE1A and P-PERK/PERK ratios (Supplementary Figure 11B-C).

In conclusion, in can be said that at P21 only a modest increase of oxidative stress and ER-stress were noticeable. Parts of these results were included in the publication [100].

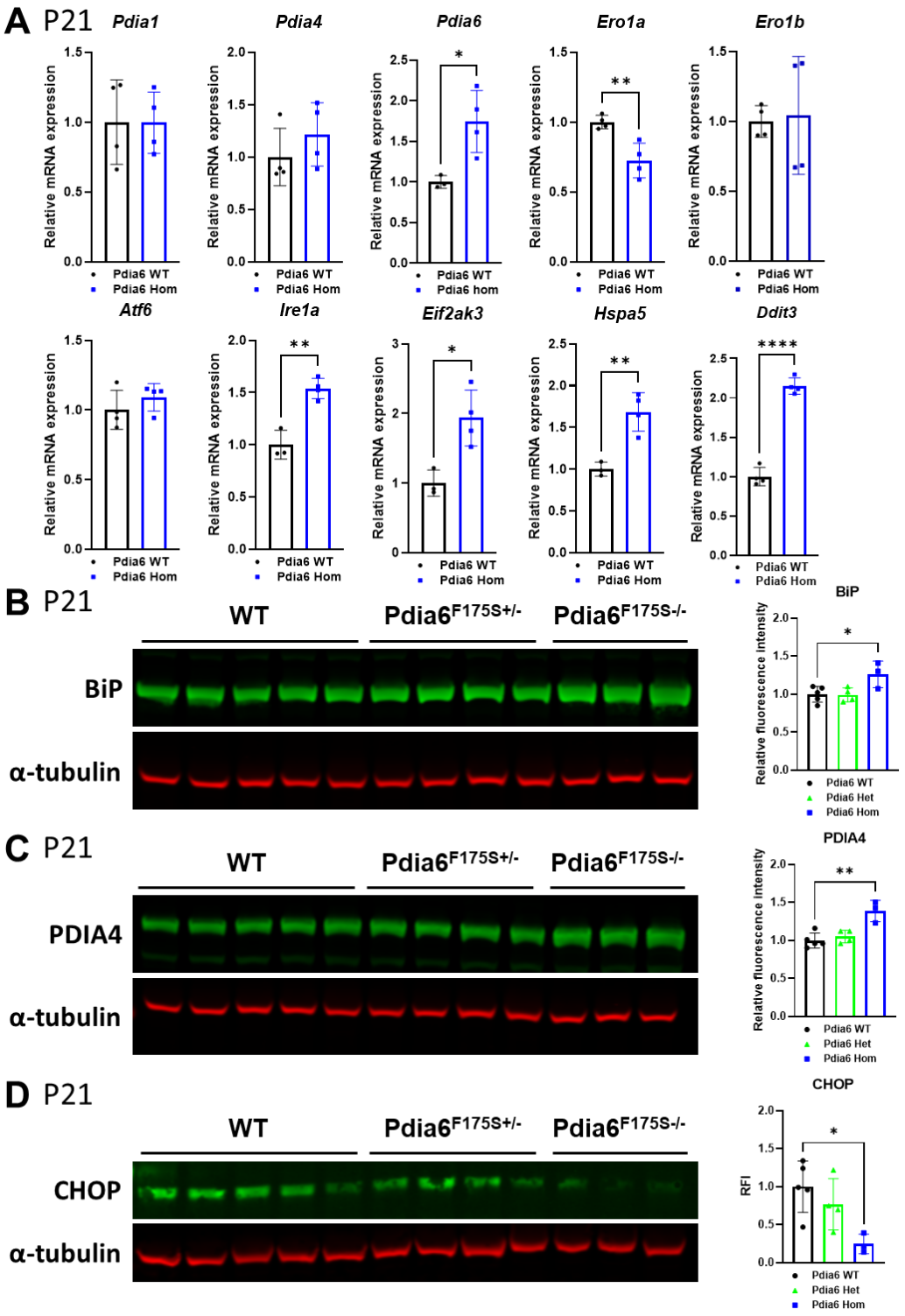

Figure 25 Modest ER-stress in Pdia6$^{F175S-/-}$ at P21

(A) Relative mRNA expression of *Pdia1*, *Pdia4*, *Pdia6*, *Ero1a*, *Ero1b*, *Atf6*, *Ire1a*, *Eif2ak3*, *Hspa5*, and *Ddit3*; n=3-4. **(B-D)** Western blot analyses and quantification of **(B)** BiP, **(C)** PDIA4 and **(D)** CHOP in pancreatic tissue; n=3-5. Mice at age P21 were used for all experiments. Parts of the figure are adapted from Chhabra and Amend et al. 2021.

4.2.6 Summary and conclusion for Pdia6^{F175S}

Mice with a homozygous point mutation in PDIA6 (F175S) occur in a reduced Mendelian ratio and show severe hyperglycemia shortly after weaning. Their body weight gain is reduced and they quickly develop severe hyperglycemia, accompanied by strongly reduced levels of proinsulin and insulin in islets and undetectable levels in plasma. A gene expression analysis revealed an increase in α-cell markers and a reduced expression of genes which are associated β-cell identity that further deteriorate with age. The occurrence of apoptosis could not be observed. Some signs of oxidative stress and ER-stress were already recognizable in 21-day old mutants with increased expression of PDIA4 and BiP.

In conclusion, it can be stated that the F175S point mutation in PDIA6 leads to hyperglycemia due to insulin deficiency and the loss of β-cell identity, which manifests itself in a disturbed redox milieu and mild ER-stress. Taken together, our study demonstrated that PDIA6 is required for the maintenance of β-cell identity, which was not previously recognized.

4.3 MODY1 caused by mutations in the *Hnf4a* gene: Characterization of several mouse models and gene therapy of Hnf4a-KI

The MODY1 project was part of an international collaboration aimed at identifying mouse models for various MODY genes that resemble a human phenotype and are suitable for gene therapy. Here, we collaborated with the group of Fatima Bosch from the Autonomous University of Barcelona (UAB) and with scientists around Steve Brown from the MRC in Harwell. The UAB team was working on MODY3 (causative gene *HNF1A*), the MRC team on MODY2 (causative gene: *GCK*) and our group on MODY1 (*HNF4A*).

We generated and phenotyped a variety of mouse models, which are briefly highlighted and performed gene therapy on one of the mouse models (Hnf4a-KI).

4.3.1 Hnf4a mouse models

Several mouse models with *Hnf4a* mutations were generated for MODY1, which results from mutations in the human *HNF4A* gene.

4.3.1.1 Hnf4a^{tm1b}

The IMPC (International Mouse Phenotyping Consortium) Hnf4a^{tm1b} mouse line was obtained from the EMMA mouse repository within INFRAFRONTIER (https://www.infrafrontier.eu/) and contains a lacZ tagged null allele of the *Hnf4a* gene, creating a full-body knock-out (KO) as described in [146]. Mice are commercially available under the official name of C57BL/6N-Hnf4a$^{tm1b(EUCOMM)Hmgu}$/Ieg. Wild types (Hnf4a$^{tm1b+/+}$) and heterozygous animals (Hnf4a$^{tm1b+/-}$) were analyzed for this work.

4.3.1.2 Hnf4a^{R333L} and Hnf4a^{G124A}

For Hnf4a^{R333L} and Hnf4a^{G124A}, the F1 archive from the Munich ENU mutagenesis screen [141] was searched for coding mutations in the *Hnf4a* gene that resemble human MODY1 mutations as found in the LOVD database (https://www.lovd.nl/3.0/home). The F1-archive consists of 16,800 DNA and corresponding sperm samples from individual F1-mutagenized mice on the C3HeB/FeJ genetic background, which was built by using the alkylating agent *N*-ethyl-*N*-nitrosourea (ENU) [147]. PCR fragments of about 250-300 base pairs were analyzed by high-resolution melting analysis using a LightScanner® instrument combined with a Plate-Butler System® [148]. Ten different mutations in *Hnf4a*

were identified (described in Supplementary Figure 13). After alignment of mouse and human genes, two mutations were selected: Hnf4a^{R333L}, where the arginine (basic polar, positively charged) at position 333 was exchanged by leucine (nonpolar, hydrophobic) (R333L, resembling the human R324L mutation) and Hnf4a^{G124A}, where the glycine (nonpolar, uncharged) at position 124 was exchanged by alanine (nonpolar, hydrophobic) (G124A, resembling the human G115A mutation). Both mutations were qualified as deleterious for the HNF4A protein by the PROVEAN tool (http://provean.jcvi.org/seq_submit.php). Therefore, the mutations R333L (c.998 G>T) and G124A (c.371 G>C) were selected to generate mice using the respective sperm samples for *in vitro* fertilization (IVF) followed by embryo transfer (performed by Susan Marschall, Helmholtz Zentrum München). After exome sequencing, additional mutations in the coding sequences resulting from ENU mutagenesis were identified. Animals were thoroughly genotyped after each generation until additional mutations were eliminated before the start of phenotyping experiments.

Hnf4a^{tm1b}, Hnf4a^{R333L} and Hnf4a^{G124A} were homozygous lethal, hence only heterozygous and wild type animals were analyzed.

4.3.1.3 Hnf4a$^{tm1b/R333L}$ and Hnf4a$^{tm1b/G124A}$

Additionally, we created hemizygous mouse lines to reduce on the one hand the *Hnf4a* gene dose (tm1b+/-) and on the other hand to introduce a point mutation. Therefore, Hnf4a$^{tm1b+/-}$ mice were bred with Hnf4a$^{R333L+/-}$ or Hnf4a$^{G124A+/-}$, respectively, to obtain hemizygous mice harboring one KO allele (tm1b$^{+/-}$) and one wild type (control animals) or one mutated allele (R333L or G124A), leading to the two novel mouse lines: Hnf4a$^{tm1b/R333L}$ and Hnf4a$^{tm1b/G124A}$.

4.3.1.4 Hnf4a-KI

Hnf4a-KI mice were generated in collaboration with Miquel Garcia from the laboratory of Fatima Bosch at the Autonomous University in Barcelona. A CRISPR-Cas9 mediated knock-in (KI) of a specific sequence into the 3' UTR of the *Hnf4a* gene is supposed to lead to an endogenous downregulation of *Hnf4a* specifically in β-cells. This novel technique for downregulation of genes by KI of specific sequences was filed on January 25th, 2021 as an initial priority application at the European Patent office (EP21382080)

together with our collaborators from Barcelona. Details concerning the KI or guide RNA sequences are specified in EP21382080 and not yet available to the public. The KI strategy is shown in Figure 26. CRISPR-Cas9 gene editing, pronucleus-injections and subsequent embryo transfer to create the mouse line was performed by Florian Giesert (Helmholtz Zentrum München). Animals were genotyped as described in 3.2.3. An additional restriction digest using EcoRV was done to confirm the genotypes because this restriction site was added to the KI sequence. For this mouse line, mice homozygous for the KI and the wild-type allele were analyzed.

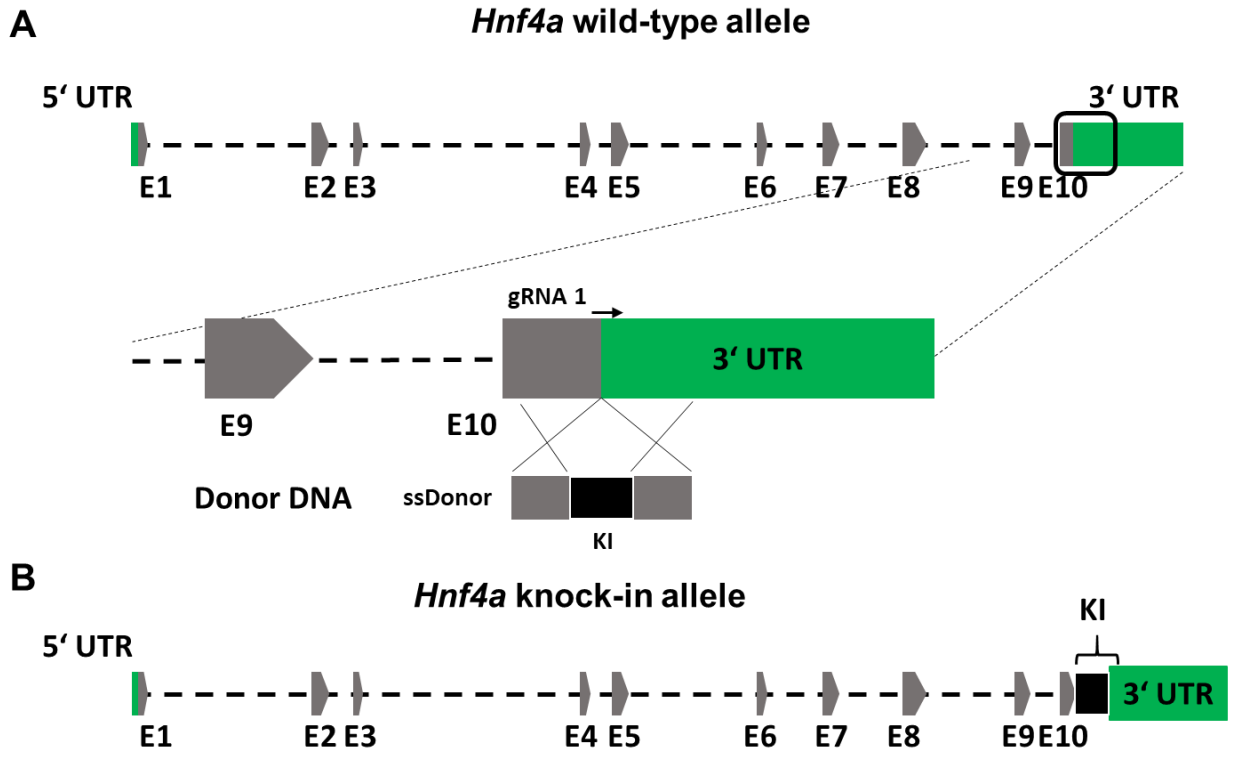

Figure 26 Downregulation of Hnf4a by KI of a sequence between exon 10 and the 3’ UTR

(A) The upper panel shows the intron/exon (E) structure of the wild-type *Hnf4a* gene (structure obtained from ENSEMBL (ENSMUST00000018094.13). The bottom panel illustrates the CRISPR/Cas9 strategy to generate the sequence-specific knock-in (KI). A single guided RNA (gRNA 1) was designed to target between exon 10 and the 3’ UTR of the *Hnf4a* gene to introduce the sequence (donor DNA) by homology directed repair (HDR).

(B) Resultant *Hnf4a* KI allele.

4.3.2 **Hnf4a-KO animals do not show hyperglycemia**

The first step to identify a suitable mouse model for gene therapy was to phenotype the Hnf4a-KO animal model Hnf4a^{tm1b}. Since it was previously shown that homozygous Hnf4a-KO animals are not viable due to homozygous lethality at E6.5 [105], and we also did not observe any homozygous animals, we analyzed wild-type (Hnf4a$^{tm1b+/+}$) and heterozygous (Hnf4a$^{tm1b+/-}$) animals according to the protocol for hypothesis-driven phenotyping for glucose metabolism from the German Mouse Clinic (GMC; http://www.mouseclinic.de/research/gmc-pipelines/hypothesis-driven-pipelines/index.html). However, we did not observe any differences between male and female Hnf4a$^{tm1b+/-}$ animals and their wild-type littermates in both body weight development and regular glucose monitoring (Figure 27A-B'). Furthermore, no differences between mutants and wild type were detected in glucose- and insulin tolerance tests (Figure 27C-C').

Compared with wild type animals, KO animals only have one functional allele, so we expected correspondingly less HNF4A protein. However, when we checked the expression of HNF4A protein in the liver, where HNF4A is highly expressed, to our surprise, we could not detect any change in heterozygous animals compared with wild types (Figure 27D). Consistent with this result, we also did not detect any change in gene expression of *Hnf4a* in isolated islets (Figure 27E).

HNF4A is essential for β-cell function and maintaining glucose homeostasis by controlling insulin secretion [149]. We therefore analyzed gene expression of its main interactor *Hnf1a* [150] and some other genes related to β-cell function (*Ins2*, *Ucn3*, *Slc2a2*) and insulin secretion (*Kcnj11*, *Abcc8*) in isolated islets. None of these genes were found to be differentially expressed (Figure 27E).

Also, 6 weeks of high-fat diet (HFD) did not result in differences in body weight, body weight gain or blood glucose between groups (Supplementary Figure 12).

From these data, it can be concluded that the presence of one null allele does not lead to any molecular perturbations such as downregulation of the *Hnf4a* gene or its protein. In line with these observations, we did not observe any manifestation of a phenotype. Heterozygous Hnf4a-KO animals are not a suitable mouse model for MODY1.

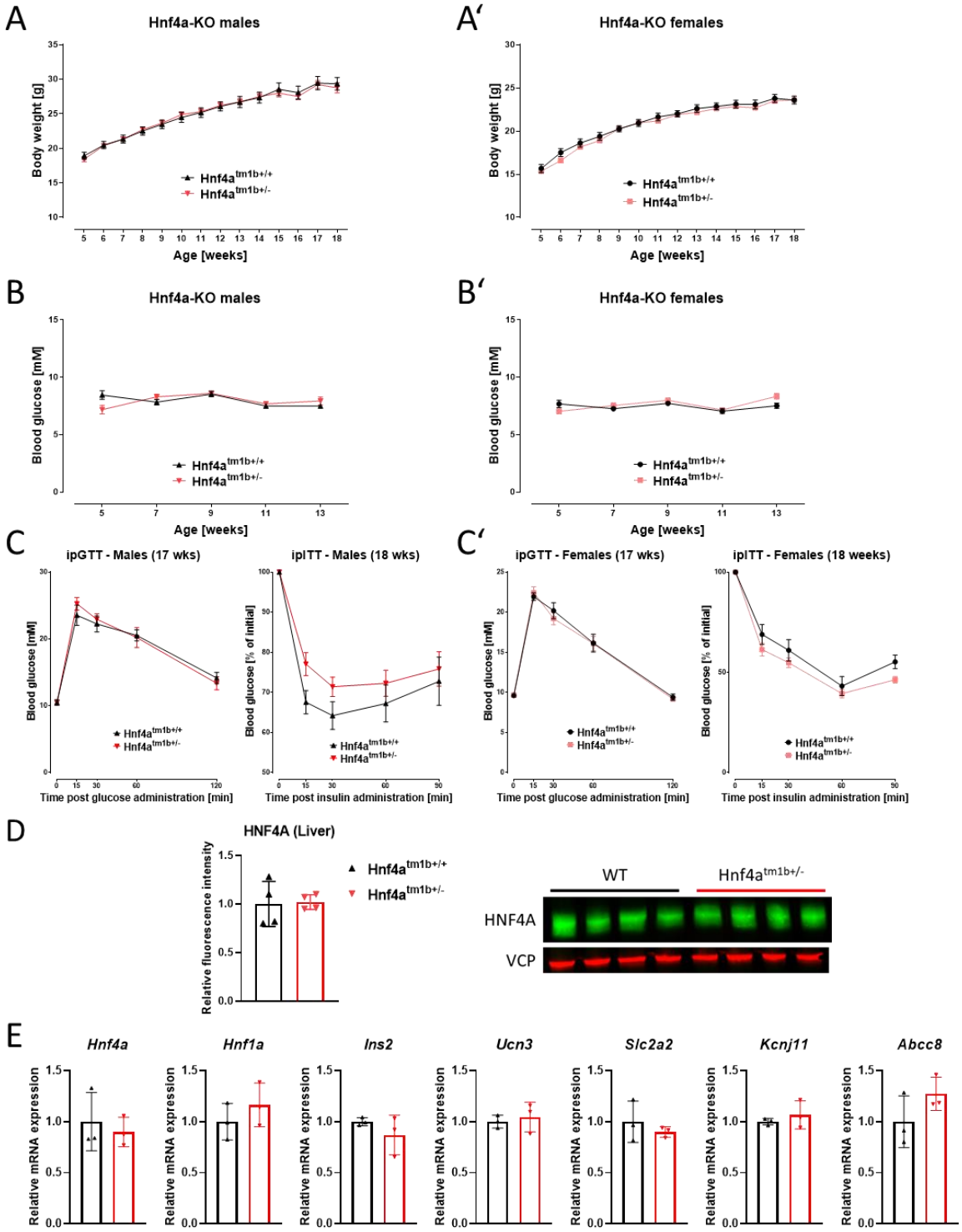

Figure 27 In vivo and in vitro phenotyping of Hnf4a-KO mice

(A-A') Body weight [g] in *ad libitum* fed males and females, n=11-15. **(B-B')** Blood glucose [mM] from *ad libitum* fed males and females, n=11-15. **(C-C')** ipGTT (2g/Kg BW) and ipITT (0.75U/kg BW) in 17- and 18-week-old males and females; n=11-15. **(D)** Western blot analysis and quantification of HNF4A in liver tissue from 12- and 25-week-old males. **(E)** Relative mRNA expression of *Hnf4a*, *Hnf1a*, *Ins2*, *Ucn3*, *Slc2a2*, *Kcnj11* and *Abcc8* in islets of 12-week-old males; n=3-4; black = Hnf4a$^{tm1b+/+}$ (WT); red = Hnf4a$^{tm1b+/-}$.

4.3.3 **Hnf4a^{R333L} and Hnf4a^{G124A} animals do not show hyperglycemia**

As the MODY1 phenotype in humans does not result from a knockout of the *HNF4A* gene but rather from point mutations, spontaneous or inherited, we aimed to identify mouse models with point mutations in the *Hnf4a* gene. We screened our F1 archive from the Munich ENU archive as described in 4.3.1.2 and performed *in vivo* and *in vitro* phenotyping of our models Hnf4a^{R333L} and Hnf4a^{G124}. According to preceding data base research, both mutations were described as deleterious by the PROVEAN tool.

After heterozygous intercrosses, we could not observe any homozygous offspring and propose homozygous lethality similar to Hnf4a-KO mice (4.3.2). Therefore, we have only analyzed heterozygous Hnf4a$^{R333L+/-}$ and Hnf4a$^{G124A+/-}$ mice together with their respective wild type littermates (+/+).

During the *in vivo* observations, we did not observe any changes of bodyweight in mutants of both models (Figure 28A-A'), which is similar to the Hnf4a-KO. We bi-weekly investigated urine non-invasively, for signs of elevated blood glucose levels and did not observe any differences between the groups. When the animals were sacrificed at the age of 12 weeks, we also observed no changes in fasting blood glucose levels (Figure 28B-B') in all animals. Finally, we did not find any changes in HNF4A protein expression in liver tissue in all animals.

We conclude, that both heterozygous Hnf4a^{R333L} and Hnf4a^{G124} animals do not develop hyperglycemia and are therefore not suitable mouse models for MODY1.

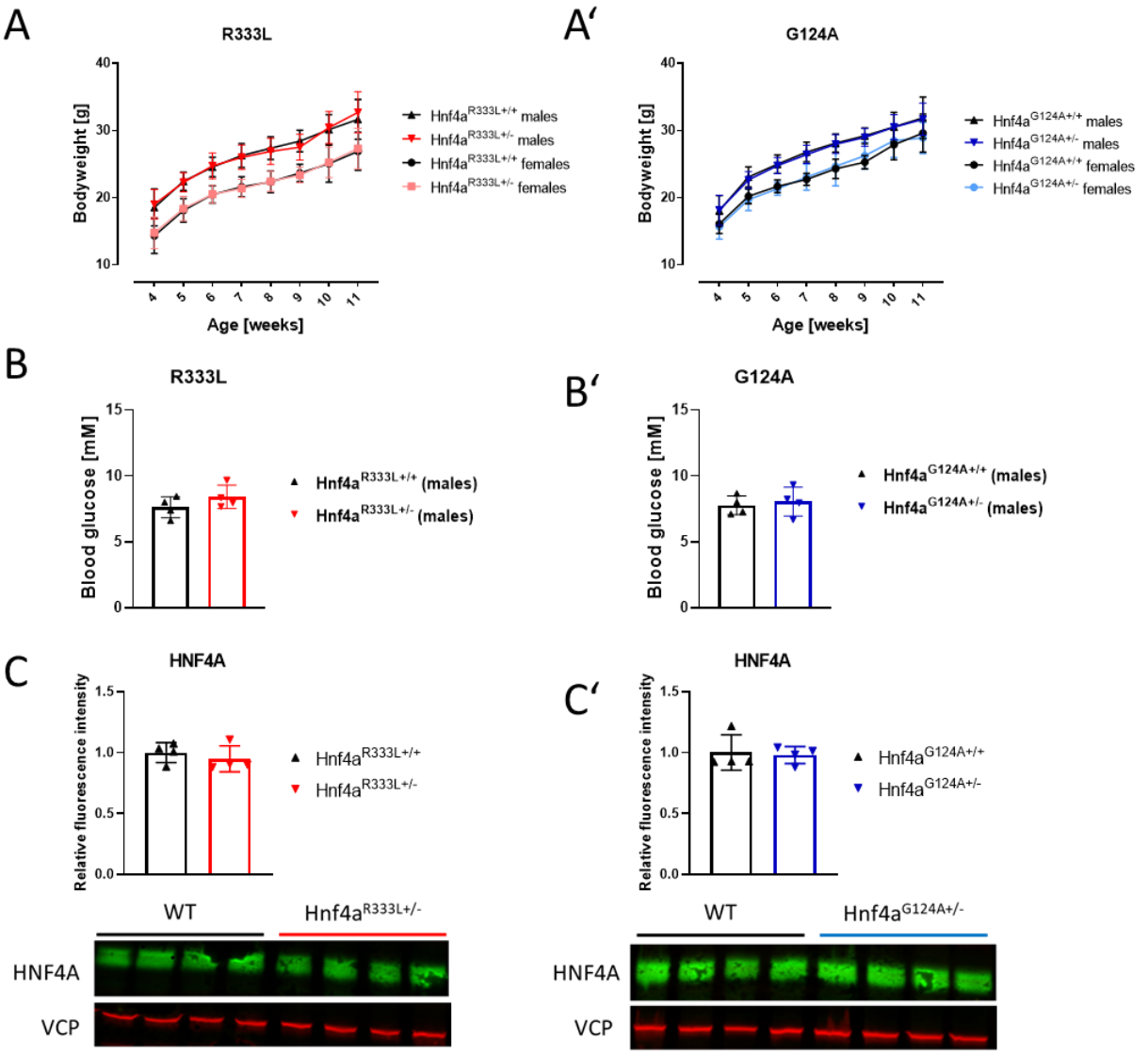

Figure 28 No hyperglycemia in Hnf4a^{R333L} and Hnf4a^{G124A} animals

(A-A') Body weight [g] in *ad libitum* fed males and females; n=10-12. **(B-B')** Fasting (6h) blood glucose in [mM] in males at the age of 12 weeks, n=4 for each genotype. **(C-C')** Western blot analysis and quantification of HNF4A in liver tissue from 12-week-old males; n=4 for each genotype.

4.3.4 Hemizygous Hnf4a$^{tm1b/R333L}$ and Hnf4a$^{tm1b/G124A}$ do not show hyperglycemia

Since neither Hnf4a-KO nor Hnf4a^{R333L} or Hnf4a^{G124A} animals showed any phenotype and we could not observe any reduction of HNF4A protein in individual heterozygotes, we aimed to reduce the *Hnf4a* gene dose by performing Hnf4a-KO×Hnf4a^{R333L} and Hnf4a-KO×Hnf4a^{G124A} intercrosses to generate hemizygous animals. Analyses were performed on animals that harbor one KO allele (tm1b) to reduce theoretically the gene dose to 50% and, an allele that contains one of the individual point mutations (R333L or G124A). Littermates containing one wild-type (+) and one KO-allele (tm1b) served as controls.

Until the age of 14-15 weeks, where several animals were sacrificed for further analyses, no differences between hemizygous mice and wild-type littermates of both lines in body weight development and random blood glucose levels were observed (data not shown). Therefore, smaller cohorts of both lines were further analyzed until the age of 30 weeks. In these cases, due to the low number of animals, males and females were grouped and analyzed together.

However, also at the age of 30 weeks no differences in body weight or fasted blood glucose could be observed (Figure 29A-A'). Interestingly, we observed high plasma insulin levels in all animals regardless of the genotype, which can possibly be attributed to the age of the animals (Figure 29B-B'). Finally, we analyzed HNF4A protein expression in liver tissue but also did not find any differences (Figure 29C-C').

We conclude, that also the creation of hemizygous animals did not result in the manifestation of any phenotype. The downregulation of HNF4A in a whole-body concept appears to be difficult. To study HNF4A in the context of the pancreas and diabetes, other methods seem to be necessary. One possibility is to specifically reduce *Hnf4a* gene dose only in the pancreas without affecting the whole body.

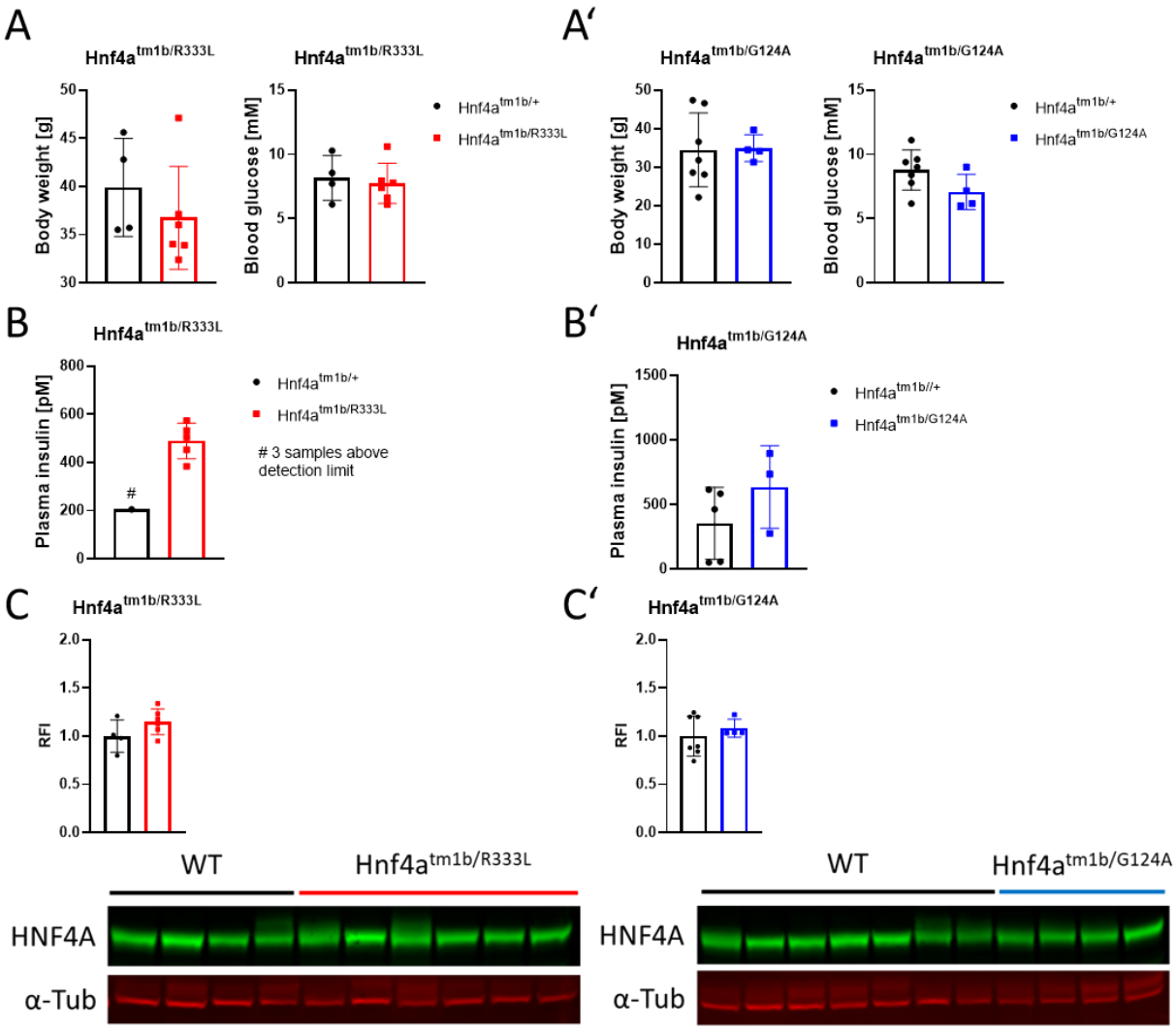

Figure 29 No hyperglycemia in Hnf4a$^{tm1b/R333L}$ and Hnf4a$^{tm1b/G124A}$

(A-A') Body weight in [g] and blood glucose in [mM] in fasted (6h) animals, n=4-7, age: 30 weeks. **(B-B')** Fasting (6h) plasma insulin in [pM], # 3 samples above detection limit; n=1-6, age: 30 weeks. **(C-C')** Western blot analysis and quantification of HNF4A in liver tissue from 30 weeks old animals; n=4-7.

4.3.5 **Hnf4a-KI do not show hyperglycemia**

We therefore analyzed in a next step a mouse model with a targeted downregulation of *Hnf4a* only in β-cells, which we achieved by the knock-in (KI) of a specific sequence in the 3'UTR of *Hnf4a* as described in 4.3.1.4. All mice were phenotyped according to the pipeline described in 3.2.4.2, starting from the age of 6 weeks until the age of 24 weeks. We did not observe any changes in body weight (Figure 30A-A') or in blood glucose between homozygous KI-animals and wild-type littermates (Figure 30B-B'). In addition, we performed glucose- and insulin tolerance tests at two times points to trace changes over time. However, we did not find any difference in glucose tolerance (Figure 30C-C') or insulin tolerance (Figure 30D-D') between groups. We only observed mild deterioration of insulin tolerance by week 22, which is normal during ageing [151].

Since we did not observe a phenotype even though it was shown that *Hnf4a* deficiency in the pancreas caused abnormal insulin secretion in mice [149] and that HNF4A regulates the expression of genes associated with glucose metabolism [103], we first checked in pancreatic islets of 12-14 week-old animals whether we actually observe decreased *Hnf4a* expression as intended. In addition, we analyzed the expression of HNF4A-associated genes. Indeed, the KI of a specific sequence into the 3' UTR did lead to downregulation of *Hnf4a* compared to wild types as shown with two different primer pairs. However, the decreased expression of *Hnf4a* did not lead to altered expression of *Hnf1a*, which is one main interactor [150] (Figure 31A). Also, other prominent islet genes like *Ins2*, *Ucn3* and *Gcg* were not dysregulated. Interestingly, *Slc2a2* expression, encoding for GLUT2, was downregulated while the expression of *Sst* (encoding for somatostatin) was upregulated (Figure 31B).

After final sacrifice, protein was isolated from the liver to observe whether an off-target effect happened that led to downregulation in the liver. In males, we did not observe any significant differences between the groups. In females, we observed a mild but significant upregulation of HNF4A (Figure 31C).

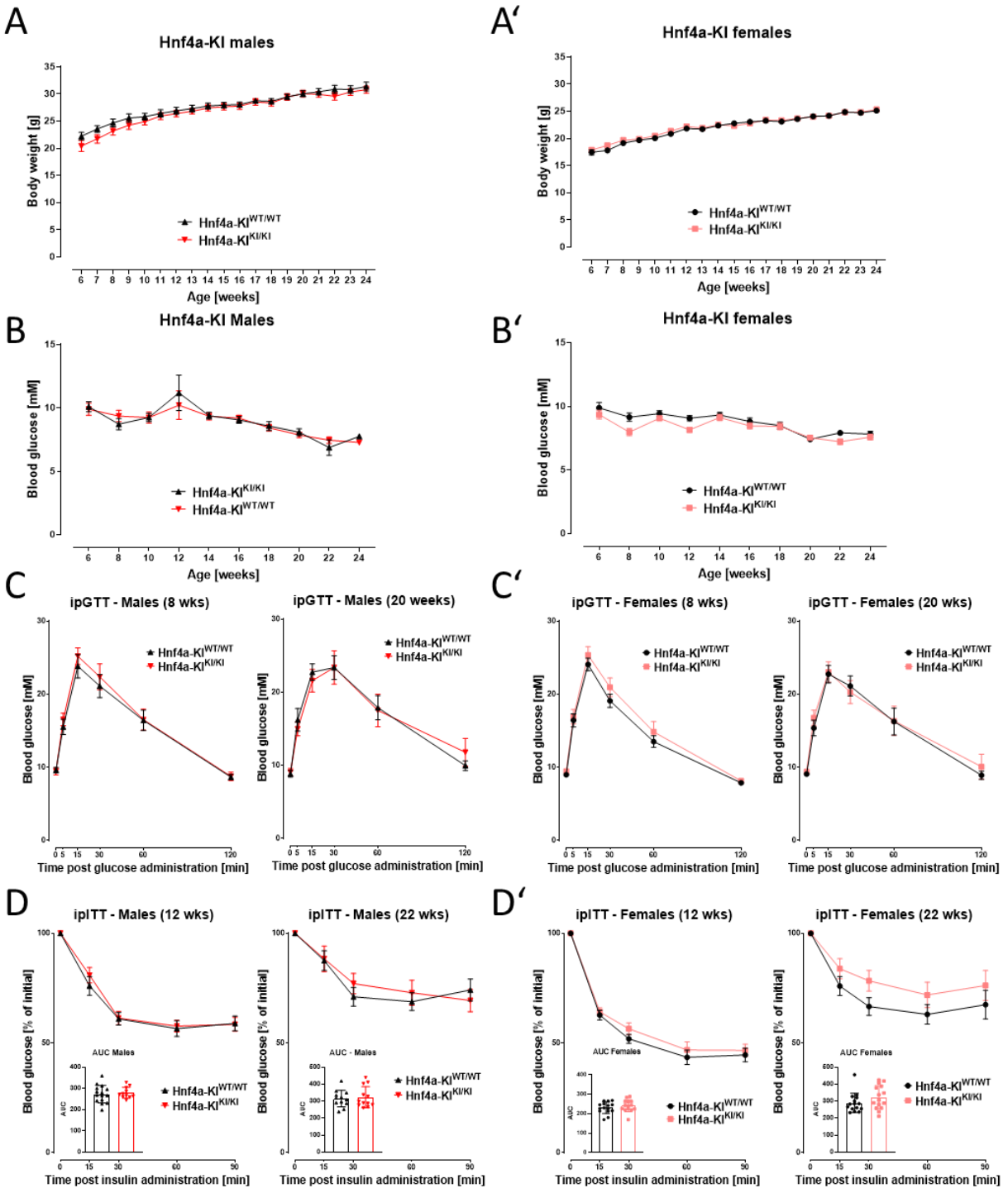

Figure 30 No hyperglycemia in homozygous Hnf4a-KI animals

(A-A') Body weight [g] in *ad libitum* fed males and females, n=13-15. **(B-B')** Blood glucose [mM] in *ad libitum* fed males and females, n=13-15. **(C-C')** ipGTT (2g/kg BW) in 8- and 20-week-old males and females; n=11-15. **(D-D')** ipITT (0.75U/kg BW) in 12- and 22-week-old males and females; n=11-15 per genotype.

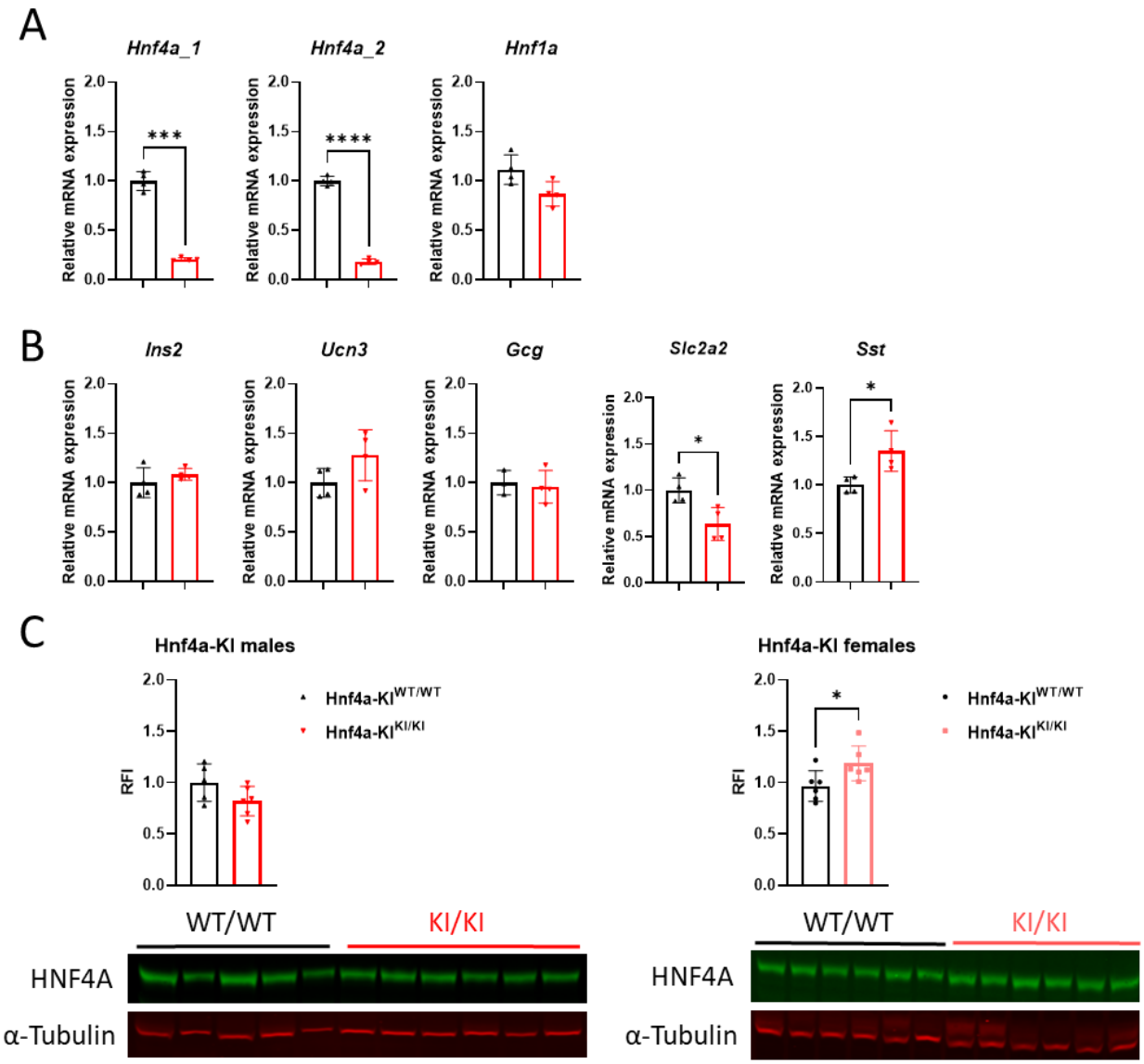

Figure 31 Gene expression analysis in islets and HNF4A expression in the liver of Hnf4a-KI animals

(A) Relative mRNA expression of *Hnf4a* (two different primer pairs) and *Hnf1a* in islets of 14-16-week-old male animals; n=3-4. **(B)** Relative mRNA expression of *Ins2*, *Ucn3*, *Gcg*, *Slc2a2* and *Sst* in islets of 14-16-week-old males; n=3-4. **(C)** Western blot analysis and quantification of HNF4A in liver tissue from 24-week-old males; n=5-6 per genotype.

4.3.6 **Gene therapy in Hnf4a-KI**

Since, as intended, we observed a specific downregulation of *Hnf4a* in islets of Hnf4a-KI animals and suspected that this leads to a diabetic phenotype, we decided to perform gene therapy in these animals to check whether *Hnf4a* expression can be rescued.

4.3.6.1 Method establishment for in vivo AAV-vector delivery

The local delivery of gene vectors directly to the pancreas reduces systemic exposure to the vector, which in turn leads to increased safety of gene transfer. Intraductal injections were performed as described by Loiler et al. in 2005 [134] with some modifications. This method is commonly used by our collaborators of the laboratory of Fatima Bosch at the Autonomous University (UAB) [126, 135]. After intense training at the Barcelona facility, we optimized the protocol to adapt to local circumstances and recent discoveries.

Animals were separated into 2 groups: control group and treatment group. The control group was injected with 200 µL of PBS solution (Table 18). For the treatment group, rAAV8 vectors (5×10^{11} viral genomes (vg)) were diluted in 200 µL of the same buffer. As determined by our collaborators at UAB, one dose containing 5×10^{11} vg is sufficient to transduce most of the β-cells.

To ensure maximum possible sterility throughout the procedure, all appliances and the area used for surgery were cleaned extensively and disinfected before the start of the procedure. All surgical tools that were used were heat-sterilized before surgery and between individual animals. The surgeon always took care to wear fresh sterile gloves and to keep touching of appliances to a minimum.

To prepare for surgery, AAV vectors were thawed on ice and heating pads were warmed. Mice where anesthetized by *ip* injection with 100 mg/kg Ketamine and 10 mg/kg Xylazine (diluted in sterile 0.9% NaCl). Once immobile, mice were placed on the heating pads. Eye cream (Bepanthen) was applied to keep the eyes wet, then animals were injected *s.c.* with 0.1 mg/kg Buprenorphin (diluted in 0.9% sterile NaCl) to provide appropriate analgesia. Once mice had reached deep anesthesia (surgical tolerance), the abdominal area was shaved and disinfected by applying 70% EtOH (Figure 32A). The abdominal cavity was opened by a ventral midline incision using blunt scissors to avoid organ injury:

first the skin was opened, then the muscular layer, following the *linea alba* approximately 1 cm down from the xyphoid process (Figure 32B).

A colibri retractor (FST 17000) was inserted to keep the abdominal cavity open (Figure 32C). The mouse was placed with the anterior end of the animal facing towards the surgeon under a stereomicroscope equipped with a ring light and a small heating pad. To expose the duodenum where the common bile duct is attached, a blunt, shovel-like tool was used to lift up the liver, then the intestine was pulled down carefully using a ring forceps (FST 11103-09) until the common bile duct was exposed (Figure 32D).

To ensure vision of the duct, two small paper balls soaked in sterile saline were placed on either side of the duct to displace the liver lobes laterally (Figure 32E). A microclamp (FST 18055-04) was placed on the bile duct caudally to the liver using a forceps applicator (FST 18057-14) to avoid loss of injection solution to the liver (Figure 32F). A syringe with a 30G needle was inserted through the papilla of Vater into the common bile duct and carefully advanced retrogradely through the duct (Figure 32G). The needle was secured in place by a surgical assistant carefully placing a second microclamp (FST 18055-02) in the middle of the needle, thereby clamping the needle, the duct and the intestine (Figure 32H). A volume of 200 µL (PBS or vector solution) was carefully and slowly injected into the duct within approximately 1 minute (Figure 32I). After another minute, the second microclamp was carefully removed by the surgical assistant and the needle was slowly pulled out. The injection site was carefully dried, then one drop of veterinary glue (Histoacryl) was applied to cover the hole made by the syringe and allowed to dry (~10 sec). Afterwards, the remaining microclamp and the paper balls were carefully removed from the abdominal cavity. A few drops of saline were added before removing the retractor. The mice were then transferred from the stereomicroscope to the heating pad (Figure 32J). The muscular layer and the skin were sutured with a two-layer approach using absorbable suture (Chirlac) (Figure 32K-L). Mice were left on the heating pad to recover and wake up from anesthesia. To reduce stress levels, mice were moved to individual cages. Mice were carefully watched for the following 7 days and scored according to the animal welfare guidelines. The following 3 days, sutures were checked. If the sutures were open, animals were anesthetized shortly using isoflurane to re-suture.

In the following 3 days, animals were closely monitored and received 5 mg/kg Melosus solution (Meloxicam) twice a day to ensure continuous analgesia. The animals were allowed to recover from surgery for 4 weeks before further experiments were performed. After one week, feces and urine were collected and nucleic acids were isolated to ensure that the animals did not shed viral nucleic acids.

Figure 32 Microsurgical procedure for intraductal AAV administration

(A) Shaved and disinfected abdomen. **(B)** Incisions: Skin layer, muscular layer. **(C)** Insertion of a colibri retractor. **(D)** Exposing the injection site. **(E)** Placement of small paper balls. **(F)** Placement of the first microclamp with clamp applicator. **(G)** Insertion of the needle into the common bile duct. **(H)** Placement of the second microclamp (by surgical assistant). **(I)** Close up of the intraductal injection (blue color used for demonstration purposes). **(J)** Suturing procedure. **(K)** Suture of the muscular layer. **(L)** Suture of the skin (Images taken by Maximilian Schmidtke, surgeon: Anna-Lena Amend).

4.3.6.2 In vivo vector delivery in Hnf4a-KI

Surgery for intraductal delivery of the gene therapy vector (Figure 10) was performed with male animals aged 8 weeks as described in detail in 4.3.6.1. Within the scope of this thesis, gene therapy was performed on one control group (wild type injected with control solution) and one treatment group (homozygous KI injected with vector solution). Future studies will include a second control group (homozygous KI injected with control solution), which has not yet had surgery due to experimental limitations and delays in material delivery during and after the COVID-19 pandemic. For the same reasons, the *in vivo* follow-up examination was not yet completed at the time this thesis was written (the plan is to sacrifice the animals at 30 weeks of age). Therefore, the remaining experiments and follow-up studies have been handed over to the succeeding doctoral researchers Aliona Harten and Maximilian Schmidtke.

Animals injected with either vector solution or control solution were allowed to recover for 4 weeks from surgery before undergoing phenotyping experiments as described in 3.2.4.2. During the course of the follow-up study, to this date, animals did not show any changes in body weight or blood glucose levels (Figure 33A-B). Glucose tolerance was not significantly altered at the two time points 14 weeks and 26 weeks (Figure 33C). Also, insulin tolerance was found to be unchanged at the two time points 18 weeks and 28 weeks (Figure 24, D). These findings suggest that the treatment with the vector so far has no abnormal side effects on glucose-associated metabolism.

Considering laboratory safety, handling and injection of substances containing viral particles, we aimed to check whether animals shed viral nucleic acids in feces and urine one week post-surgery. These experiments were carried out by Maximilian Schmidtke, but are added to this thesis in order to demonstrate the safety of the method with regard to potential future human patients of such a therapy with rAAV8 vectors. One week after surgery, we isolated viral nucleic acids from urine and feces and performed a PCR analysis and subsequent gel electrophoresis. We could not observe any viral nucleic acids in both urine and feces in all animals. As a positive control, viral nucleic acids were isolated from vector solution and diluted 1:10. The result clearly demonstrated the absence of viral nucleic acids in urine and feces of vector-treated animals (Figure 33E).

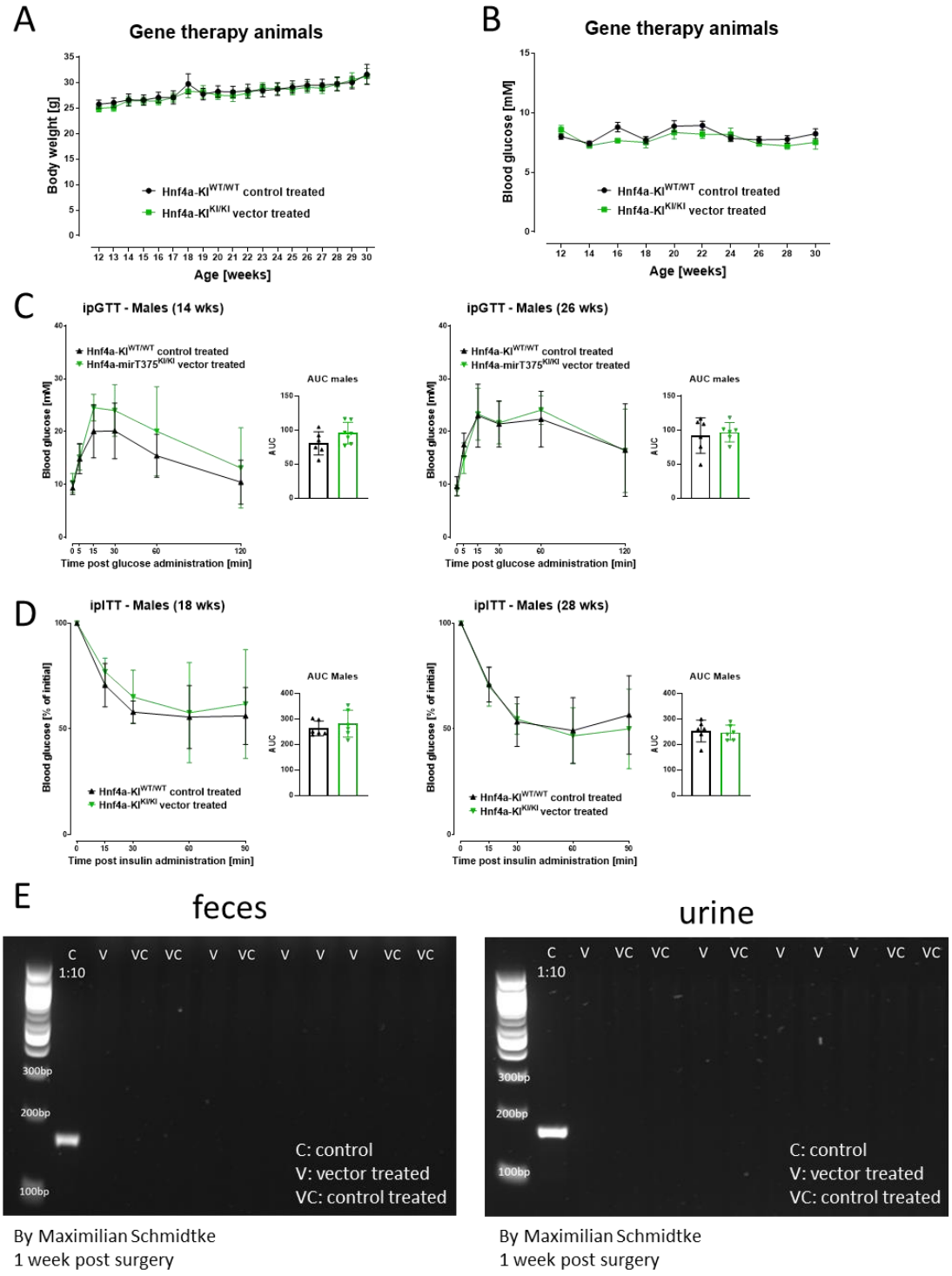

Figure 33 Follow up after gene therapy treatment in Hnf4a-KI

(A-A') Body weight [g] in *ad libitum* fed male animals, n=6-7. **(B-B')** Blood glucose [mM] from *ad libitum* fed male animals, n=6-7 per treatment. **(C-C')** ipGTT (2g/kg BW) in 14- and 26-week-old male animals; n=6-7 per treatment. **(D-D')** ipITT (0.75U/kg BW) in 18- and 28-week-old male animals; n=6-7 per treatment. **(E)** Viral nucleic acids in feces and urine samples from vector (V) and control-treated (CV) animals, n=5 per treatment + control (1:10-dilution).

4.3.7 **Summary and conclusion for the MODY1 project**

Identifying a mouse model that reflects the human MODY1 phenotype has proven to be difficult. None of the mouse models included in this thesis presented phenotypical alterations. All mutants were macroscopically indistinguishable from wild-type littermates. Against our expectations, the models Hnf4a-KO, Hnf4a^{R333L}, Hnf4a^{G124A}, Hnf4a$^{tm1b/R333L}$ and Hnf4a$^{tm1b/G124A}$ did not show any signs of reduced HNF4A activity, which might be the reason for a missing phenotype. Further analysis is necessary to decipher why we do not observe a phenotype, although animals are heterozygous KO animals and point mutations were predicted to be deleterious.

Only in Hnf4a-KI, where *Hnf4a* was supposed to be specifically downregulated only in β-cells, we actually observed downregulation of *Hnf4a*, albeit without a concomitant phenotype. Hence, this mouse model offers an interesting subject to study why we do not observe a phenotype although we observe an extreme downregulation of *Hnf4a*.

To date, there is no *Hnf4a* mouse model that meets the criteria of hyperglycemia, but the Hnf4a-KI model lost most of its *Hnf4a* transcripts in β-cells. However, as evidence of the concept that gene therapy treatment with a healthy *Hnf4a* copy can rescue *Hnf4a* gene expression in β-cells, we treated homozygous Hnf4a-KI mice with rAAV8. To this date, follow-up studies are still in progress. So far, we have not observed any negative side effects of the treatment and no shedding of viral particles.

5. Discussion

5.1 Differences between mouse strains in metabolic research

When considering phenotypic variations, such as in our case, changes in metabolism due to point mutations, knock-out or knock-in alleles, it must be taken into account that different inbred mouse strains inherently have a different metabolic phenotype and are not always comparable with one another (see also Kollmus et al. 2020 [152] and references therein). For example, it has been shown that C3HeB/FeJ animals gain body mass faster, consume more food and generally have higher blood glucose levels compared to three other strains [153]. It has even been shown, that there are differences between the different C57BL/6 substrains C57BL/6N and C57BL/6J [154]. The mouse models used in this work are based of different inbred mouse strains: The two *Ins2* and the *Pdia6* models, are based on the mouse strain C3HeB/FeJ, while the *Hnf4a* models are based on C57BL/6N, C3HeB/FeJ or on hybrid strains (C3H/C57).

5.2 The two novel mouse models Ins2^{C109G} and Ins2^{V26D}

In this work, two new *Ins2*-mutant mouse models were described for the first time: Ins2^{C109G}, the first mouse model in which a point mutation at C109 leads to the loss of the cysteine and consequently to the loss of the A20-B19 disulfide bridge, and Ins2^{V26D}, the first mouse model with a point mutation at position B2.

5.2.1 Severe diabetes and changed insulin sensitivity in male *Ins2* mutants

In both models, male animals exhibited severe, early-onset diabetes with hyperglycemia and hypoinsulinemia, while females were only mildly affected. Therefore, we excluded female animals from some experiments in this study, but performed others to assess similarities and differences with male animals. Sexual dimorphism in mice is discussed further below (5.2.7).

Like Ins2^{V26D} mice, KINGS mice harbor a non-cysteine mutation at G32 and male mice became diabetic around 5 weeks of age [91]. However, hyperglycemia in Ins2^{V26D} mice was much more pronounced with blood glucose levels climbing up to around 30 mM and even insulin being undetectable in the majority of animals by 16 weeks of age. Surprisingly, the increase in glycemia was more pronounced in Ins2^{V26D} compared to

Ins2^{C109G} and also to KINGS mice [91], however this could also be partly due to strain-specific differences between C3HeB/FeJ and C57BL/6J (KINGS mice) [153].

Ins2^{C109G} animals also showed high blood glucose levels from an early age, yet 25 mM were never reached and insulin was detected in most animals at all time points analyzed. Since the blood sugar levels in mutants of both lines were already very high, we decided not to carry out GTTs for animal welfare reasons. When we analyzed the insulin sensitivity, we observed normal deterioration with age in wild types of both models [155]. However, the mutants showed opposite effects to each other. Ins2^{C109G} mutants retained better insulin sensitivity at 20 weeks compared to wild-type littermates, an effect also observed in Akita mice [156]. On the other hand, in Ins2^{V26D}, the effect was reversed and the response to insulin was more blunted compared to wild types. This is similar to patients of T1DM, who also have reduced insulin sensitivity [157]. These findings are particularly interesting when one looks at a study by Liu et al. [158] who showed that misfolded Akita proinsulin abnormally interacted with the insulin receptor and consequently resulted in decreased insulin signaling within the β-cells. Therefore, other misfolded molecules could elicit different responses.

It is therefore conceivable that, as with Akita (C96Y [158]), insulin with mutations on the cysteines such as C109 or C95 (e.g. in Munich*Ins2* [90]) binds abnormally or not at all to the receptors. In addition, since only small amounts of functional insulin are present in the blood stream, the receptors are hypersensitive, so that when functional insulin is administered, the reaction is intensified, even more so with increasing age. In contrast, the Ins2^{V26D} mutation appears to induce a more T2DM-like phenotype with insulin resistance. Because of a potentially new specific conformation, V26D-mutant molecules might be able to bind to the receptor, but fail to elicit a response, leading to animals becoming insulin resistant over time. To confirm this hypothesis, receptor binding assays as described in [159] could be performed in future experiments.

Taken together, these results indicate that both the exact positions and the amino acid substitutions are important and must be considered when assessing the phenotype. Also, the different age-related changes in insulin sensitivity, if observed in humans, could provide clues for a better treatment regime.

5.2.2 Disturbed folding of proinsulin and subsequent swelling of the ER

It is proposed that the A20-B19 bridge forms as the first of the three disulfide bonds and acts as a specific folding nucleus for the ripening insulin molecule [160]. Therefore, loss of the A20-B19 bond in $Ins2^{C109G}$ can lead to the destabilization of the molecule. In $Ins2^{V26D}$, the exchange of the hydrophobic valine at position 26 to aspartic acid lies in the first segment of the B-chain (B1-6), which has been reported to be important in promoting foldability [36, 41]. Therefore, this change in charge of the amino acid may disrupt proper folding.

Previous studies have shown that in MIDY high-molecular weight (HMW) complexes containing mutant and wild-type proinsulin accumulate in the ER and hinder healthy insulin from exiting [39]. Indeed, we observed a severely dilated ER in both our mutants. This was surprising in $Ins2^{V26D}$, because we expected a less severe phenotype resembling more KINGS mice, where only a modest retention of G32S proinsulin was observed [91]. Interestingly, the overall $Ins2^{V26D}$ phenotype appears to be more pronounced, further demonstrating that the type and position of a mutation do matter.

In both mutants, calreticulin, a soluble ER marker and chaperone [161], appeared displaced and did not co-localize with proinsulin as in the wild types. Calreticulin has been shown *in vitro* to aid in dissolving proinsulin aggregates during oxidative stress, leading to proinsulin being proposed as a new candidate for its chaperone function [162]. We hypothesize that mutant proinsulin interferes with calreticulin binding, further exacerbating the dilation of the ER and adding to oxidative stress. Additional immunohistochemistry with calnexin, an integral ER membrane chaperone that acts in concert with calreticulin [161], revealed a lower density in mutants. In the case of a distended ER, in which membranes are not ad densely packed as normally the case, we expected that an integral ER membrane protein would be less densely packed than in wild types, in which membranes are physically closer together. We thus confirmed the observation from TEM images and were able to reassure the above-mentioned hypothesis. The next step crucial step is the transport of proteins from the ER to the Golgi apparatus for sorting and distribution within the cell [163]. Within the β-cells, there was no difference in the localization of the Golgi marker GRASP65 between mutants and wild

types, indicating that the Golgi apparatus was not affected by the severe dilation of the ER. Additionally, proinsulin showed co-localization with GRASP65 in both wild types and mutants, indicating normal transport of those proteins that manage to exit the ER to the Golgi (Supplementary Figure 7).

Aside from misfolding, healthy or mutant proinsulin molecules must be processed to mature insulin to obtain biological function. In T1DM diagnosed at a very young age, strong co-localization of proinsulin and insulin was associated with impaired proinsulin processing [143]. Since we did not observe such co-localization in our *Ins2* models and the INS/PROINS ratio remained similar between mutants and wild types, the general processing of available proinsulin itself, independent of potential misfolding, does not appear to be disturbed.

5.2.3 **β-cell dysfunction and β-cell identity in our *Ins2* models**

Several factors potentially contribute to β-cell dysfunction in our models, e.g. altered gene expression of *Ins2* due to individual mutations, oxidative stress due to insulin misfolding or glucotoxicity due to severe hyperglycemia.

Indeed, the expression of *Ins2* and of a subset of functional and maturation markers of β-cells [23, 164] (as described in 1.3) was downregulated in both $Ins2^{C109G}$ and $Ins2^{V26D}$. In addition, we observed a reduced number of NKX6-1+ cells in at least $Ins2^{V26D}$, which is a key marker for functionally mature β-cells [25]. The same was shown for Akita mice [94]. There may be two intertwined mechanisms that lead to this decrease. First, the mutations in the *Ins2* gene lead to a decrease of *Ins2* expression, affecting other β-cell genes. Second, the mutations disrupt correct folding, which in turn leads to ER- and oxidative stress (as described in 1.4.2 and 1.4.3 and discussed below), effectively resulting in global attenuation of transcription [165]. In summary, we propose, that by 2 months of age, mutant β-cells of both models have lost mature β-cell function and are in a dedifferentiated state due to downregulation of all β-cell markers analyzed.

An additional gene expression analysis at 1 month of age (Supplementary Figure 5, Supplementary Figure 6) revealed a reduced expression of maturation markers already at this age, leaving room for some speculations: Do the *Ins2*-mutant β-cells ever fully differentiate and reach functional maturity? Of course, as already mentioned, global

transcriptional attenuation could be present [165], but this does not help to answer this question. At least in Ins2^{V26D} we found *Ngn3*, a progenitor marker [71] increased. A few years ago, this would have allowed a solid conclusion, however, novel concepts such as the suggestion, that each β-cell dedifferentiates in its own way and does not necessarily regains properties of immature cells [72] need to be considered. Therefore, the question of differentiation vs. maturation is not so easy to answer. Instead, another question must first be answered before a conclusion can be drawn: What is the difference between differentiation, maturation and functional maturation? It is my understanding, derived from the cumulative literature review over the past 4 years, that sensing glucose and expressing insulin makes a β-cell a β-cell. Therefore, insulin expression is the hallmark of β-cells. *In utero* and after birth, the β-cells go through their maturation process. By the time β-cells start expressing insulin, they can be considered differentiated β-cells. In contrast, the secretion of functional insulin, would then be the indicator of *functional* maturity. Looking at the data from this angle, we observed residual expression of *Ins1* and *Ins2* in islets, PROINS and INS staining and even substantial insulin secretion into the plasma at 4 weeks of age in both models. Therefore, at least some β-cells must have reached functional maturity at an earlier point in time. Further experiments at P14 and P21 are needed to determine whether become mature and subsequently dedifferentiate or whether they never reached full functional maturity. Single cell analysis could shed more light on the form of dedifferentiation compared to T1DM and T2DM as described in [72].

Interestingly, the downregulation of functional markers for β-cells was less pronounced in Ins2^{C109G}, although we observed reduced β-cell mass and islet size in this model. Analysis of younger Ins2^{C109G} animals showed significantly increased blood glucose already at P7 (Supplementary Figure 2). Chronic exposure to high levels of glucose has been shown to have toxic effects on β-cells [166]. Therefore, increased glucotoxicity secondary to hyperglycemia at a very early age could disturb β-cell maturation during the postnatal period. In addition, persistent glucotoxicity could further lead to dedifferentiation [23]. Taken together, these mechanisms above-described effectively result in reduced β-cell mass in Ins2^{C109G}. In contrast, Ins2^{V26D} animals showed no reduction of β-cell mass, an observation similarly made in KINGS mice [91]. We observed hyperglycemia only after

4 weeks (Supplementary Figure 2) and conclude, that the β-cells in Ins2^{V26D} are less severely affected due to the later onset of glucotoxicity. However, the increased amount of polyhormonal cells in Ins2^{V26D}, double-positive for INS and GCG, suggests not only de- but also transdifferentiation, which could explain the persistent β-cell mass and retained islet size. Incidentally, there was no evidence of increased apoptosis or changes in proliferation in any model (Supplementary Figure 10).

Taken together, our results indicate that β-cells of both mutants do not reach maturity, dedifferentiate or transdifferentiate due to an unfavorable cellular environment.

5.2.4 Disruption of the oxidative environment

Protein disulfide isomerases (PDIs) and ER oxidoreductases (ERO) play important roles in oxidative folding of proinsulin. For example, it has been shown that an increased expression of ERO1A in the β-cell line INS1E promotes the export of wild-type insulin, even in the presence of mutant proinsulin [167]. Further, ERO1B re-oxidizes PDIs and promotes insulin biogenesis and glucose homeostasis [62]. However, in our *in vivo* study, we observed downregulation of *Ero1a* in *Ins2*^{V26D} and of *Ero1b* in both Ins2^{C109G} and Ins2^{V26D} islets. Interestingly, similar findings were made in Akita mice, where expression of *Ero1b* was decreased and that of *Ero1a* remained unchanged [59]. Unfortunately, the availability of islet samples was limited, so protein expression could not be evaluated. However, reduced expression of *Ero1a* and *Ero1b* and possibly their protein products may decrease insulin biogenesis and export of healthy insulin, consistent with less secreted insulin in both mutant lines.

PDIA1, the most abundant ER oxidoreductase, plays an important role in oxidative maturation of proinsulin, in particular during metabolic stress, and may help to dissolve HMW complexes [61], which is consistent with the increase of PDIA1 protein in our models. Also, PDIA6 seems to be critical for processing of misfolded proinsulin [100, 145], but due to the limitation of sample amounts, its protein was not evaluated in the *Ins2* models. However, *Pdia6* and *Pdia4* gene expressions were significantly upregulated in islet samples of both mutant lines. The upregulation of PDI genes in Ins2^{V26D} and Ins2^{C109G} appears to be a β-cell response that helps to dissolve HMW complexes and to promote export of healthy insulin. Taken together, the simultaneous downregulation of

Ero1 and upregulation of PDI genes in our mouse models could lead to a mismatch in oxidizing equivalents and thus to oxidative stress, which represents another obstacle to the export of healthy insulin from the ER and explains the low plasma insulin levels.

5.2.5 **ER-stress, UPR and apoptosis?**

Misfolding and an unfavorable oxidative cell milieu potentially lead to ER-stress and trigger the UPR. Therefore, a gene expression analysis of the three relevant ER-stress transducers *Ire1a*, *Eif2ak3* and *Atf6* and protein expression analysis of the chaperone BiP were performed in our mouse models. Surprisingly, none of the genes were upregulated in 8-week-old mutants compared to wild type animals even though we observed severe dilation of the ER. Instead, *Ire1a* was even found downregulated in Ins2^{C109G}. This is in contrast to Akita mice, where these genes, although analyzed in much younger animals at P21, were upregulated [94]. Interestingly, deletion of IRE1α in NOD mice, a model for T1D, led to transient dedifferentiation of β-cells prior to the onset of insulitis which protected the animals from diabetes and prevented the autoimmune destruction of their β-cells [56]. Since we propose β-cell dedifferentiation, *Ire1a*-downregulation might therefore just be another sign for β-cell dedifferentiation. BiP, the chaperone that normally associates with IRE1A, PERK and ATF6 and only dissociates upon their activation [46], was upregulated only in Ins2^{C109G}. Due to the limited sample availability, the expression of all three ER-stress transducers on the protein level remains to be elucidated.

In summary, our models show only a certain degree of classic ER-stress and UPR, which is expressed, for example, in the retention of molecules in the ER and in Ins2^{C109G} also in the increase of the chaperone BiP. BiP is regulated post-transcriptionally [168], which is why the unchanged expression of its coding gene *Hspa5* was not really surprising.

Furthermore, we observed a reduced expression of *Ddit3* in both models. *Ddit3* encodes for the ER-stress responsive element CHOP, which increases protein synthesis and leads to oxidative stress and, eventually, to cell death [169]. This observation is in line with the fact, that we observed no changes in the expression of cleaved Caspase-3, which is a downstream executioner for apoptosis [170]. As described in 1.4.2, UPR can also lead to global attenuation of transcription by Ire1-dependant decay (RIDD). Since we also observed reduced expression of β-cell markers, it is tempting to speculate that due to

global attenuation of transcription [165], overall only few transcripts are available for translation, which might explain the lack of upregulation of ER-stress genes and the downregulation of the *Ero1* genes.

5.2.6 **Activated autophagy**

Autophagy, the lysosomal degradation of proteins, has received increasing attention in recent years. Autophagy helps to remove misfolded proteins, protects cells from ER-stress, and supports β-cells in insulin homeostasis [65]. Stimulation of Akita β-cells *in vitro* with the autophagy-inducer rapamycin led to a relief from ER-stress and decrease in the expression of P62 [66]. A similar observation was made in donor islets from T2D humans [65]. However, autophagy remains to be evaluated *in vivo*. It is therefore interesting to note that the *Sqstm1* gene and its product P62 were decreased in isolated islets of our 8-week-old mutants of both lines even under basal conditions. Immunohistochemistry of P62 on pancreatic sections of animals at the same age also showed decreased P62. P62, which delivers bound molecules to the phagophore at LC3 for subsequent degradation, is self-degraded by the autolysosomes after initiation of autophagy [171]. Therefore, the reduction or absence of P62 indicates a higher level of autophagy compared to wild types, because accumulation of P62 would be a hint for reduced autophagic flux [171]. However, what the observed reduction of the *Sqstm1* gene means for its protein P62 remains a matter of speculation. Since we could not detect P62 in mutant animals with our experimental means, we do not know whether less *Sqstm1* gene product also leads to less P62, which is, as mentioned above, also degraded upon stimulated autophagy. To shed more light on the matter and better elucidate the autophagic capacity and its association with ER-stress, future experiments should involve the stimulation of autophagy and ER-stress in isolated islets.

It remains to be noted that these changes in P62 expression suggest a higher level of basal autophagy in our mutants, which seems to play a notable role in protection against ER-stress and apoptosis. Autophagy and its stimulation could be the subject of further functional studies in these mutants and shed more light on how modulated autophagy promotes β-cell survival in the presence of severe ER dilations. The results would be relevant both for T1D and T2D.

5.2.7 **Sexual dimorphism**

Most research on diabetes is performed in male animals. However, the observation of sexual dimorphism in diabetic mouse models and also in human diabetes patients is not new [172]. For example, female Akita mice harboring the disulfide-bridge affecting $Ins2^{C96Y}$ mutation appeared to be protected from the development of overt diabetes by endogenous estrogen, since treatment of male mice with conjugated estrogens prevented the onset of hyperglycemia. Furthermore, Xu et al. [95] have shown that estrogen promoted a proteasomal degradation of misfolded insulin. In another setup, the addition of estrogen to the medium of INS-1 cells protected them from oxidative and ER-stress and even from cell death due to glucotoxicity [173]. Although we only observed a mild increase in glycemia in $Ins2^{V26D}$ females, molecular analyses of gene and protein expression revealed a molecular phenotype comparable to males, leading to a paradox that has yet to be resolved. Hints in the study from Xu et al. [95] could be used to further determine the molecular effects of estrogen on the genes that were dysregulated in our models, particularly in $Ins2^{V26D}$.

$Ins2^{V26D}$ animals could therefore be a valuable mouse model in diabetes research for future studies of β-cell survival mechanisms in both sexes to further elucidate the molecular role of estrogen.

5.2.8 **Summary and potential disease mechanism**

In conclusion, both models of this comprehensive study showed severe diabetes accompanied by hypoinsulinemia, regardless of the type of mutation. In addition, we observed reduced expression of marker genes for β-cells and observed some signs for oxidative stress and severe swelling of the ER. In consequence, we observed a decline of β-cell health and finally, loss of functionally mature β-cell identity. Surprisingly, whilst ER-stress pathways were only slightly affected, autophagy pathways were deregulated. This suggests a more prominent and important role of autophagy alongside classic ER-stress. A detailed summary of similarities and differences between the models is provided in Figure 21.

In the past, not all the data collected in this work has been extensively evaluated in the same cohort of diabetic mice. Instead, many individual publications were published, that

only partially or not at all illuminated these aspects. This study, provides a comprehensive overview of a mouse model with a cysteine-mutation ($Ins2^{C109G}$) and one without ($Ins2^{V26D}$) and presents them side-by-side to provide the best possible comparisons. In fact, valuable differences were found, most notably, that non-cysteine mutations can result in a very strong phenotype that is more severe compared to all other published mouse models. Furthermore, not much is known about the effects of a C109G mutation, although there are human patients with the identical mutation [86] for whom this research can provide valuable additional information not previously known.

The following Figure 34 is a proposed model showing the overarching disease mechanism, which may also apply to other *Ins2* models but requires full evaluation there:

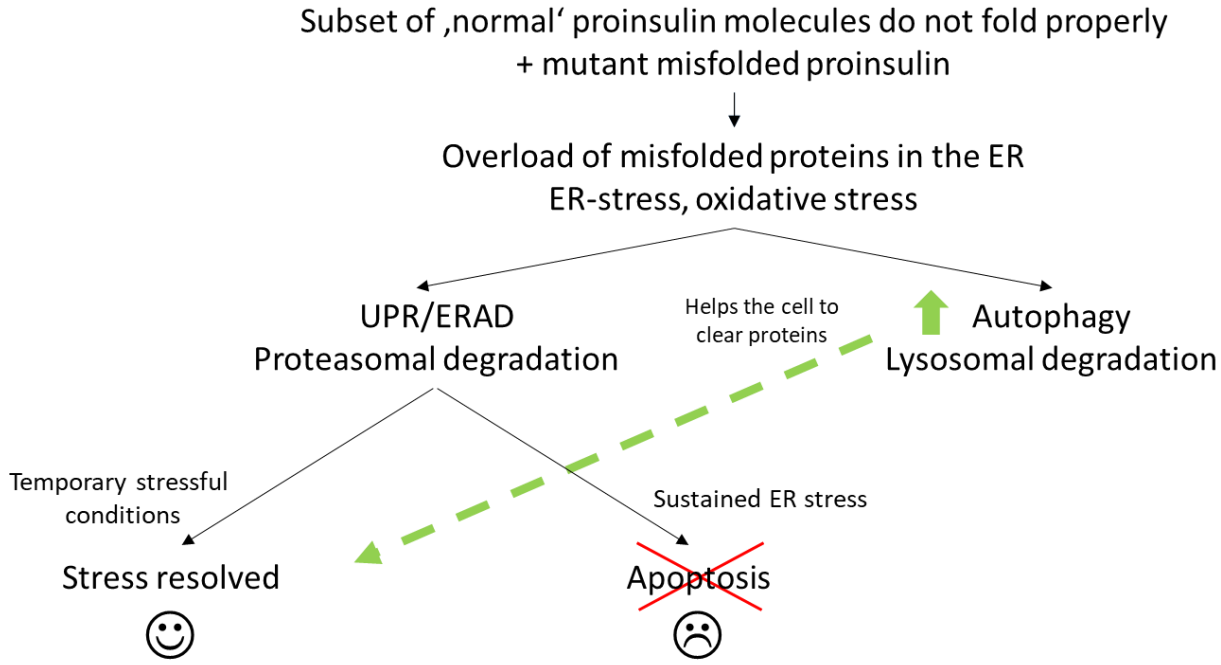

Figure 34 Proposed disease mechanism for Ins2-mutation induced diabetes in mouse models

The model is based on results obtained for this study and associated literature research. A disease mechanism is proposed where autophagy besides ER-stress plays a more prominent role than previously anticipated.

However, it is important though to keep in mind the uncovered molecular differences (see also Figure 21) and to take them into account when evaluating the models or associated human patients in relation to the proposed model.

Taken together, these results help to provide valuable insight into the pathophysiology of MIDY and, in addition, these animal models may provide important insight into β-cell survival mechanisms and the more complex pathophysiology of multifactorial T1D and T2D.

5.3 The novel mouse model Pdia6^{F175S}

Many aspects of the PDIA6-F175S mutation have already been discussed with my participation [100]. Therefore, only a few points will be highlighted and discussed in more detail here.

5.3.1 F175S versus V32A versus human mutation in *Pdia6/PDIA6*

The exchange from valine to alanine at position 32 in the first thioredoxin domain of PDIA6 (V32A) was recently evaluated in a mouse model with a strong focus on lymphoid and myeloid development [97]. Apart from the resulting immune deficiency, the authors also described altered glucose metabolism providing the first hint that *Pdia6* plays an important role *in vivo* in maintaining glucose homeostasis.

Our animal model carrying a F175S point mutation in the second thioredoxin domain of PDIA6 also showed reduced body weight with reduced body size, reduced Mendelian ratio and apparent hyperglycemia. And, similar to our model hardly any insulin or proinsulin was detectable in V32A animals [97], which was not investigated further due to the different focus of the study. Further, it should be noted that the model used for this study is a compound mouse model, where the V32A mutation results from another mutation which they call braum/-.

In contrast to our model though, the V32A mutation resulted in a reduction of PDIA6 protein, which we did not observe. Instead in our model, *Pdia6* gene expression was increased and PDIA6 protein levels remained unchanged. This finding provides some evidence that the underlying defect is due to a dysfunctional PDIA6 protein rather than due to missing protein. Therefore, it is conceivable that by upregulating *Pdia6* gene expression in Pdia6^{F175S} islets, the β-cells try to provide more transcripts for translation to compensate for the missing function. Furthermore, this observation suggests that mutations in the second thioredoxin domain might have different effects on protein abundance compared to mutations in the first thioredoxin domain, providing evidence for different functions of the two domains. Taken together, these results imply that *Pdia6* might play a larger role in glucose homeostasis and insulin secretion than previously thought. Recently, the first human patient was identified carrying a homozygous

frameshift mutation affecting the second thioredoxin domain of PDIA6, leading to severe immunodeficiency and neonatal diabetes [87].

Because *Pdia6* is expressed globally throughout the body, mutations can result in a complex, multi-organ phenotype as seen in the human patient [87]. Further studies must show to what extent the other organ systems are also affected in Pdia6^{F175S} animals. Furthermore, two independent studies have shown that mice with a homozygous whole-body knockout are not born (www.mousephenotype.org/data/genes/MGI:1919103 and [97]), further underscoring the global importance of *Pdia6*.

5.3.2 Disrupted glucose homeostasis and insulin deficiency in *Pdia6* mutants

The role of *Pdia6* in β-cell dysfunction has not been extensively explored. However, *in vitro* silencing of *Pdia6* in INS-1 cells resulted in reduced insulin secretion [60]. Eletto et al. therefore hypothesized, that sustained activity of IRE1A and subsequent Ire1-dependent decay (RIDD) reduced *Ins1* and *Ins2* expression [60]. Thus, an important role of ER-stress in the development of the *Pdia6*-associated insulin deficiency and the subsequent disruption of glucose homeostasis has been described. In summary, also with regard to the results on the two *Ins2* models described in this work, some mechanisms could be intertwined. First, mutations in the *Pdia6* gene lead to a decrease in *Ins2* expression, which affects the expression of other β-cell genes. Second, mutations any of the PDI genes can disrupt the folding environment, which in turn leads to ER- and oxidative stress, effectively leading to further global attenuation of transcription and particularly of β-cell genes [52]. A *Pdia6* mutation could therefore directly affect β-cell identity and insulin production capacities.

In adult mice, plasma insulin levels were below the detection limit of the insulin ELISA kit used, and insulin and proinsulin were barely detectable in isolated islets [100]. In addition, *Ins2* gene expression was already reduced at P21. As shown in Figure 4, insulin folding is a complicated process that requires the interaction of PDIs and EROs to establish the three disulfide bonds of the mature molecule. Any disturbance of this homeostasis can lead to dysfunction of β-cells. Thus, we observed an upregulation of the *Pdia6* gene, an increase of PDIA4 and downregulation of *Ero1a*, indicating a disrupted folding

environment in the cell. The increase in PDIA4 could represent a compensatory attempt by the cell, similar to how *Pdia4* was upregulated in a model with a PDIA1 defect [61].

Analyzing the ER-stress sensors (as described in 1.4.2), we found increased *Ire1a*, *Eif2ak3* and *Hspa5* expression. The next step was the analysis of their encoded proteins IRE1A with its active form P-IRE1A, PERK with its active form P-PERK and BiP. While IRE1A/P-IRE1A and PERK/P-PERK were unaffected at P21, BiP expression was increased, altogether indicating some ER-stress response. Analysis of some other downstream effectors of IRE1A (also described in 1.4.2) may shed more light on the RIDD hypothesis [60].

Regarding β-cell identity, we observed *Ins2* downregulation and *Gcg* upregulation at P21, along with some cells that were double-positive for insulin and glucagon. With age, we observed a massive decrease in β-cell markers [100] and an increase in α-cell markers, showing that β-cells lose their identity over time. We propose that the insulin secretory defect is more closely related to the effects of the *Pdia6* mutation on β-cell identity and homeostasis, and that *Pdia6* is a novel player in β-cell identity. This association is also reflected in the dysregulation of *Pdia6* in a model for T1DM by disruption of β-cells by STZ [174]. It may be worth checking the expression of *Pdia6* in models of T2DM with hyperinsulinemia as well to further elucidate its role in other types of diabetes and its potential role in hyperinsulinemia.

Unfortunately, an analysis of younger animals similar to the *Ins2* study is still missing. It could be shown that embryonic development is not impaired in Pdia6^{F175S} and that insulin expression is reduced at P14. Studies on P7 could therefore answer the question of whether the β-cells ever reach full maturity or when they start to lose their identity.

5.3.3 **Summary and outlook**

In summary, mice homozygous for the F175S mutation in *Pdia6* were mildly hyperglycemic at weaning and subsequently became hypoinsulinemic and overtly diabetic in adulthood. Within this study, we have shown that *Pdia6* plays an important role in insulin synthesis and secretion and propose that it is a novel player affecting β-cell identity. Although there is an unfavorable oxidative environment, it is not yet known whether insulin accumulates in the ER of Pdia6^{F175S} mice. Future experiments could

therefore include the analysis of β-cells by transmission electron microscopy and, for example, additional immunohistochemistry against calreticulin. Furthermore, as briefly highlighted in this study, a functioning ER-stress machinery is of utmost important for the development of β-cells. Therefore, future studies should also consider the investigation of ER-stress mechanisms in more detail and analyze their downstream effectors to properly examine whether the loss of insulin transcripts *in vivo* is due to RIDD-mediated decay, as suggested by Eletto et al. [60]. Finally, *Pdia6* is ubiquitously expressed and its function in other organs remains to be elucidated.

5.4 *Hnf4a*-mouse models and the missing phenotype

It has been proven to be very difficult to identify a mouse model with a disruption of *Hnf4a,* in a variety of attempts that reflects the human phenotype of MODY1. Therefore, this discussion is focused on the potential underlying mechanisms for the missing phenotype.

5.4.1 Missing reduction of HNF4A in Hnf4a^{tm1b}, Hnf4a^{R333L}, Hnf4a^{G124A} and hemizygous mice

In general, our findings suggest that damaging mutations in *Hnf4a*, when homozygous, are embryonically lethal and might be tolerable when heterozygous. MODY1 in humans is usually caused by spontaneously occurring or hereditary point mutations [32]. These point mutations can result in frameshift or missense mutations and possibly even to a premature stop codon, effectively reducing the HNF4A dose. In general, when homozygous mutations are observed in humans, they are often inherited by children of consanguineous parents who are both heterozygous carriers. An example is the human patient with a *Pdia6* mutation [87]. Yet, turning off a gene or knocking out a gene in rodents is a commonly used tool to better understand its function. In this work, a multiple approach was followed to identify a suitable mouse model for MODY1: the investigation of a whole-body knockout, the generation and characterization of two point mutation models (to better represent the human situation), the reduction of the *Hnf4a* gene dose by generating two hemizygous mouse lines (each carrying a point mutation and a knockout allele) and the generation of a mouse model with a β-cell specific downregulation of *Hnf4a.* To date, no patients have been reported who carry a homozygous mutation in the *HNF4A* gene. Also, no mouse models have been described to date, including our own, which are homozygous for whole-body mutations in *Hnf4a*. As described in 1.6.3, HNF4A is an important transcription factor that is expressed during development and in many organs, hence, it is not surprising that homozygous disruption resulted in early embryonic death in mice [113]. This could also explain why there are no patients with homozygous mutations in *HNF4A*.

A fundamental difference between human and mouse seems to lie in the expression of *HNF4A*/*Hnf4a* itself. In the islets of mice, expression was found to by 10 times higher compared to human islets [115]. A heterozygous *Hnf4a* knockout might provide a gene

reduction of about 50% and could therefore better reflect the human situation. As early as 1997 it was stated that heterozygous *Hnf4a* knockouts do not show any phenotype [114]. However, this was only mentioned in one sentence and results were never published. Therefore, we decided to analyze a new knockout model, but after detailed phenotyping of the heterozygous mice, even if they were more than one year old (data not shown), we did not observe any metabolic changes. However, it was surprising that no changes of *Hnf4a* gene expression or HNF4A protein expression were found when examining expressions in the liver, the main organ where HNF4A is expressed and which is easily accessible. Genotyping was performed targeting the lacZ site introduced by the tm1b KO strategy [146], thereby confirming the presence of the knockout and omitting sequencing. The fact that no homozygous animals were born speaks against the possibility that the knockout was somehow leaky and further confirms the functionality of the knockout allele. Also surprising was the similar findings in the models with the R333L and G124A point mutations and in hemizygous mice carrying one knockout and one point mutation allele, although the point mutations were predicted to be deleterious. So, there seems to be compensatory mechanism that somehow protects the cells from losing HNF4A protein.

Changes in the amount of transcription factors can impact the absolute activity of a gene and the entire transcription factor network. Alternatively, the expression of HNF4A in our mutants may still have been above a certain threshold that is required for the manifestation of a disease phenotype. Such a disease scenario has already been proposed by Harries et al. [115], which is hereby confirmed.

5.4.2 Missing phenotype in Hnf4a-KI and the hierarchical regulatory relationship of *Hnf1a* and *Hnf4a*

So far, only mice with a targeted islet-specific knockout of *Hnf4a* were viable and presented a mild phenotype with hyperinsulinemia and impaired glucose tolerance [110]. Our approach with a β-cell specific downregulation of *Hnf4a* was successful in that we could significantly reduce the *Hnf4a* gene dose in the islets significantly without affecting the expression in the liver, demonstrating that our novel approach to downregulate endogenous genes worked as intended. Although we showed a concomitant downregulation of the HNF4A target gene *Slc2a2,* HNF4A-KI mice did not develop a diabetic phenotype. However, the HNF4A protein content in islets has yet to be quantified. We also observed no changes in *Hnf1a* expression. We propose that the underlying reason for the missing phenotype might be the hierarchical relationship between *Hnf1a* and *Hnf4a*. It has long been described that HNF4A and HNF1A share a common regulatory network in islets and that they jointly regulate β-cell function [108, 149]. These two transcription factors have been shown to regulate a similar set of genes and have been found to regulate common targets synergistically. However, HNF1A has also been described as being higher in the regulatory hierarchy [103, 107, 108]. Boj et al. [108] proposed a model with HNF1A upstream of HNF4A, which is shown in the following Figure 35:

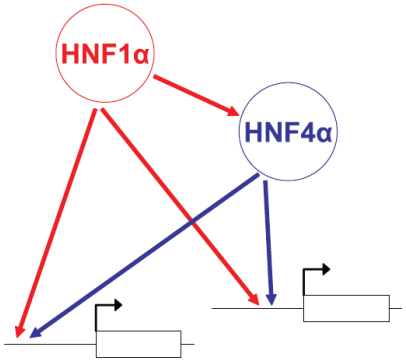

Figure 35 Hierarchical relationship of HNF1A and HNF4A

Figure was adapted from Boj et al., 2010.

Since we did not observe any regulation of *Hnf1a*, the missing phenotypic effect could be due to the assumption that *Hnf1a* takes over the regulation of genes that are normally regulated by *Hnf4a.* Since *Hnf1a* is located higher in the regulatory network, it could

compensate for the loss of *Hnf4a*, resulting in only mild effects such as reduced *Slc2a2* in otherwise healthy animals. Alternatively, *Hnf4g* might compensate for the loss of *Hnf4a* as recently demonstrated for the targeted deletion of *Hnf4a* in the intestine [175]. While these presumptions remain to be explored, Hnf4a-KI mice could provide a valuable resource for further analyses on the HNF transcription factors network in islets. A double KO of *Hnf1a* and *Hnf4a* could provide additional information on how disturbance of the network affects the metabolic state of animals.

Further follow-up studies could include the reduction of *Slc2a2* expression and whether this has an impact on GLUT2 abundance and the insulin secretory capacity of islets *in vitro*. Therefore, a GSIS experiment with islets of HNF4A-KI animals could shed light on this matter. In HNF4A- defective INS-1 cells, *Slc2a2* and *insulin* were reduced, resulting in defective GSIS [103]. However, the concomitant *insulin* reduction was not observed in our model. This observation once again underscores the importance of *in vivo* evaluation of *in vitro* data. However, in our model, we could not detect a complete loss of *Hnf4a* transcripts, so there may still be enough transcripts left for the normal function of the transcription factor. On the other hand, HNF1A and/or HNF4G may have taken over the regulation of most genes, resulting in wild-type-like mice. In future experiments, one could also include e.g. gene expression analysis on other genes important for normal β-cell function, such as *Abcc8* and *Kcnj11*. Finally, since we do not observe any *in vivo* phenotype, it must be kept in mind that these experiments can only be source for exploring further compensatory mechanisms and for revealing differences between mice and humans.

5.4.3 **Ongoing and future experiments**

Since we observed *Hnf4a* downregulation and few other effects at the molecular level in HNF4A-KI mice, it might be worth performing further experiments. Some of them are already in the hands of my successors Maximilian Schmidtke and Aliona Harten. To add an environmental trigger to the genetic disruption, mice were placed on a high fat diet (HFD) and my successors are currently awaiting results. In addition, a cohort of mice could be left up to about 1 year of age to test whether diabetes occurs late in life. Additional sample collection is currently underway for the experiments suggested above.

Hopefully, these experiments will provide more detailed information about the missing phenotype.

5.5 The intricate procedure of intraductal injection

Establishing the microsurgical procedure of intraductal injection was a team effort of our *Functional Genetics* group. The best possible results could only be achieved by working together and finding best-practice examples.

Microsurgery for intraductal injection is an intricate procedure. Many things need to be considered before starting, for example the local environment, available equipment and tools, personal skills of the surgeons, but also local regulations regarding experiment approvals and animal welfare. In order to get approval and to establish the method in our animal facility, extensive training at the UAB facility in Barcelona and lots of further training were required.

Implementation of the whole procedure has proven to be a constant learning process. We have reorganized the laboratory to keep the surgical area as sterile as possible. To give the surgeon a good view, we have added a ring light to the stereomicroscope. We have also used tungsten carbide surgical instruments to achieve the best possible performance. And to increase animal welfare, we added buprenorphine as an additional analgesic during surgery and also treated with meloxicam for the three following days.

In order to avoid injury during surgery, one should not touch the pancreas at any time and should not use sharp tools when moving the liver lobes and intestines. In addition, the hole in the bile duct created during the injection should not be closed with too much tissue glue in order to prevent the organs from sticking together and not to impede the subsequent islet isolation. When closing the surgical wound, the suture of the muscle layer must be kept as flat as possible, while the ends of the skin suture must not be too short to prevent the knots from opening.

5.6 Gene therapy for mouse models for monogenic diabetes

As intended, homozygous Hnf4a-KI animals showed significant downregulation of *Hnf4a* in pancreatic islets. Therefore, the first cohort of HNF4A-KI animals, divided into a control group and a treatment group were treated with rAAV8- However, the follow up analyses were not yet complete at the time of writing of this thesis. In the following, the discussion therefore focuses on experimental limitations and ongoing and future experiments.

5.6.1 Experimental limitations

After surgery for the intraductal administration of substances (rAAV or PBS solution) the animals were closely monitored for several days. Consequently, surgeries had to be limited to two days a week. With only one surgeon, the capacity was limited to a maximum of 10 animals per week. Another limitation was that initially, male animals at the right age and with the right genotype need to be available, but, at the same time breeding excess should be avoided. For this reason, the surgeries have only been performed on one control group (wild types injected with vehicle solution) and the treatment group (homozygous Hnf4a-KI injected with vector solution). This shows that careful planning in advance of such a project is essential. Due to the limitations mentioned above and additional delays in material supply during and after the Corona pandemic, the second control group (homozygous Hnf4a-KI, injected with vehicle solution) could not be included in this work. The dosage of the anesthetics also proved to be a limiting factor. With the originally used mixing ratio of ketamine/xylazine (100 mg/16 mg per kg/BW), which corresponds to that of our cooperation partners at the UAB, some animals did not wake up from anesthesia after surgery. Only after switching to a ketamine/xylazine dose of 100 mg/10 mg per kg/BW this did no longer occur. This again proves that each step of the surgical procedure needs to be carefully evaluated and regular troubleshooting is of utmost importance

5.6.2 Ongoing and future experiments with Hnf4a-KI

After the treated animals have been rested for four weeks, they are currently being phenotyped as shown in Figure 9. However, this work is not yet complete. To date, no differences have been observed between the rAAV-treated Hnf4a-KI animals and the vehicle-treated wild-type littermates. From today's perspective, this shows that treatment with rAAV does not appear to have any negative effects on body weight, blood sugar, glucose tolerance or insulin tolerance. The absence of such side effects is consistent with the findings of our cooperation partners in the rAAV treatment of diabetic Hnf1a-KI animals (Fatima Bosch, personal communication). The analysis of feces and urine samples from the treated animals one week after administration also shows that treatment with rAAV can be regarded as safe, since no viral nucleic acids could be detected in the excrements.

Upon completion of the phenotyping of live animals, *Hnf4a* expression will be examined at RNA and protein level in isolated islets and in liver to verify that vector administration results in restoring *Hnf4a* expression in islets of Hnf4a-KI animals and does not cause off-target effects in the liver. For further comparisons and studies on possible side effects, Hnf4a-KI animals treated with vehicle solution would have to be added as an additional control group

Overall, the gene therapy carried out can be considered successful in terms of method development and optimization of the surgical steps, which is evidenced by the significantly improved survival rate. Together with the absence of negative or toxic side effects, the results obtained form the basis for future experiments within the group.

5.6.3 AAV-vector design and choice of promoter

The design of the AAV vector and the selection of a suitable promoter was carried out by our cooperation partner at UAB. Three different promoters were evaluated in cell culture to determine the optimal expression level of the therapeutic gene to be transferred to β-cells. However, the promoter selected cannot be specified yet since it is part of the patent application which is not yet publicly available.

5.6.4 Future perspectives for other mouse models of monogenic diabetes and humans

After successfully establishing the surgical method and targeting the vector expression to β-cells, an important question remains unanswered: Is this method also suitable for the treatment of other mouse models with monogenic diabetes?

In my opinion, a basic distinction must be made between two types of monogenic diabetes: Loss of function and gain of (toxic) function mutations. It is also important to consider whether the effect is β-cell specific (such as in our *Ins2* models) or affects the whole body (such as in our *Pdia6* model).

For all loss-of-function cases, gene therapy, i.e. providing a healthy version of the gene, seems to be a suitable option and offers good prospects for the affected patients In the case of mutations that lead to a toxic function, the situation is more complex. In $Ins2^{C109G}$ and $Ins2^{V26D}$ animals, the mutant insulin forms HMW complexes with the healthy insulin

and accumulates in the ER, thereby preventing healthy insulin from exiting. Providing a healthy copy of the gene may enhance this phenotype, significantly increasing ER-stress and triggering apoptosis. In this case, other approaches must be chosen. One idea is to try to alleviate ER-stress, for example, by providing a copy of the gene *Ero1b* to improve redox potential or by providing a gene like *Sqstm1* that enhances autophagy to reduce the burden of misfolded proteins. However, the side effects of such a treatment are unpredictable and the effects of the increased gene dose could play a major role. Another idea is to try *in vivo* gene editing with AAV-vectors to deliver CRISPR and a Cas-endonuclease into β-cells and correct the mutation *in vivo*. This approach has proven to be successful in a retinal disease [176]. However, it must be carefully examined which Cas-endonuclease is most effective [177]. Therefore, this approach requires many preliminary *in vitro* experiments to assess all the intricacies associated with this potential treatment.

Another problem occurs in the *Pdia6* model. *Pdia6* is expressed globally, and, as shown by all previous studies, including our own, the defects are widespread throughout the body. While treating only the β-cells could improve glucose homeostasis, other defects, such as immunodeficiency [60], would remain untreated. Therefore, intraductal delivery to β-cells, may not be the right choice in this case. Whole body delivery using a ubiquitous promoter may represent a better treatment option. One method of administration could be via the blood stream, which of course is low-invasive. However, whole body administration has its own side effects, some of which are highlighted here: Very high doses are required, transduction efficiency varies greatly in different tissues [178], and pre-existing immunity to AAV in humans, needs to be evaluated in humans prior to *in vivo* treatment [131].

5.7 **Closing remarks and future perspectives**

In this work, nine mouse models (see Table 15) were phenotyped *in vivo*. The molecular *in vitro* evaluation of the phenotype was carried out for each mouse line with regard to the respective mutations and adapted to findings made during the process. Furthermore, with the help of other group members, the technique of intraductal injection using a microsurgical procedure was successfully established. We treated the first mouse model,

Hnf4a-KI mice, greatly improving our skills and thereby optimizing the method for future treatments of other mouse models.

Unfortunately, it has not been possible to identify a suitable model for MODY1. *Hnf4a* appears to be a difficult gene to manipulate, particularly in rodents. Future experiments could include phenotyping other mouse models of monogenic diabetes with loss-of-function mutations. An overview of possible mutations can be found in Hattersley et al. [179]. MODY4 diabetes caused by *Pdx1* mutations is one example.

6. Acknowledgements

The process of obtaining a doctorate degree felt like going on a big adventure. At the beginning, I did not know what I got myself into. Soon, curiosity was my continuous guide and hard work started to pay off. Along the way though, I took a few (expected) detours, because not everything can be foreseen and sometimes, science does not behave in the way we expect it to behave. Eventually though, one manages to return to the path that leads to the end of the tunnel. And finally, there it is, the end! Of course, I did not go through this process all by myself. Some great people helped along the way by providing guidance, scientific expertise, company and encouraging word here and there.

First of all, I would like to express my gratitude to Martin Hrabě de Angelis, for giving me the chance to work together and venture into the field of gene therapy. Martin always kept me on track, provided guidance where necessary and never lost sight of the bigger picture. Thank you for your honest opinions, critical questions and never ending curiosity.

Another big thank you goes out to Gerhard Przemeck, who provided guidance and supervision on a daily basis and always checked on my progress. Thank you for all your patience with my bubbly nature and always taking the time to read through manuscripts and my thesis – your writing tips are the best and have greatly shaped my scientific writing.

Another hearty thanks goes out to Nirav Chhabra. I consider myself very lucky to have had you as my postdoc mentor. Thanks for being a persistent teacher and helping me set up experiments. I will forever remember our enthusiastic, heated discussions and your motivational talks – not only as colleagues but also as friends. Also, I will never forget the 24h experiments and our crazy snowstorm trip to Barcelona.

I am also exceptionally grateful for the excellent technical help by Andreas Mayer and Michael Schulz. If you are in need of a teacher for all mouse related experiments, there is no better teacher than Andreas. Thanks for being the best surgical assistant out there and your forever positive attitude! Also thank you to Micha for providing expertise in the lab outside of the mouse facility – you are the king of western blots. Another thank you goes to Lucy, Marion and Elli.

A huge thanks goes out to our collaborators at the UAB (Fatima, Veronica, Miquel and Estefania). Without you, gene therapy would have been unthinkable. Thank you for your patience in teaching us how to perform intraductal injections and adjusting to German bureaucracy.

Of course, a special thanks also goes to other colleagues (Adriano Maida, Birgit Rathkolb, Lore Becker, Julia Calzada-Wack, Jan Rozman, Annette Feuchtinger, Susan Marschall, Florian Giesert, Raffaele Teperino, Raffaele Gerlini) who have helped along the way by providing mice, samples, experimental help, expertise and guidance as well as fruitful discussions.

I would also like to acknowledge my other office colleagues that I also consider friends. Sandra, your positive attitude and kind words have significantly improved many of my days. Selina and Dani (and also Nirav), there is no better way to start into the weekend then to have some Friday afternoon office-deep-talk about everything that would come to our minds. Maxi and Aliona, thanks for taking over my projects, valuing my opinion and always keeping me updated. Thank you all for making this period of my life unforgettable.

I found another home working alongside some fellow doctoral researchers in the DINI group and also with the HeJus. I might just become a party planner/networking event organizer now as a second career. Thank you all for your friendship, for being there for that period of my life and helping me get through some difficulties.

Last but certainly not least, I am thankful to my friends and family for simply being there and constantly caring about my wellbeing. I am grateful for my parents checking in on me regularly and making sure I have everything I need. Moritz, thank you for your enthusiasm about all the things I do without questions. Michi, you entered this process only at a later point, but I am grateful to have you in my life, that you tolerated me while I was writing this thesis and also that you kept my spirits high at all times. Thank you all for your faith in me and your love.

7. Publications and posters

Publications related to this thesis in peer-reviewed journals

Chhabra, N. F., Amend, A. L., Bastidas-Ponce, A., Sabrautzki, S., Tarquis-Medina, M., Sachs, S., . . . Hrabe de Angelis, M. (2021). **A point mutation in the Pdia6 gene results in loss of pancreatic beta-cell identity causing overt diabetes**. Mol Metab, 101334. doi:10.1016/j.molmet.2021.101334

Poster presentations related to this thesis

Anna-Lena Amend, Nirav Chhabra, Gerhard Przemeck, Martin Hrabě de Angelis. **Why research on rare forms of diabetes deserves more attention.** 8th DZD Diabetes Research School, September and October 2020, Virtual Format

Anna-Lena Amend, Nirav Chhabra, Gerhard Przemeck, Martin Hrabě de Angelis. **New mouse models for rare forms of diabetes: *Ins2*^{C109G} and *Ins2*^{V26D}**." N^2 Joint Event 2019: From Research to Application, 13.-15.11.2019, Berlin

Anna-Lena Amend, Nirav Chhabra, Andreas Mayer, Michael Schulz, Gerhard Przemeck, Martin Hrabě de Angelis. **Establishment of new mouse models for monogenic forms of diabetes: *Ins2*^{C109G} and *Ins2*^{V26D}**. 22nd DZD Workshop at DDZ, 29.-30.04.2019, Düsseldorf

Anna-Lena Amend, Nirav Chhabra, Andreas Mayer, Michael Schulz, Gerhard Przemeck, Martin Hrabě de Angelis. **Establishment of new mouse models for monogenic forms of diabetes: *Ins2*^{C109G} and *Ins2*^{V26D}**. 6th DZD Diabetes Research School, 29.09.-01.10.2018, Berlin

Other peer-reviewed publications

Chhabra, N. F., Amarie, O. V., Wu, M., Amend, A. L., Rubey, M., Gradinger, D., . . . Hrabe de Angelis, M. (2020). **PAX6 mutation alters circadian rhythm and beta cell function in mice without affecting glucose tolerance.** Commun Biol, 3(1), 628. doi:10.1038/s42003-020-01337-x

Saller, M. M., Huettl, R. E., Hanuschick, P., Amend, A. L., Alberton, P., Aszodi, A., & Huber, A. B. (2016). **The role of Sema3-Npn-1 signaling during diaphragm innervation and muscle development.** J Cell Sci, 129(17), 3295-3308. doi:10.1242/jcs.186015

Appendix A

Supplementary Figures that are mentioned in the text.

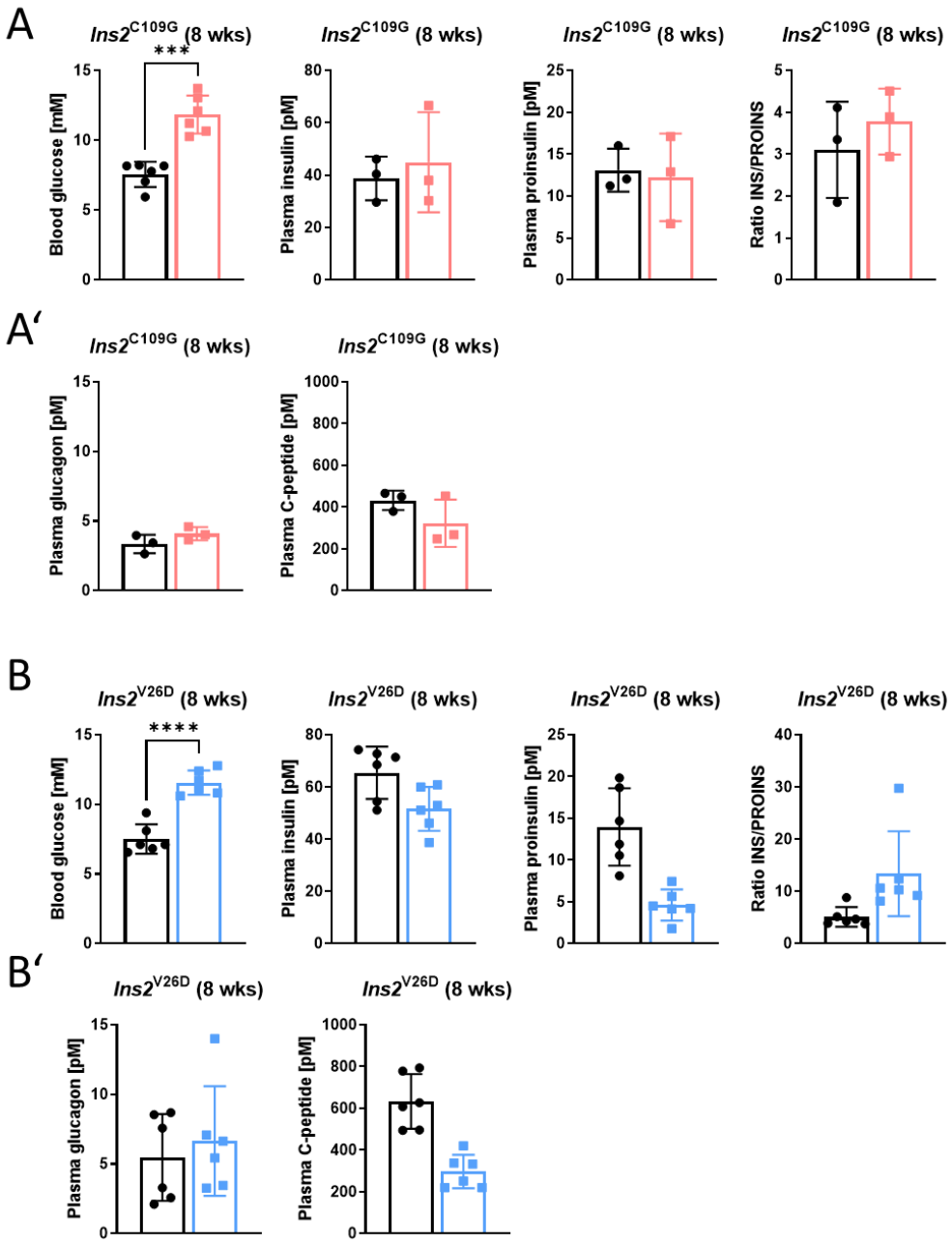

Supplementary Figure 1 Mild hyperglycemia but normal hormone secretion in 8-week-old female Ins2^{C109G} and Ins2^{V26D}

(A-B) Blood glucose [mM], plasma insulin [pM], plasma proinsulin [pM] and ratio of insulin/proinsulin from 8-week-old fasted (6h) Ins2^{C109G} **(A)** and Ins2^{V26D} **(B)** compared to wild types; n=3-6. **(A'-B')** Plasma glucagon [pM] and plasma C-peptide [pM] from 8-weeks-old fasted (6h) *Ins2*^{C109G} **(A')** and *Ins2*^{V26D} **(B')** compared to wild types; n=3-6.

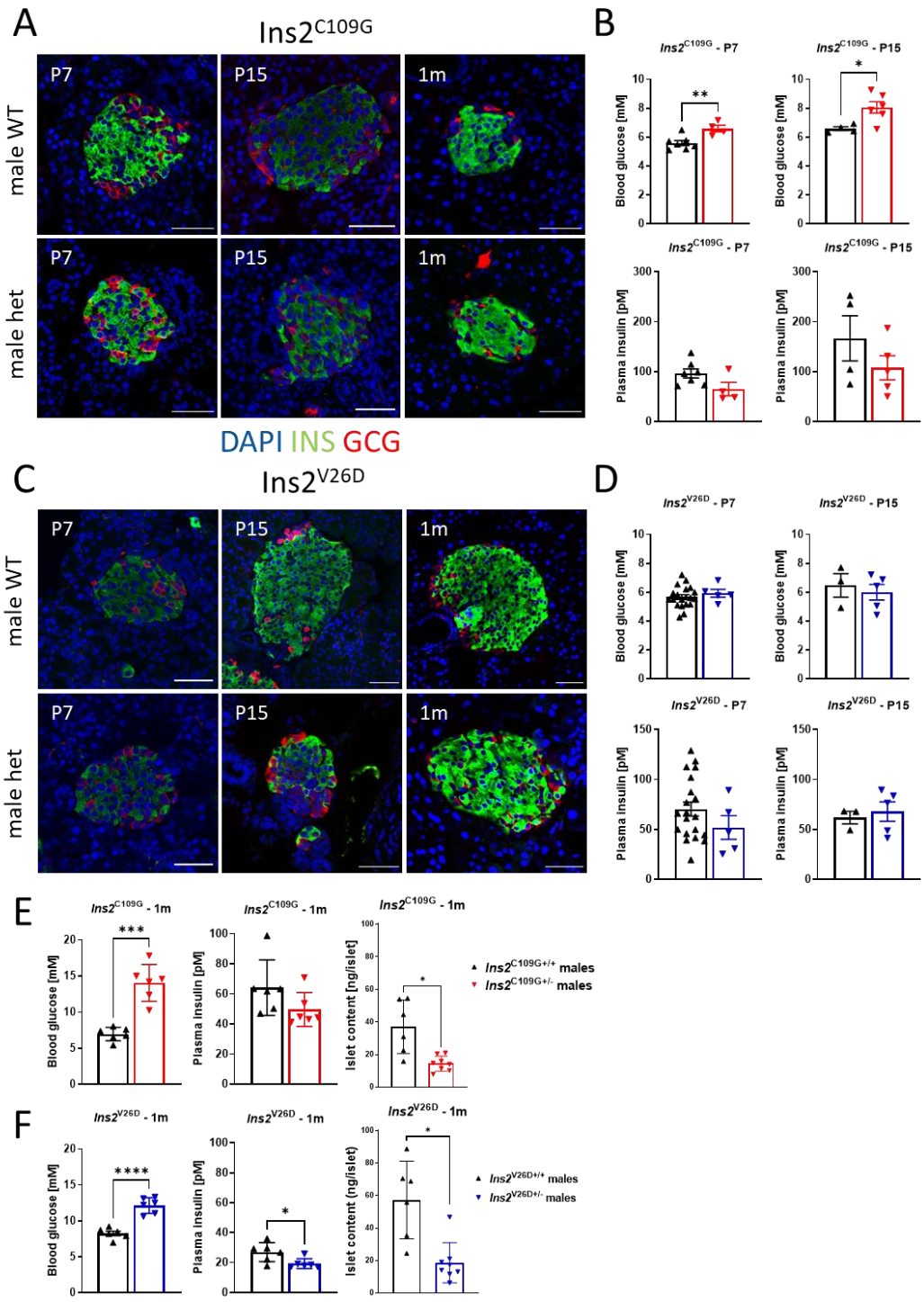

Supplementary Figure 2 Islet morphology, blood glucose and plasma insulin from P7, P15 and 1-month-old animals, islet content from 1-month-old animals

(A, C) Representative images of islets of Langerhans from WT, Ins2^{C109G} and Ins2^{V26D} animals. DAPI: blue, insulin: green, glucagon: red. Scale bars equal 50 µm. **(B, D)** Blood glucose [mM] and plasma insulin [pM], from P7 and P15 Ins2^{C109G} **(B)** and Ins2^{V26D} **(D)** males and females; n=4-20. **(E-F)** Blood glucose [mM] and plasma insulin [pM] from 4-week-old 6 h fasted animals, insulin content in islets from random fed animals in WT and Ins2^{C109G} **(E)** and Ins2^{V26D} **(F)** males; n=5-6.

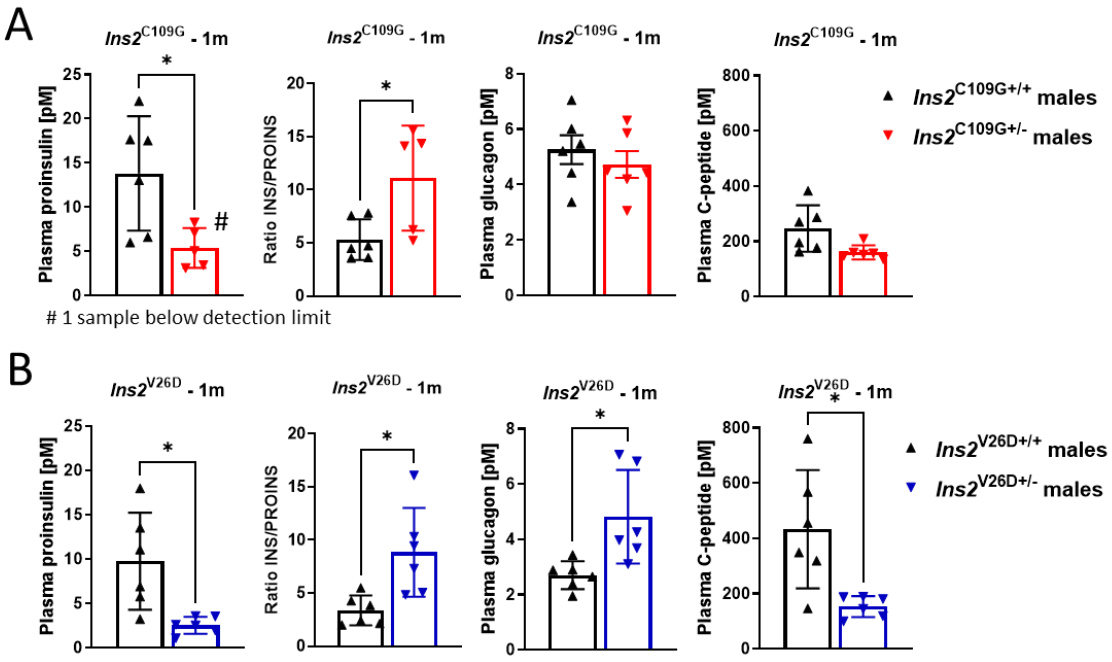

Supplementary Figure 3 Hormone secretion to the plasma in 1-month-old animals

(A-B) Plasma proinsulin [pM], ratio of insulin/proinsulin, plasma glucagon [pM] and plasma C-peptide [pM] from 4-week-old 6 h fasted WT, Ins2^{C109G} **(A)** and Ins2^{V26D} **(B)** male animals; n=4-6.

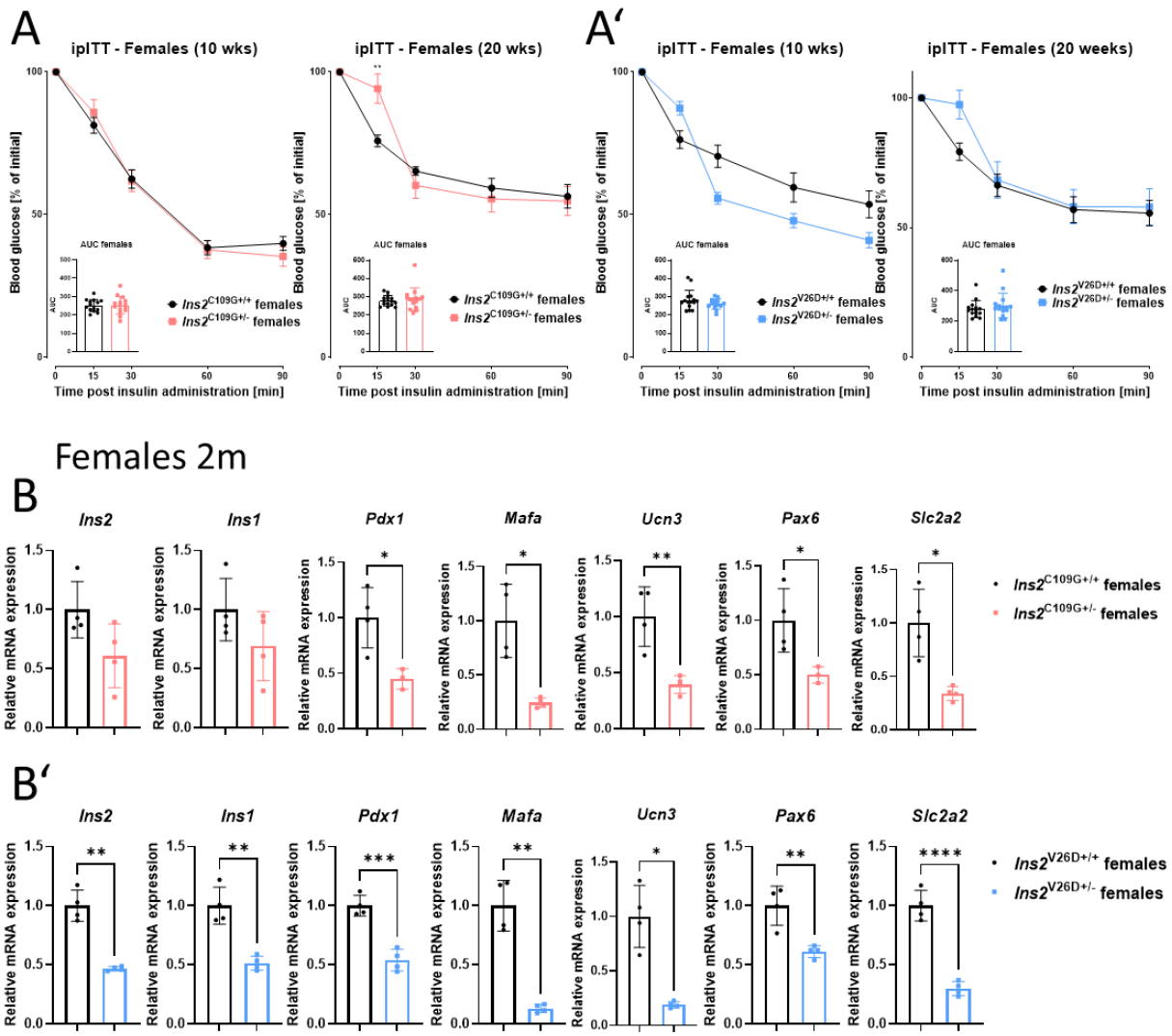

Supplementary Figure 4 ipITT results and mature β-cell markers in Ins2^{C109G} and Ins2^{V26D} females

(A-A') ipITT (0.75 U/kg BW) in **(A)** 10-week- and 20-week-old *Ins2*^{C109G} and WT; AUC; n=14-15 and **(A')** 10- and 20-week-old Ins2^{V26D} and WT, AUC; n=15. **(B-B')** Relative mRNA expression of *Ins2*, *Ins1*, *Pdx1*, *Mafa*, *Ucn3*, *Pax6* and *Slc2a2* in **(B)** WT and Ins2$^{C109G+/-}$females and **(B')** WT and Ins2$^{V26D+/-}$ females aged 8 weeks**;** n=3-4.

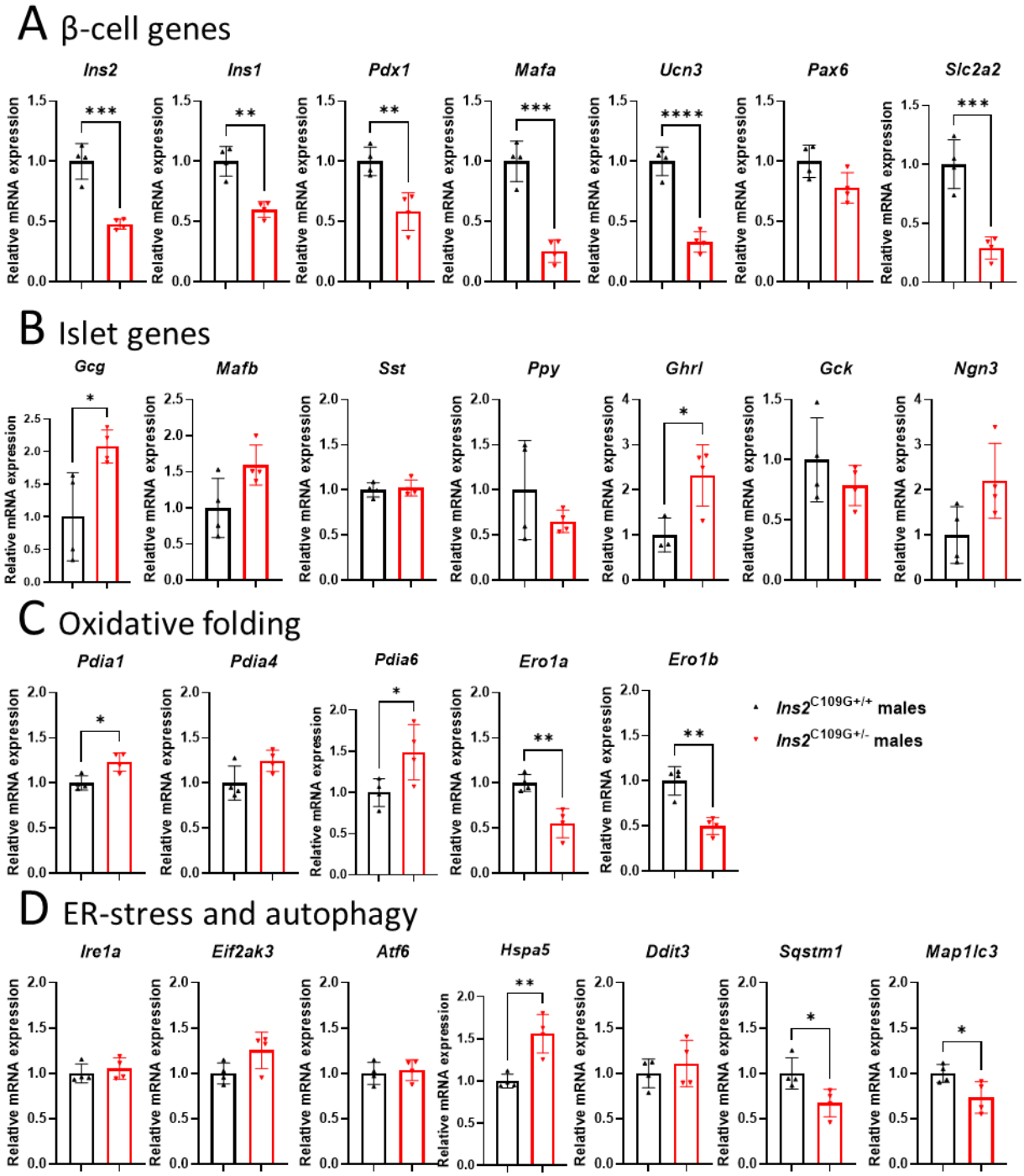

Supplementary Figure 5 Gene expression analysis in islets from 1-month-old Ins2^{C109G}

Relative mRNA expression of genes associated with **(A)** β-cell identity, **(B)** islet function, **(C)** oxidative folding, and **(D)** ER-stress and autophagy in WT and Ins2$^{C109G+/-}$ males aged 4 weeks**;** n=3-4.

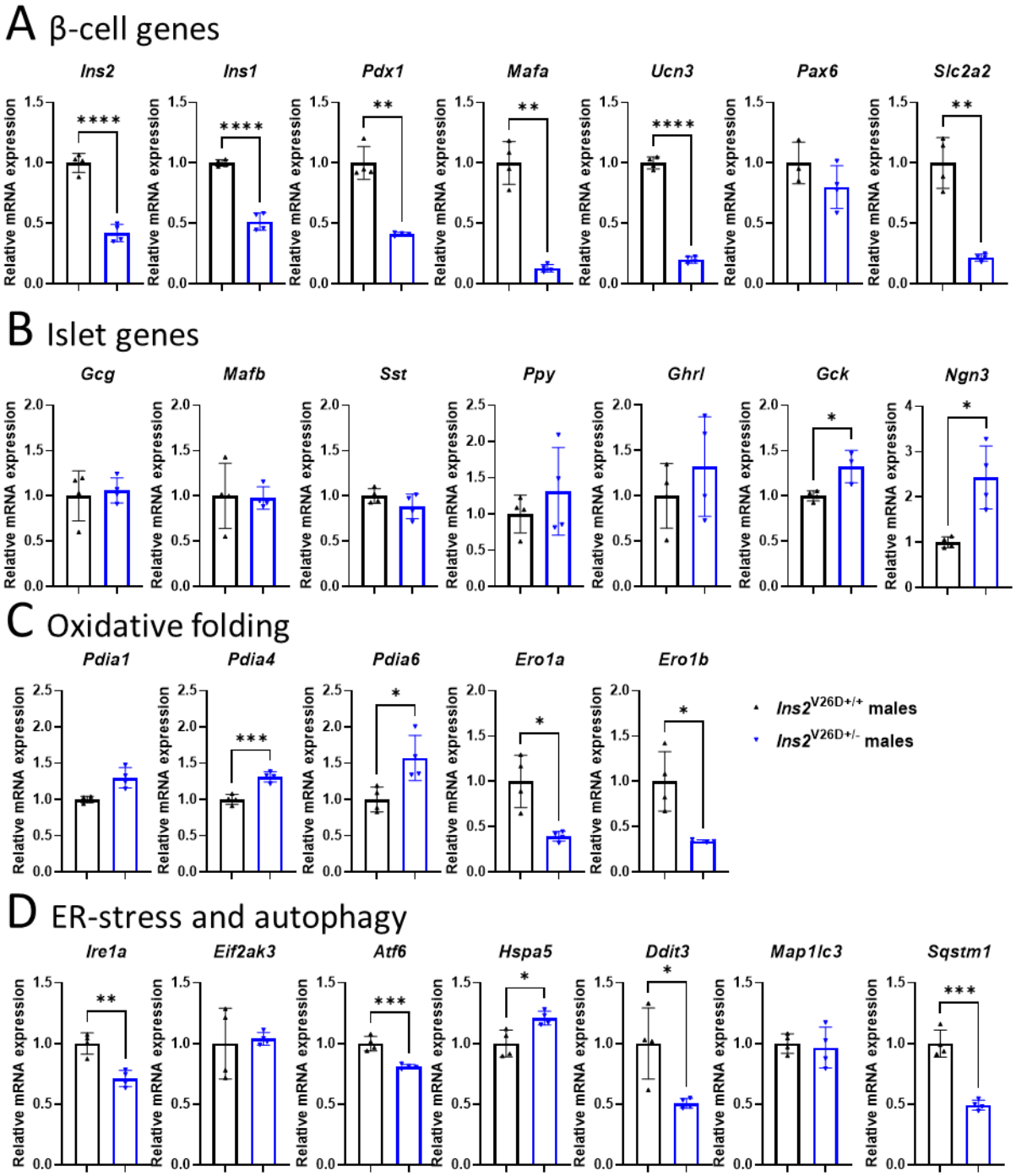

Supplementary Figure 6 Gene expression analysis in islets from 1-month-old Ins2^{V26D}

Relative mRNA expression of genes associated with **(A)** β-cell identity, **(B)** islet function, **(C)** oxidative folding, and **(D)** ER-stress and autophagy in WT and Ins2$^{V26D+/-}$ males aged 4 weeks**;** n=3-4.

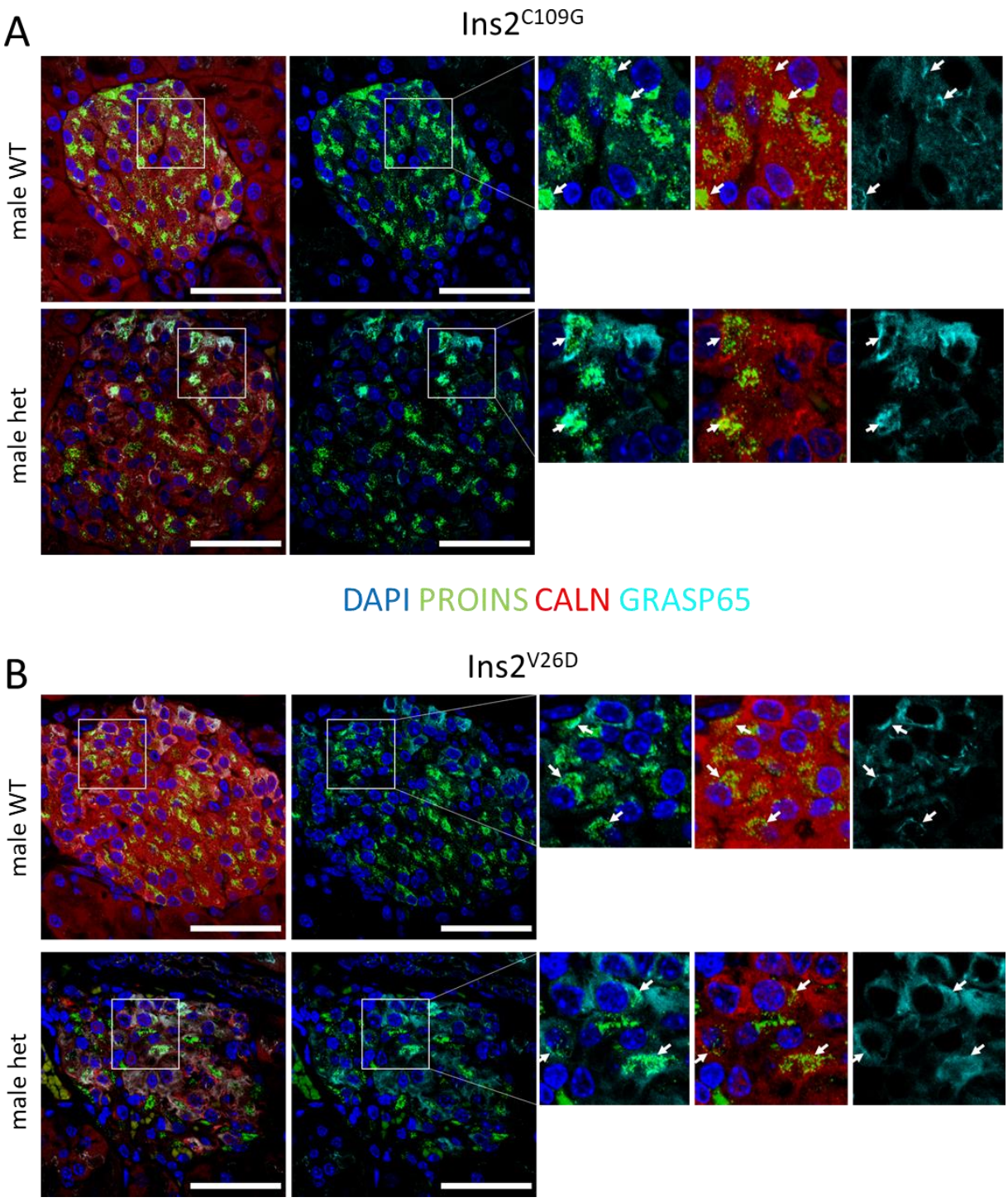

Supplementary Figure 7 Golgi-staining of Ins2^{C109G} and Ins2^{V26D} males

(A-B) Representative images of islets of Langerhans' of Ins2^{C109G} **(A)**, Ins2^{V26D} **(B),** and WT male animals. White arrows in all panels highlight Golgi structures that co-localize with proinsulin. DAPI: blue, proinsulin: green, calnexin: red, GRASP65: cyan; Scale bars equal 50 µm; age 8 weeks.

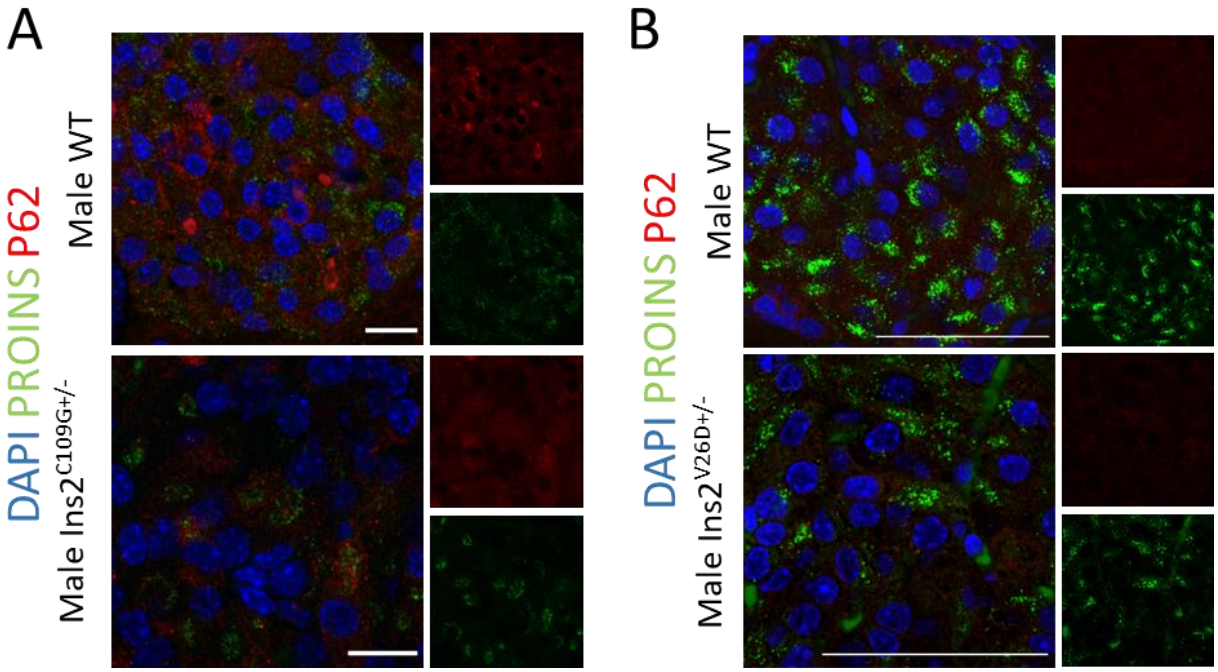

Supplementary Figure 8 P62 staining in Ins2 mutants

(A-B) Representative images of islets of Langerhans' of $Ins2^{C109G}$ **(A)**, $Ins2^{V26D}$ **(B),** and WT male animals. DAPI: blue, proinsulin: green, P62: red; Scale bars equal 50 µm; age 8 weeks.

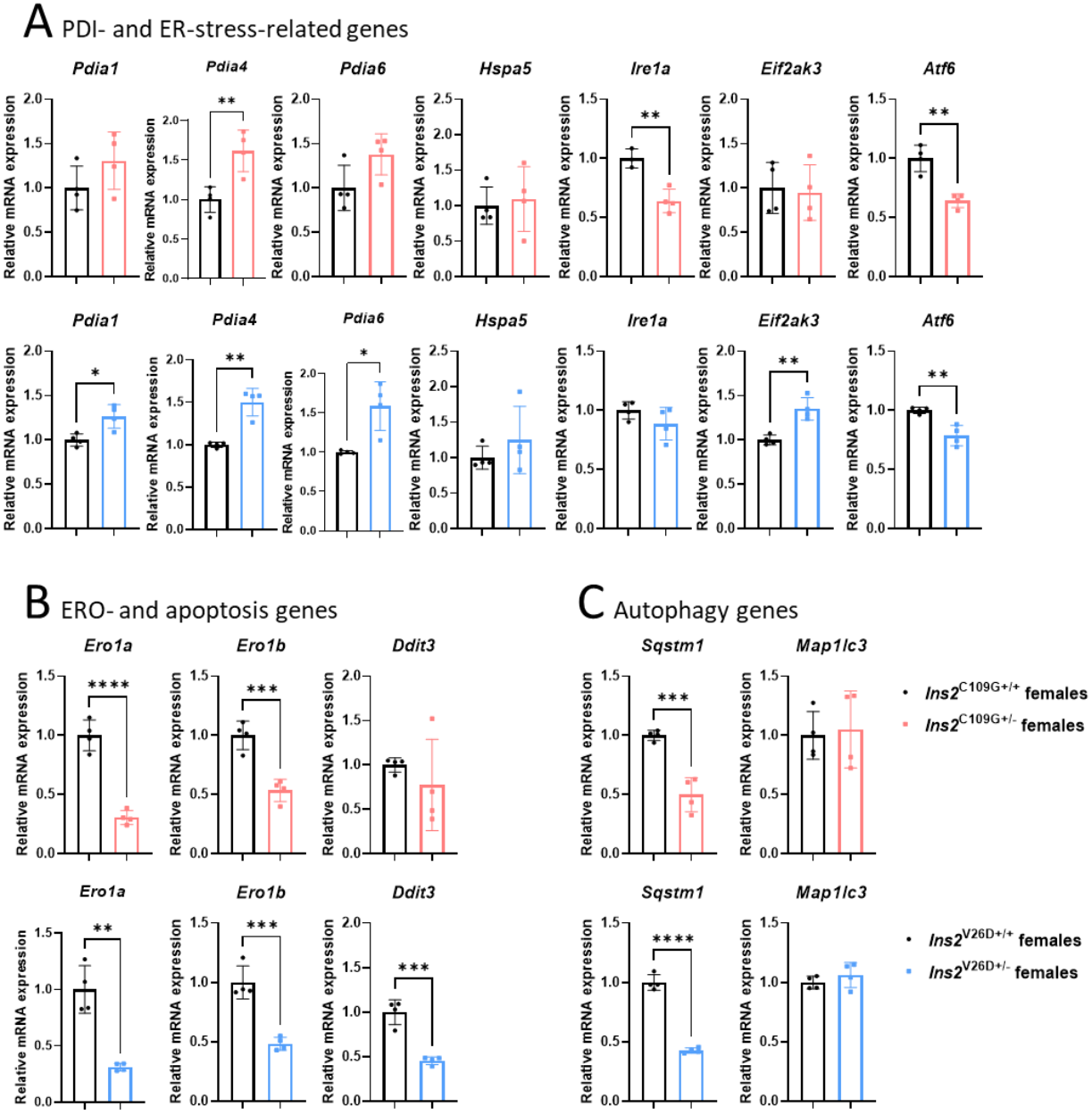

Supplementary Figure 9 Gene expression analysis from 8-week-old females

Relative mRNA expression of genes associated with **(A)** Protein disulfide isomerases and ER-stress, **(B)** ER-oxidoreductins and apoptosis, and **(C)** autophagy in WT and Ins2$^{C109G+/-}$ or Ins2$^{V26D+/-}$ females aged 8 weeks**;** n=3-4.

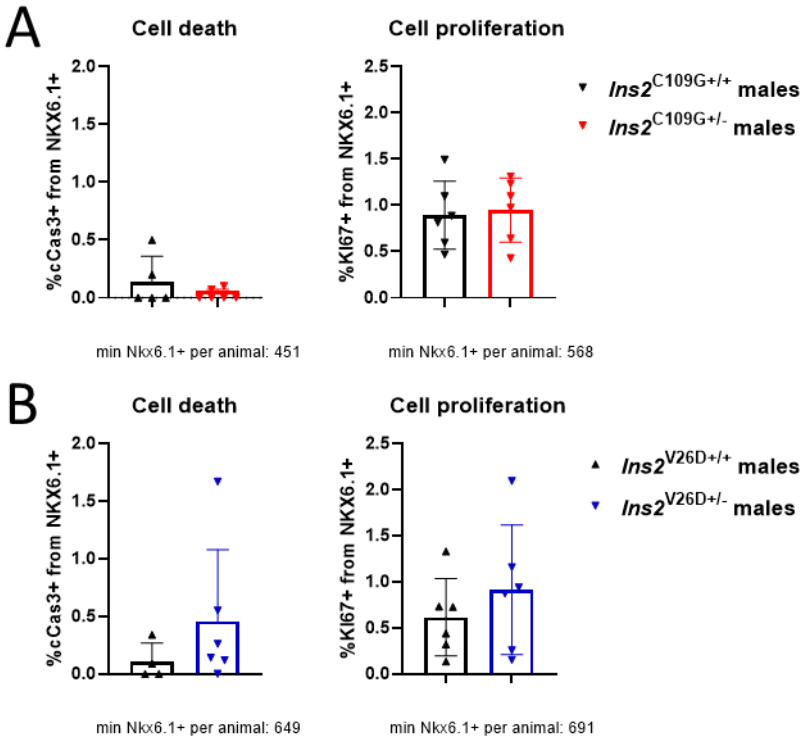

Supplementary Figure 10 Cell death and cell proliferation in 8-week-old animals

(A-B) Per cent (%) of NKX6.1+ cells that also express cleaved Caspase-3 (cCas3) or KI67 in 8-week-old Ins2^{C109G} **(A)** and Ins2^{V26D} **(B)** and WT males; n=4-6.

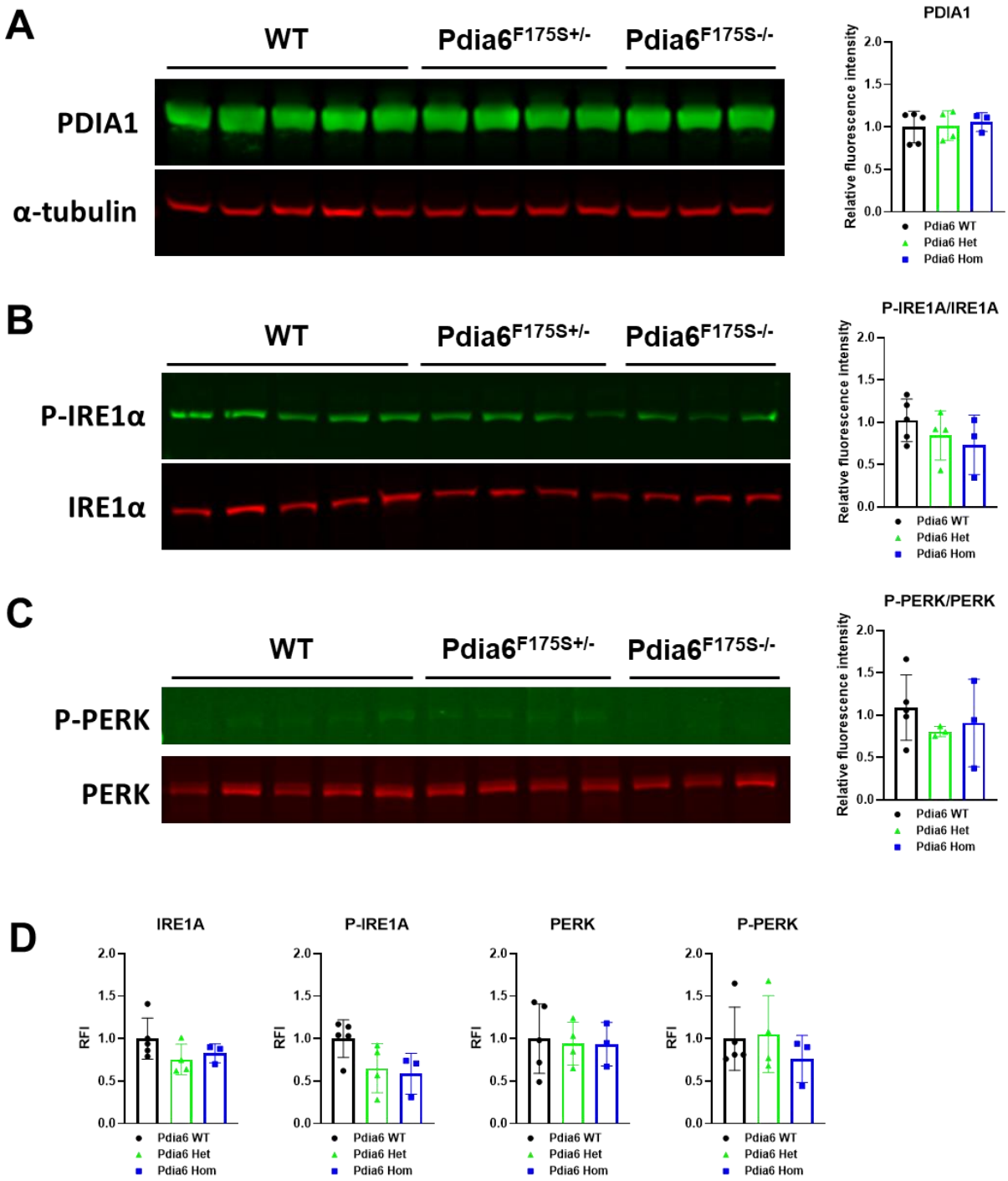

Supplementary Figure 11 Additional western blot results for PDIA6

(A-D) Western blot analyses and quantification of **(A)** PDIA1, **(B)** P-IRE1A/IRE1A, **(C)** P-PERK/PERK, and **(D)** Individual quantifications for IRE1A, P-IRE1A, PERK and P-PERK in pancreatic tissue; n=3-5. Mice aged P21 were used for all experiments. Parts of the figure are adapted from Chhabra and Amend et al. 2021.

Sperm ID	Position cDNA	Nucleotide exchange	Exon/intron	Protein exchange	Mutation type
21041347	c.181	G>A	Ex 2	Ala61Thr (A61T)	missense
21103501	c.371	G>C	Ex 3	Gly124Ala (G124A)	missense
21096929	c.456	C>T	Ex 4	Ile152Ile (I152I)	silent
10184617	c.757	C>A	Ex 7	Arg253Arg (R253R)	silent
21051881	2,163566116 (pos. chr. 2)	T>A	In 7-8	./.	./.
21094261	c.909	T>C	Ex 8	Ser303Ser (S303S)	silent
21095915	c.932	T>G	Ex 8	Leu311Arg (L311R)	missense
21047761	c.974	A>G	Ex 8	Asp325Gly (D325G)	missense
21098457	c.998	G>T	Ex 8	Arg333Leu (R333L)	missense
21046419	c.1002	T>A	Ex8	Phe334Leu (F334L)	missense

Supplementary Figure 13 Hnf4a-mutations found in the F1 archive

The two mouse models analyzed in this thesis are highlighted in grey.

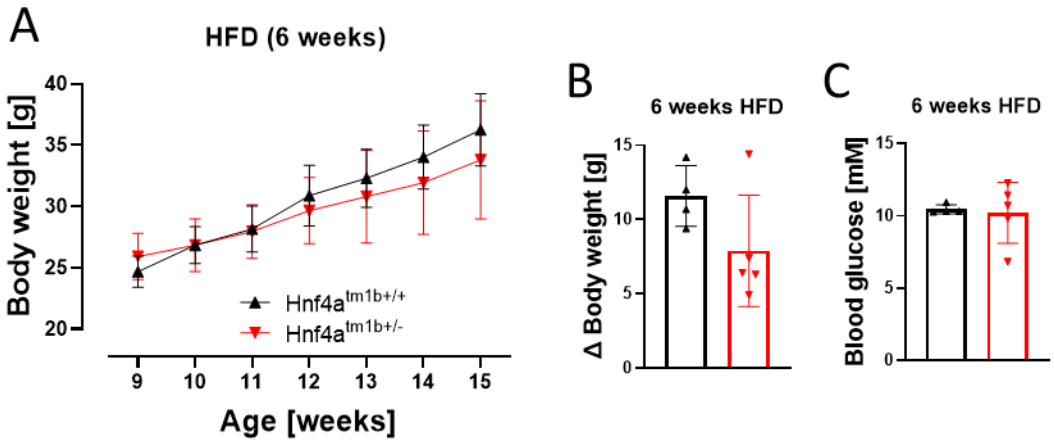

Supplementary Figure 12 HFD feeding in Hnf4a-KO

Hnf4a-KO animals were fed a HFD for 6 weeks from the age of 9 weeks to 15 weeks. **(A)** Body weight evolution in [g]. **(B)** Δ Body weight in [g] before sacrifice. **(C)** Blood glucose at the age of 15 weeks after 6 weeks of HFD; n=4-6.

Appendix B

Additional data that was not mentioned in the text.

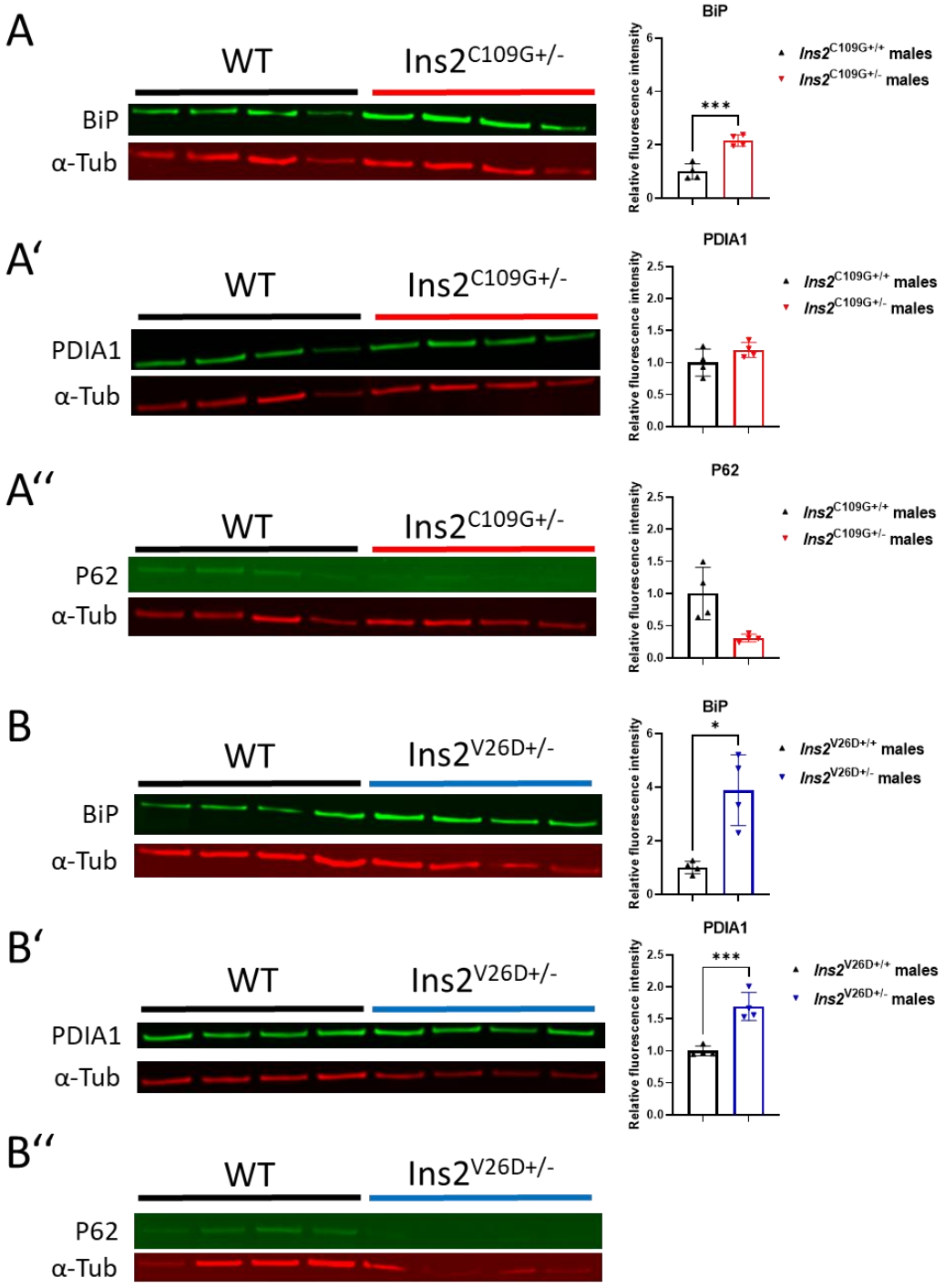

Appendix B 1 Protein expression in islets of 1-month old male Ins2-mutants

(A-B’’) Western blot analyses and quantification of **(A, B)** BiP, **(A’, B’)** PDIA1 and **(A’’-B’’)** P62 in 1-month-old Ins2^{C109G} **(A-A’’)** and Ins2^{V26D} **(B-B’’)** and WT males; n=4.

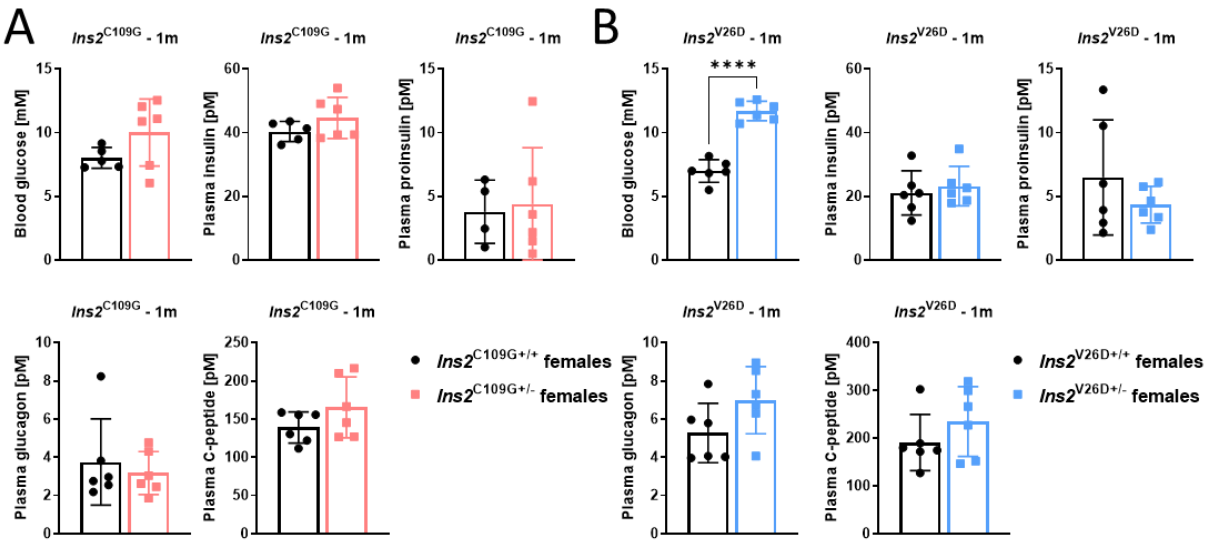

Appendix B 2 Plasma hormones in 8-week-old female Ins2 mutants

(A-B) Blood glucose [mM], plasma insulin [pM], plasma proinsulin [pM], plasma glucagon [pM] and plasma C-peptide [pM] from 8-week-old 6 h fasted WT, $Ins2^{C109G}$ **(A)** and $Ins2^{V26D}$ **(B)** female animals; n=4-6.

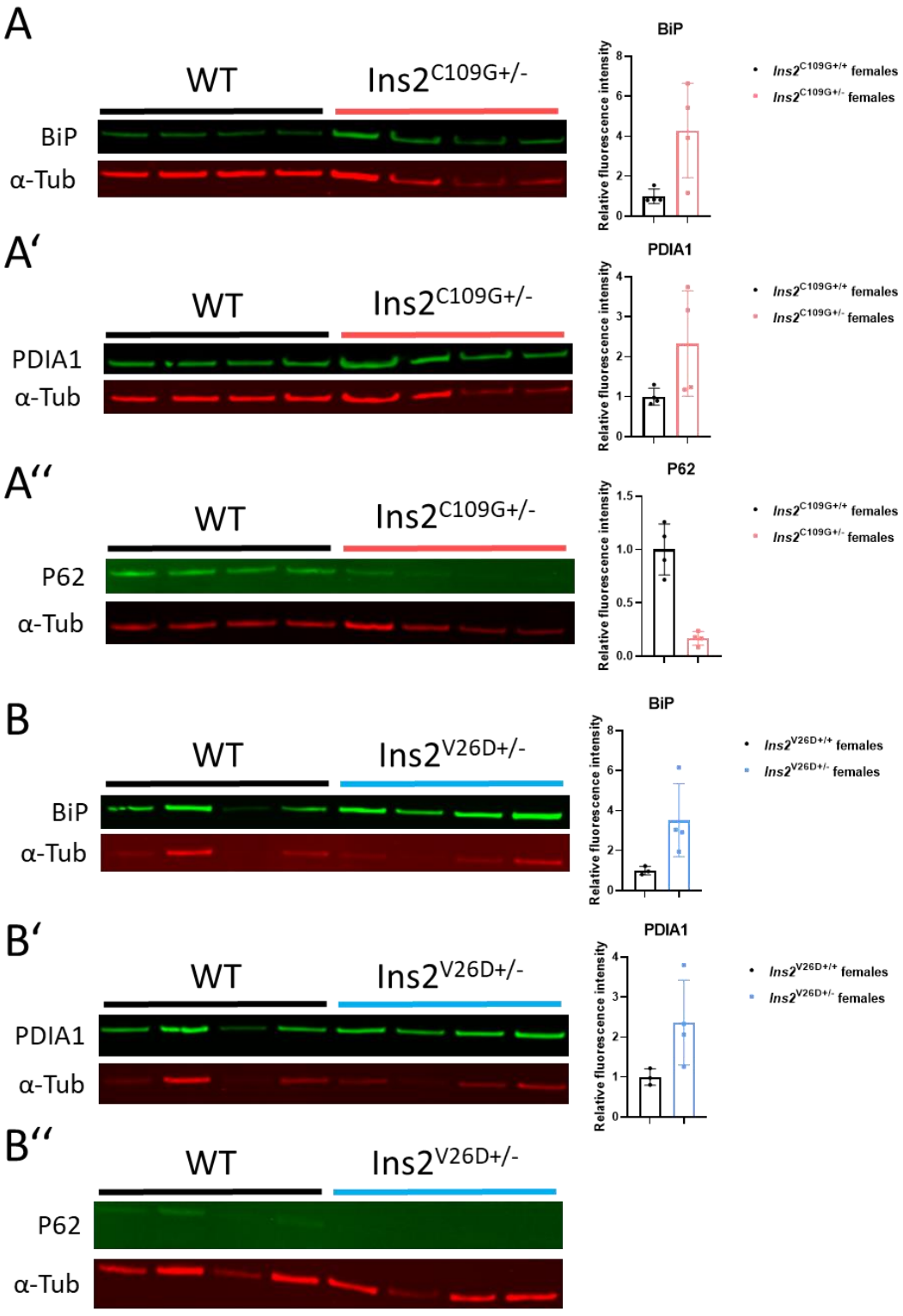

Appendix B 3 Protein expression in islets of 8-week-old female Ins2 mutants

(A-B'') Western blot analyses and quantification of **(A, B)** BiP, **(A', B')** PDIA1 and **(A''-B'')** P62 in 8-week-old Ins2^{C109G} **(A-A'')** and Ins2^{V26D} **(B-B'')** and WT females; n=4.

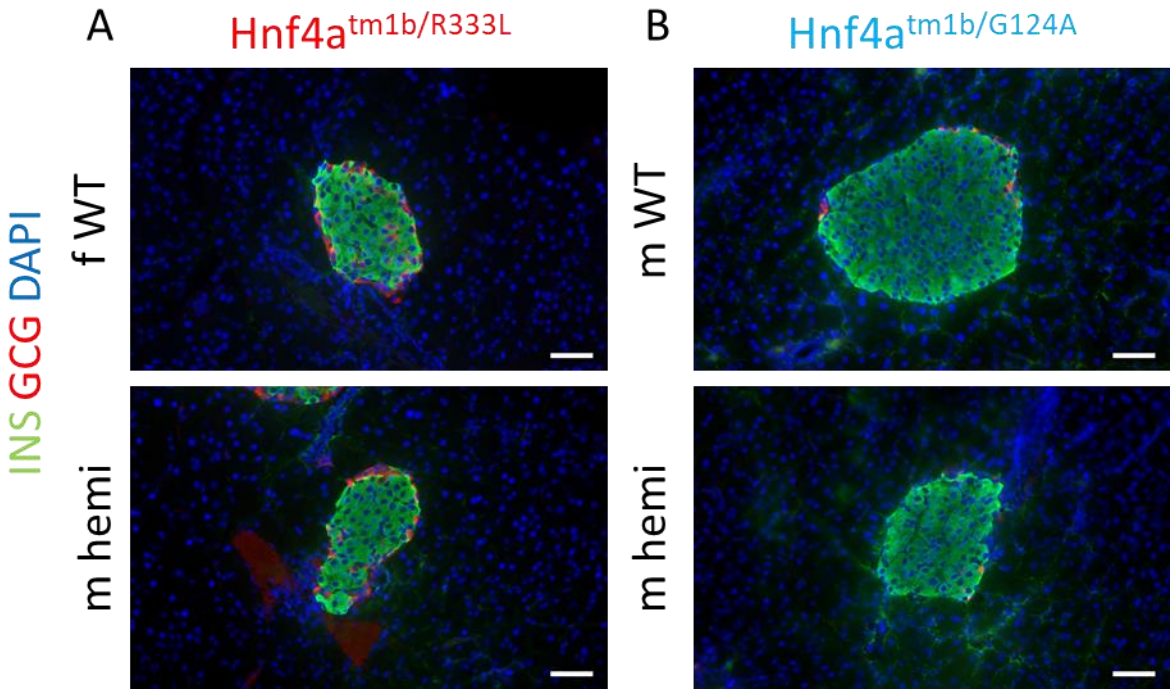

Appendix B 4 INS and GCG in Hnfa$^{tm1b/R333L}$ and Hnf4a$^{tm1b/G124A}$

(A-B) Representative images of islets of Langerhans' of Hnf4a$^{tm1b/R333L}$ **(A)**, Hnf4a$^{tm1b/G124A}$ **(B)** and WT animals. DAPI: blue, insulin: green, glucagon: red; Scale bars equal 20 µm; age 8 weeks.

Literature

1. Pan, F.C. and C. Wright, *Pancreas organogenesis: from bud to plexus to gland.* Dev Dyn, 2011. **240**(3): p. 530-65.
2. Slack, J.M., *Developmental biology of the pancreas.* Development, 1995. **121**(6): p. 1569-80.
3. Bastidas-Ponce, A., et al., *Cellular and molecular mechanisms coordinating pancreas development.* Development, 2017. **144**(16): p. 2873-2888.
4. Rojas, A., et al., *Islet cell development.* Adv Exp Med Biol, 2010. **654**: p. 59-75.
5. Langerhans, P., 1847-1888, *Beiträge zur mikroskopischen Anatomie der Bauchspeicheldrüse : Inaugural-Dissertaton, zur Erlangung der Doctorwürde in der Medicin und Chirurgie vorgelegt der Medicinischen Facultät der Friedrich-Wilhelms-Universität zu Berlin und öffentlich zu vertheidigen am 18. Februar 1869*. 1869: Berlin : Buchdruckerei von Gustav Lange, 1869.
6. Minkowski, O., 1858-1931, *Untersuchungen über den Diabetes mellitus nach Exstirpation des Pankreas*. 1893, Leipzig: F.C.W. Vogel.
7. Flier, J.S. and C.R. Kahn, *Insulin: A pacesetter for the shape of modern biomedical science and the Nobel Prize.* Mol Metab, 2021. **52**: p. 101194.
8. McEvoy, R.C., *Changes in the volumes of the A-, B-, and D-cell populations in the pancreatic islets during the postnatal development of the rat.* Diabetes, 1981. **30**(10): p. 813-7.
9. Steiner, D.J., et al., *Pancreatic islet plasticity: interspecies comparison of islet architecture and composition.* Islets, 2010. **2**(3): p. 135-45.
10. Orci, L. and R.H. Unger, *Functional subdivision of islets of Langerhans and possible role of D cells.* Lancet, 1975. **2**(7947): p. 1243-4.
11. Bosco, D., et al., *Unique arrangement of alpha- and beta-cells in human islets of Langerhans.* Diabetes, 2010. **59**(5): p. 1202-10.
12. Moin, A.S.M. and A.E. Butler, *Alterations in Beta Cell Identity in Type 1 and Type 2 Diabetes.* Curr Diab Rep, 2019. **19**(9): p. 83.
13. Rutter, G.A., et al., *Pancreatic beta-cell identity, glucose sensing and the control of insulin secretion.* Biochem J, 2015. **466**(2): p. 203-18.
14. Jo, J., M.Y. Choi, and D.S. Koh, *Size distribution of mouse Langerhans islets.* Biophys J, 2007. **93**(8): p. 2655-66.
15. Brereton, M.F., et al., *Hyperglycaemia induces metabolic dysfunction and glycogen accumulation in pancreatic beta-cells.* Nat Commun, 2016. **7**: p. 13496.
16. Matschinsky, F.M., *Glucokinase as glucose sensor and metabolic signal generator in pancreatic beta-cells and hepatocytes.* Diabetes, 1990. **39**(6): p. 647-52.
17. Herzig, S., et al., *Identification and functional expression of the mitochondrial pyruvate carrier.* Science, 2012. **337**(6090): p. 93-6.
18. Ashcroft, F.M., D.E. Harrison, and S.J. Ashcroft, *Glucose induces closure of single potassium channels in isolated rat pancreatic beta-cells.* Nature, 1984. **312**(5993): p. 446-8.
19. Cook, D.L. and C.N. Hales, *Intracellular ATP directly blocks K+ channels in pancreatic B-cells.* Nature, 1984. **311**(5983): p. 271-3.
20. Petersen, M.C. and G.I. Shulman, *Mechanisms of Insulin Action and Insulin Resistance.* Physiol Rev, 2018. **98**(4): p. 2133-2223.
21. Nauck, M.A. and J.J. Meier, *Incretin hormones: Their role in health and disease.* Diabetes Obes Metab, 2018. **20 Suppl 1**: p. 5-21.
22. Marchetti, P., et al., *Pancreatic Beta Cell Identity in Humans and the Role of Type 2 Diabetes.* Front Cell Dev Biol, 2017. **5**: p. 55.
23. Salinno, C., et al., *beta-Cell Maturation and Identity in Health and Disease.* Int J Mol Sci, 2019. **20**(21).

24. Dassaye, R., S. Naidoo, and M.E. Cerf, *Transcription factor regulation of pancreatic organogenesis, differentiation and maturation.* Islets, 2016. **8**(1): p. 13-34.
25. Aigha, II and E.M. Abdelalim, *NKX6.1 transcription factor: a crucial regulator of pancreatic beta cell development, identity, and proliferation.* Stem Cell Res Ther, 2020. **11**(1): p. 459.
26. Huang, J.L., et al., *Genetic deletion of Urocortin 3 does not prevent functional maturation of beta cells.* J Endocrinol, 2020. **246**(1): p. 69-78.
27. Hang, Y. and R. Stein, *MafA and MafB activity in pancreatic beta cells.* Trends Endocrinol Metab, 2011. **22**(9): p. 364-73.
28. Tritschler, S., et al., *Systematic single-cell analysis provides new insights into heterogeneity and plasticity of the pancreas.* Mol Metab, 2017. **6**(9): p. 974-990.
29. Melloul, D., S. Marshak, and E. Cerasi, *Regulation of insulin gene transcription.* Diabetologia, 2002. **45**(3): p. 309-26.
30. Brereton, M.F., et al., *Reversible changes in pancreatic islet structure and function produced by elevated blood glucose.* Nat Commun, 2014. **5**: p. 4639.
31. Weir, G.C. and S. Bonner-Weir, *Five stages of evolving beta-cell dysfunction during progression to diabetes.* Diabetes, 2004. **53 Suppl 3**: p. S16-21.
32. Stekelenburg, C.M. and V.M. Schwitzgebel, *Genetic Defects of the beta-Cell That Cause Diabetes.* Endocr Dev, 2016. **31**: p. 179-202.
33. Cnop, M., et al., *Endoplasmic reticulum stress and eIF2alpha phosphorylation: The Achilles heel of pancreatic beta cells.* Mol Metab, 2017. **6**(9): p. 1024-1039.
34. Eizirik, D.L., A.K. Cardozo, and M. Cnop, *The role for endoplasmic reticulum stress in diabetes mellitus.* Endocr Rev, 2008. **29**(1): p. 42-61.
35. Hummasti, S. and G.S. Hotamisligil, *Endoplasmic reticulum stress and inflammation in obesity and diabetes.* Circ Res, 2010. **107**(5): p. 579-91.
36. Liu, M., et al., *Biosynthesis, structure, and folding of the insulin precursor protein.* Diabetes Obes Metab, 2018. **20 Suppl 2**: p. 28-50.
37. Riahi, Y., et al., *Effects of proinsulin misfolding on beta-cell dynamics, differentiation and function in diabetes.* Diabetes Obes Metab, 2018. **20 Suppl 2**: p. 95-103.
38. Sun, J., et al., *Proinsulin misfolding and endoplasmic reticulum stress during the development and progression of diabetes.* Mol Aspects Med, 2015. **42**: p. 105-18.
39. Liu, M., et al., *Mutant INS-gene induced diabetes of youth: proinsulin cysteine residues impose dominant-negative inhibition on wild-type proinsulin transport.* PLoS One, 2010. **5**(10): p. e13333.
40. Liu, M., et al., *Proinsulin maturation, misfolding, and proteotoxicity.* Proc Natl Acad Sci U S A, 2007. **104**(40): p. 15841-6.
41. Liu, M., et al., *Deciphering the hidden informational content of protein sequences: foldability of proinsulin hinges on a flexible arm that is dispensable in the mature hormone.* J Biol Chem, 2010. **285**(40): p. 30989-1001.
42. Liu, M., et al., *Impaired cleavage of preproinsulin signal peptide linked to autosomal-dominant diabetes.* Diabetes, 2012. **61**(4): p. 828-37.
43. Liu, M., et al., *INS-gene mutations: from genetics and beta cell biology to clinical disease.* Mol Aspects Med, 2015. **42**: p. 3-18.
44. Liu, M., et al., *Proinsulin entry and transit through the endoplasmic reticulum in pancreatic beta cells.* Vitam Horm, 2014. **95**: p. 35-62.
45. Hwang, J. and L. Qi, *Quality Control in the Endoplasmic Reticulum: Crosstalk between ERAD and UPR pathways.* Trends Biochem Sci, 2018. **43**(8): p. 593-605.
46. Papa, F.R., *Endoplasmic reticulum stress, pancreatic beta-cell degeneration, and diabetes.* Cold Spring Harb Perspect Med, 2012. **2**(9): p. a007666.

47. Gupta, S., B. McGrath, and D.R. Cavener, *PERK (EIF2AK3) regulates proinsulin trafficking and quality control in the secretory pathway.* Diabetes, 2010. **59**(8): p. 1937-47.
48. Zhang, W., et al., *PERK EIF2AK3 control of pancreatic beta cell differentiation and proliferation is required for postnatal glucose homeostasis.* Cell Metab, 2006. **4**(6): p. 491-7.
49. Back, S.H., et al., *Translation attenuation through eIF2alpha phosphorylation prevents oxidative stress and maintains the differentiated state in beta cells.* Cell Metab, 2009. **10**(1): p. 13-26.
50. Han, J., et al., *Antioxidants Complement the Requirement for Protein Chaperone Function to Maintain beta-Cell Function and Glucose Homeostasis.* Diabetes, 2015. **64**(8): p. 2892-904.
51. Julier, C. and M. Nicolino, *Wolcott-Rallison syndrome.* Orphanet J Rare Dis, 2010. **5**: p. 29.
52. Moore, K. and J. Hollien, *Ire1-mediated decay in mammalian cells relies on mRNA sequence, structure, and translational status.* Mol Biol Cell, 2015. **26**(16): p. 2873-84.
53. Hollien, J. and J.S. Weissman, *Decay of endoplasmic reticulum-localized mRNAs during the unfolded protein response.* Science, 2006. **313**(5783): p. 104-7.
54. Chen, Y. and F. Brandizzi, *IRE1: ER stress sensor and cell fate executor.* Trends Cell Biol, 2013. **23**(11): p. 547-55.
55. Hassler, J.R., et al., *The IRE1alpha/XBP1s Pathway Is Essential for the Glucose Response and Protection of beta Cells.* PLoS Biol, 2015. **13**(10): p. e1002277.
56. Lee, H., et al., *Beta Cell Dedifferentiation Induced by IRE1alpha Deletion Prevents Type 1 Diabetes.* Cell Metab, 2020. **31**(4): p. 822-836 e5.
57. Usui, M., et al., *Atf6alpha-null mice are glucose intolerant due to pancreatic beta-cell failure on a high-fat diet but partially resistant to diet-induced insulin resistance.* Metabolism, 2012. **61**(8): p. 1118-28.
58. Eletto, D., et al., *Redox controls UPR to control redox.* J Cell Sci, 2014. **127**(Pt 17): p. 3649-58.
59. Awazawa, M., et al., *Deregulation of pancreas-specific oxidoreductin ERO1beta in the pathogenesis of diabetes mellitus.* Mol Cell Biol, 2014. **34**(7): p. 1290-9.
60. Eletto, D., et al., *PDIA6 regulates insulin secretion by selectively inhibiting the RIDD activity of IRE1.* FASEB J, 2016. **30**(2): p. 653-65.
61. Jang, I., et al., *PDIA1/P4HB is required for efficient proinsulin maturation and ss cell health in response to diet induced obesity.* Elife, 2019. **8**.
62. Zito, E., et al., *ERO1-beta, a pancreas-specific disulfide oxidase, promotes insulin biogenesis and glucose homeostasis.* J Cell Biol, 2010. **188**(6): p. 821-32.
63. Ellgaard, L. and L.W. Ruddock, *The human protein disulphide isomerase family: substrate interactions and functional properties.* EMBO Rep, 2005. **6**(1): p. 28-32.
64. Hatahet, F. and L.W. Ruddock, *Protein disulfide isomerase: a critical evaluation of its function in disulfide bond formation.* Antioxid Redox Signal, 2009. **11**(11): p. 2807-50.
65. Bugliani, M., et al., *Modulation of Autophagy Influences the Function and Survival of Human Pancreatic Beta Cells Under Endoplasmic Reticulum Stress Conditions and in Type 2 Diabetes.* Front Endocrinol (Lausanne), 2019. **10**: p. 52.
66. Riahi, Y., et al., *Autophagy is a major regulator of beta cell insulin homeostasis.* Diabetologia, 2016. **59**(7): p. 1480-1491.
67. Jung, H.S., et al., *Loss of autophagy diminishes pancreatic beta cell mass and function with resultant hyperglycemia.* Cell Metab, 2008. **8**(4): p. 318-24.
68. Dikic, I. and Z. Elazar, *Mechanism and medical implications of mammalian autophagy.* Nat Rev Mol Cell Biol, 2018. **19**(6): p. 349-364.
69. Sanchez-Martin, P. and M. Komatsu, *p62/SQSTM1 - steering the cell through health and disease.* J Cell Sci, 2018. **131**(21).
70. Rui, J., et al., *beta Cells that Resist Immunological Attack Develop during Progression of Autoimmune Diabetes in NOD Mice.* Cell Metab, 2017. **25**(3): p. 727-738.

71. Talchai, C., et al., *Pancreatic beta cell dedifferentiation as a mechanism of diabetic beta cell failure.* Cell, 2012. **150**(6): p. 1223-34.
72. Nimkulrat, S.D., et al., *The Anna Karenina Model of beta-Cell Maturation in Development and Their Dedifferentiation in Type 1 and Type 2 Diabetes.* Diabetes, 2021. **70**(9): p. 2058-2066.
73. Thorel, F., et al., *Conversion of adult pancreatic alpha-cells to beta-cells after extreme beta-cell loss.* Nature, 2010. **464**(7292): p. 1149-54.
74. Lam, C.J., et al., *Low-Level Insulin Content Within Abundant Non-beta Islet Endocrine Cells in Long-standing Type 1 Diabetes.* Diabetes, 2019. **68**(3): p. 598-608.
75. Gao, T., et al., *Pdx1 maintains beta cell identity and function by repressing an alpha cell program.* Cell Metab, 2014. **19**(2): p. 259-71.
76. Thompson, P.J., et al., *Targeted Elimination of Senescent Beta Cells Prevents Type 1 Diabetes.* Cell Metab, 2019. **29**(5): p. 1045-1060 e10.
77. Sun, H., et al., *IDF diabetes Atlas: Global, regional and country-level diabetes prevalence estimates for 2021 and projections for 2045.* Diabetes Res Clin Pract, 2021: p. 109119.
78. American Diabetes, A., *2. Classification and Diagnosis of Diabetes: Standards of Medical Care in Diabetes-2021.* Diabetes Care, 2021. **44**(Suppl 1): p. S15-S33.
79. Eizirik, D.L., L. Pasquali, and M. Cnop, *Pancreatic beta-cells in type 1 and type 2 diabetes mellitus: different pathways to failure.* Nat Rev Endocrinol, 2020. **16**(7): p. 349-362.
80. Saeedi, P., et al., *Global and regional diabetes prevalence estimates for 2019 and projections for 2030 and 2045: Results from the International Diabetes Federation Diabetes Atlas, 9(th) edition.* Diabetes Res Clin Pract, 2019. **157**: p. 107843.
81. Flannick, J., S. Johansson, and P.R. Njolstad, *Common and rare forms of diabetes mellitus: towards a continuum of diabetes subtypes.* Nat Rev Endocrinol, 2016. **12**(7): p. 394-406.
82. Muoio, D.M. and C.B. Newgard, *Mechanisms of disease:Molecular and metabolic mechanisms of insulin resistance and beta-cell failure in type 2 diabetes.* Nat Rev Mol Cell Biol, 2008. **9**(3): p. 193-205.
83. Wagner, R., et al., *Pathophysiology-based subphenotyping of individuals at elevated risk for type 2 diabetes.* Nat Med, 2021. **27**(1): p. 49-57.
84. Peixoto-Barbosa, R., A.F. Reis, and F.M.A. Giuffrida, *Update on clinical screening of maturity-onset diabetes of the young (MODY).* Diabetol Metab Syndr, 2020. **12**: p. 50.
85. Beltrand, J., et al., *Neonatal Diabetes Mellitus.* Front Pediatr, 2020. **8**: p. 540718.
86. Stoy, J., et al., *In celebration of a century with insulin - Update of insulin gene mutations in diabetes.* Mol Metab, 2021: p. 101280.
87. Al-Fadhli, F.M., et al., *Biallelic loss of function variant in the unfolded protein response gene PDIA6 is associated with asphyxiating thoracic dystrophy and neonatal-onset diabetes.* Clin Genet, 2021. **99**(5): p. 694-703.
88. Leroux, L., et al., *Compensatory responses in mice carrying a null mutation for Ins1 or Ins2.* Diabetes, 2001. **50 Suppl 1**: p. S150-3.
89. Izumi, T., et al., *Dominant negative pathogenesis by mutant proinsulin in the Akita diabetic mouse.* Diabetes, 2003. **52**(2): p. 409-16.
90. Herbach, N., et al., *Dominant-negative effects of a novel mutated Ins2 allele causes early-onset diabetes and severe beta-cell loss in Munich Ins2C95S mutant mice.* Diabetes, 2007. **56**(5): p. 1268-76.
91. Austin, A.L.F., et al., *The KINGS Ins2 (+/G32S) Mouse: A Novel Model of Beta Cell Endoplasmic Reticulum Stress and Human Diabetes.* Diabetes, 2020.
92. Sakano, D., et al., *Insulin2(Q104del) (Kuma) mutant mice develop diabetes with dominant inheritance.* Sci Rep, 2020. **10**(1): p. 12187.

93. Nozaki, J., et al., *The endoplasmic reticulum stress response is stimulated through the continuous activation of transcription factors ATF6 and XBP1 in Ins2+/Akita pancreatic beta cells.* Genes Cells, 2004. **9**(3): p. 261-70.
94. Riahi, Y., et al., *Inhibition of mTORC1 by ER stress impairs neonatal beta-cell expansion and predisposes to diabetes in the Akita mouse.* Elife, 2018. **7**.
95. Xu, B., et al., *Estrogens Promote Misfolded Proinsulin Degradation to Protect Insulin Production and Delay Diabetes.* Cell Rep, 2018. **24**(1): p. 181-196.
96. Su, A.I., et al., *Large-scale analysis of the human and mouse transcriptomes.* Proc Natl Acad Sci U S A, 2002. **99**(7): p. 4465-70.
97. Choi, J.H., et al., *Essential cell-extrinsic requirement for PDIA6 in lymphoid and myeloid development.* J Exp Med, 2020. **217**(4).
98. Eletto, D., et al., *Protein disulfide isomerase A6 controls the decay of IRE1alpha signaling via disulfide-dependent association.* Mol Cell, 2014. **53**(4): p. 562-576.
99. Crevecoeur, I., et al., *Early differences in islets from prediabetic NOD mice: combined microarray and proteomic analysis.* Diabetologia, 2017. **60**(3): p. 475-489.
100. Chhabra, N.F., et al., *A point mutation in the Pdia6 gene results in loss of pancreatic beta-cell identity causing overt diabetes.* Mol Metab, 2021: p. 101334.
101. Colclough, K., et al., *Mutations in the genes encoding the transcription factors hepatocyte nuclear factor 1 alpha and 4 alpha in maturity-onset diabetes of the young and hyperinsulinemic hypoglycemia.* Hum Mutat, 2013. **34**(5): p. 669-85.
102. Colclough, K., et al., *Clinical utility gene card for: Maturity-onset diabetes of the young.* Eur J Hum Genet, 2014. **22**(9).
103. Wang, H., et al., *Hepatocyte nuclear factor 4alpha regulates the expression of pancreatic beta -cell genes implicated in glucose metabolism and nutrient-induced insulin secretion.* J Biol Chem, 2000. **275**(46): p. 35953-9.
104. Ihara, A., et al., *Functional characterization of the HNF4alpha isoform (HNF4alpha8) expressed in pancreatic beta-cells.* Biochem Biophys Res Commun, 2005. **329**(3): p. 984-90.
105. Kanazawa, T., et al., *Expression of hepatocyte nuclear factor 4alpha in developing mice.* Anat Histol Embryol, 2009. **38**(1): p. 34-41.
106. Torres-Padilla, M.E. and M.C. Weiss, *Effects of interactions of hepatocyte nuclear factor 4alpha isoforms with coactivators and corepressors are promoter-specific.* FEBS Lett, 2003. **539**(1-3): p. 19-23.
107. Boj, S.F., et al., *A transcription factor regulatory circuit in differentiated pancreatic cells.* Proc Natl Acad Sci U S A, 2001. **98**(25): p. 14481-6.
108. Boj, S.F., D. Petrov, and J. Ferrer, *Epistasis of transcriptomes reveals synergism between transcriptional activators Hnf1alpha and Hnf4alpha.* PLoS Genet, 2010. **6**(5): p. e1000970.
109. Yamagata, K., *Roles of HNF1alpha and HNF4alpha in pancreatic beta-cells: lessons from a monogenic form of diabetes (MODY).* Vitam Horm, 2014. **95**: p. 407-23.
110. Gupta, R.K., et al., *The MODY1 gene HNF-4alpha regulates selected genes involved in insulin secretion.* J Clin Invest, 2005. **115**(4): p. 1006-15.
111. Dubois, V., et al., *Control of Cell Identity by the Nuclear Receptor HNF4 in Organ Pathophysiology.* Cells, 2020. **9**(10).
112. Miura, A., et al., *Hepatocyte nuclear factor-4alpha is essential for glucose-stimulated insulin secretion by pancreatic beta-cells.* J Biol Chem, 2006. **281**(8): p. 5246-57.
113. Chen, W.S., et al., *Disruption of the HNF-4 gene, expressed in visceral endoderm, leads to cell death in embryonic ectoderm and impaired gastrulation of mouse embryos.* Genes Dev, 1994. **8**(20): p. 2466-77.

114. Stoffel, M. and S.A. Duncan, *The maturity-onset diabetes of the young (MODY1) transcription factor HNF4alpha regulates expression of genes required for glucose transport and metabolism.* Proc Natl Acad Sci U S A, 1997. **94**(24): p. 13209-14.
115. Harries, L.W., J.E. Brown, and A.L. Gloyn, *Species-specific differences in the expression of the HNF1A, HNF1B and HNF4A genes.* PLoS One, 2009. **4**(11): p. e7855.
116. Muller, T.D., et al., *Glucagon-like peptide 1 (GLP-1).* Mol Metab, 2019. **30**: p. 72-130.
117. Rosenberg, S.A., et al., *Gene transfer into humans--immunotherapy of patients with advanced melanoma, using tumor-infiltrating lymphocytes modified by retroviral gene transduction.* N Engl J Med, 1990. **323**(9): p. 570-8.
118. Phillips, M.I., *Gene, stem cell, and future therapies for orphan diseases.* Clin Pharmacol Ther, 2012. **92**(2): p. 182-92.
119. Keeler, A.M., M.K. ElMallah, and T.R. Flotte, *Gene Therapy 2017: Progress and Future Directions.* Clin Transl Sci, 2017. **10**(4): p. 242-248.
120. Ginn, S.L., et al., *Gene therapy clinical trials worldwide to 2017: An update.* J Gene Med, 2018. **20**(5): p. e3015.
121. Naso, M.F., et al., *Adeno-Associated Virus (AAV) as a Vector for Gene Therapy.* BioDrugs, 2017. **31**(4): p. 317-334.
122. Aponte-Ubillus, J.J., et al., *Molecular design for recombinant adeno-associated virus (rAAV) vector production.* Appl Microbiol Biotechnol, 2018. **102**(3): p. 1045-1054.
123. Mingozzi, F. and K.A. High, *Therapeutic in vivo gene transfer for genetic disease using AAV: progress and challenges.* Nat Rev Genet, 2011. **12**(5): p. 341-55.
124. Jaen, M.L., et al., *Long-Term Efficacy and Safety of Insulin and Glucokinase Gene Therapy for Diabetes: 8-Year Follow-Up in Dogs.* Mol Ther Methods Clin Dev, 2017. **6**: p. 1-7.
125. Jimenez, V., et al., *FGF21 gene therapy as treatment for obesity and insulin resistance.* EMBO Mol Med, 2018. **10**(8).
126. Mallol, C., et al., *AAV-mediated pancreatic overexpression of Igf1 counteracts progression to autoimmune diabetes in mice.* Mol Metab, 2017. **6**(7): p. 664-680.
127. Nathwani, A.C., et al., *Long-term safety and efficacy of factor IX gene therapy in hemophilia B.* N Engl J Med, 2014. **371**(21): p. 1994-2004.
128. Nathwani, A.C., et al., *Adenovirus-associated virus vector-mediated gene transfer in hemophilia B.* N Engl J Med, 2011. **365**(25): p. 2357-65.
129. Ong, T., et al., *Adeno-Associated Viral Gene Therapy for Inherited Retinal Disease.* Pharm Res, 2019. **36**(2): p. 34.
130. Colella, P., G. Ronzitti, and F. Mingozzi, *Emerging Issues in AAV-Mediated In Vivo Gene Therapy.* Mol Ther Methods Clin Dev, 2018. **8**: p. 87-104.
131. Falese, L., et al., *Strategy to detect pre-existing immunity to AAV gene therapy.* Gene Ther, 2017. **24**(12): p. 768-778.
132. Callejas, D., et al., *Treatment of diabetes and long-term survival after insulin and glucokinase gene therapy.* Diabetes, 2013. **62**(5): p. 1718-29.
133. Ayuso, E., et al., *In vivo gene transfer to pancreatic beta cells by systemic delivery of adenoviral vectors.* Hum Gene Ther, 2004. **15**(8): p. 805-12.
134. Loiler, S.A., et al., *Localized gene expression following administration of adeno-associated viral vectors via pancreatic ducts.* Mol Ther, 2005. **12**(3): p. 519-27.
135. Jimenez, V., et al., *In vivo genetic engineering of murine pancreatic beta cells mediated by single-stranded adeno-associated viral vectors of serotypes 6, 8 and 9.* Diabetologia, 2011. **54**(5): p. 1075-86.
136. Johnson, J.D., *A practical guide to genetic engineering of pancreatic beta-cells in vivo: getting a grip on RIP and MIP.* Islets, 2014. **6**(3): p. e944439.

137. Alders, M., et al., *Determination of KCNQ1OT1 and H19 methylation levels in BWS and SRS patients using methylation-sensitive high-resolution melting analysis.* Eur J Hum Genet, 2009. **17**(4): p. 467-73.
138. Chhabra, N.F., et al., *PAX6 mutation alters circadian rhythm and beta cell function in mice without affecting glucose tolerance.* Commun Biol, 2020. **3**(1): p. 628.
139. Pfaffl, M.W., et al., *Determination of stable housekeeping genes, differentially regulated target genes and sample integrity: BestKeeper--Excel-based tool using pair-wise correlations.* Biotechnol Lett, 2004. **26**(6): p. 509-15.
140. Livak, K.J. and T.D. Schmittgen, *Analysis of relative gene expression data using real-time quantitative PCR and the 2(-Delta Delta C(T)) Method.* Methods, 2001. **25**(4): p. 402-8.
141. Hrabe de Angelis, M.H., et al., *Genome-wide, large-scale production of mutant mice by ENU mutagenesis.* Nat Genet, 2000. **25**(4): p. 444-7.
142. Aigner, B., et al., *Diabetes models by screen for hyperglycemia in phenotype-driven ENU mouse mutagenesis projects.* Am J Physiol Endocrinol Metab, 2008. **294**(2): p. E232-40.
143. Leete, P., et al., *Studies of insulin and proinsulin in pancreas and serum support the existence of aetiopathological endotypes of type 1 diabetes associated with age at diagnosis.* Diabetologia, 2020. **63**(6): p. 1258-1267.
144. Leach, M.R., et al., *Localization of the lectin, ERp57 binding, and polypeptide binding sites of calnexin and calreticulin.* J Biol Chem, 2002. **277**(33): p. 29686-97.
145. Gorasia, D.G., et al., *A prominent role of PDIA6 in processing of misfolded proinsulin.* Biochim Biophys Acta, 2016. **1864**(6): p. 715-723.
146. Coleman, J.L., et al., *Rapid Knockout and Reporter Mouse Line Generation and Breeding Colony Establishment Using EUCOMM Conditional-Ready Embryonic Stem Cells: A Case Study.* Front Endocrinol (Lausanne), 2015. **6**: p. 105.
147. Augustin, M., et al., *Efficient and fast targeted production of murine models based on ENU mutagenesis.* Mamm Genome, 2005. **16**(6): p. 405-13.
148. Sabrautzki, S., et al., *Point mutation of Ffar1 abrogates fatty acid-dependent insulin secretion, but protects against HFD-induced glucose intolerance.* Mol Metab, 2017. **6**(10): p. 1304-1312.
149. Maestro, M.A., et al., *Distinct roles of HNF1beta, HNF1alpha, and HNF4alpha in regulating pancreas development, beta-cell function and growth.* Endocr Dev, 2007. **12**: p. 33-45.
150. Odom, D.T., et al., *Control of pancreas and liver gene expression by HNF transcription factors.* Science, 2004. **303**(5662): p. 1378-81.
151. Basu, R., et al., *Mechanisms of the age-associated deterioration in glucose tolerance: contribution of alterations in insulin secretion, action, and clearance.* Diabetes, 2003. **52**(7): p. 1738-48.
152. Kollmus, H., et al., *A comprehensive and comparative phenotypic analysis of the collaborative founder strains identifies new and known phenotypes.* Mamm Genome, 2020. **31**(1-2): p. 30-48.
153. Champy, M.F., et al., *Genetic background determines metabolic phenotypes in the mouse.* Mamm Genome, 2008. **19**(5): p. 318-31.
154. Fontaine, D.A. and D.B. Davis, *Attention to Background Strain Is Essential for Metabolic Research: C57BL/6 and the International Knockout Mouse Consortium.* Diabetes, 2016. **65**(1): p. 25-33.
155. Ehrhardt, N., et al., *Adiposity-Independent Effects of Aging on Insulin Sensitivity and Clearance in Mice and Humans.* Obesity (Silver Spring), 2019. **27**(3): p. 434-443.
156. Naito, M., et al., *Therapeutic impact of leptin on diabetes, diabetic complications, and longevity in insulin-deficient diabetic mice.* Diabetes, 2011. **60**(9): p. 2265-73.
157. Bjornstad, P., et al., *Insulin sensitivity and complications in type 1 diabetes: New insights.* World J Diabetes, 2015. **6**(1): p. 8-16.
158. Liu, S., et al., *Misfolded proinsulin impairs processing of precursor of insulin receptor and insulin signaling in beta cells.* FASEB J, 2019. **33**(10): p. 11338-11348.

159. Whittaker, L., et al., *High-affinity insulin binding: insulin interacts with two receptor ligand binding sites.* Biochemistry, 2008. **47**(48): p. 12900-9.
160. Hua, Q.X., et al., *The folding nucleus of the insulin superfamily: a flexible peptide model foreshadows the native state.* J Biol Chem, 2006. **281**(38): p. 28131-42.
161. Michalak, M., et al., *Calreticulin, a multi-process calcium-buffering chaperone of the endoplasmic reticulum.* Biochem J, 2009. **417**(3): p. 651-66.
162. Ikezaki, M., et al., *Calreticulin protects insulin against reductive stress in vitro and in MIN6 cells.* Biochimie, 2020. **171-172**: p. 1-11.
163. Gomez-Navarro, N. and E. Miller, *Protein sorting at the ER-Golgi interface.* J Cell Biol, 2016. **215**(6): p. 769-778.
164. Blum, B., et al., *Functional beta-cell maturation is marked by an increased glucose threshold and by expression of urocortin 3.* Nat Biotechnol, 2012. **30**(3): p. 261-4.
165. Arensdorf, A.M., D. Diedrichs, and D.T. Rutkowski, *Regulation of the transcriptome by ER stress: non-canonical mechanisms and physiological consequences.* Front Genet, 2013. **4**: p. 256.
166. Robertson, R.P., et al., *Beta-cell glucose toxicity, lipotoxicity, and chronic oxidative stress in type 2 diabetes.* Diabetes, 2004. **53 Suppl 1**: p. S119-24.
167. Wright, J., et al., *Endoplasmic reticulum oxidoreductin-1alpha (Ero1alpha) improves folding and secretion of mutant proinsulin and limits mutant proinsulin-induced endoplasmic reticulum stress.* J Biol Chem, 2013. **288**(43): p. 31010-8.
168. Gulow, K., D. Bienert, and I.G. Haas, *BiP is feed-back regulated by control of protein translation efficiency.* J Cell Sci, 2002. **115**(Pt 11): p. 2443-52.
169. Han, J., et al., *ER-stress-induced transcriptional regulation increases protein synthesis leading to cell death.* Nat Cell Biol, 2013. **15**(5): p. 481-90.
170. Brentnall, M., et al., *Caspase-9, caspase-3 and caspase-7 have distinct roles during intrinsic apoptosis.* BMC Cell Biol, 2013. **14**: p. 32.
171. Yoshii, S.R. and N. Mizushima, *Monitoring and Measuring Autophagy.* Int J Mol Sci, 2017. **18**(9).
172. Tramunt, B., et al., *Sex differences in metabolic regulation and diabetes susceptibility.* Diabetologia, 2020. **63**(3): p. 453-461.
173. Kooptiwut, S., et al., *Estrogen reduces endoplasmic reticulum stress to protect against glucotoxicity induced-pancreatic beta-cell death.* J Steroid Biochem Mol Biol, 2014. **139**: p. 25-32.
174. Sachs, S., et al., *Targeted pharmacological therapy restores beta-cell function for diabetes remission.* Nat Metab, 2020. **2**(2): p. 192-209.
175. Thymiakou, E., E. Xenikaki, and D. Kardassis, *Intestine-specific ablation of the Hepatocyte Nuclear Factor 4a (Hnf4a) gene in mice has minimal impact on serum lipids and ileum gene expression profile due to upregulation of its paralog Hnf4g.* Biochim Biophys Acta Mol Cell Biol Lipids, 2022. **1867**(3): p. 159108.
176. Hung, S.S., et al., *AAV-Mediated CRISPR/Cas Gene Editing of Retinal Cells In Vivo.* Invest Ophthalmol Vis Sci, 2016. **57**(7): p. 3470-6.
177. Li, F., et al., *Comparison of CRISPR/Cas Endonucleases for in vivo Retinal Gene Editing.* Front Cell Neurosci, 2020. **14**: p. 570917.
178. Gray, S.J., et al., *Global CNS gene delivery and evasion of anti-AAV-neutralizing antibodies by intrathecal AAV administration in non-human primates.* Gene Ther, 2013. **20**(4): p. 450-9.
179. Hattersley, A.T., et al., *ISPAD Clinical Practice Consensus Guidelines 2018: The diagnosis and management of monogenic diabetes in children and adolescents.* Pediatr Diabetes, 2018. **19 Suppl 27**: p. 47-63.